Massive MIMO Channel Models for 5G Wireless Communication Systems and Beyond

by

Carlos Fernando LÓPEZ MARTINEZ

HERIOT WATT UNIVERSITY

Submitted for the degree of Doctor of Philosophy
at
Heriot-Watt University
School of Engineering and Physical Sciences

September 2019

Abstract

The recently standardised 5th generation (5G) wireless communication technologies and their evolution towards the 6th generation (6G) will enable low-latency, high-density, and high-capacity communications across a wide variety of scenarios under tight constraints on energy consumption and limited availability of radio electromagnetic spectrum. Massive multiple-input multiple-output (MIMO) technologies will be key to achieve some of these goals and cover the ever-growing demand of data rates, reliability and seamless connectivity.

Nowadays, the design and evaluation of new wireless communication technologies heavily rely on computationally-efficient channel models that can accurately capture essential propagation phenomena and flexibly adapt to a wide variety of scenarios. Thus, this thesis aims at providing methods of analysis of massive MIMO channels and developing advanced massive MIMO channel models that will help assess the 5G wireless communication technologies and beyond.

First, key aspects of massive MIMO channels are investigated through a stochastic transformation method capable of modelling the space-time varying (STV) distribution of the delay and angle of arrival (AoA) of multi-path components (MPCs). The proposed method is followed by a channel modelling approach based on STV parameters of the AoA distribution that leads to closed-form expressions of key massive MIMO channel statistical properties. These methods are employed to analyse widely-used channel models and reveal some of their limitations. This investigation provides fundamental insights about non-stationary properties of massive MIMO channels and paves the way for developing subsequent efficient and accurate channel models.

Second, three-dimensional (3D) non-stationary wideband geometry-based stochastic models (GBSMs) for massive MIMO communication systems are proposed. These models incorporate a novel approach to capture near-field effects, namely, the parabolic wavefront, that presents a good accuracy-complexity trade-off when compared to other existing techniques. In addition to cluster of MPCs (re)appearance, a Log-normal cluster-level shadowing process complements the modelling of large-scale fading over the array. Statistical properties of the models are derived and validated through simulations and measurements extracted from the available literature.

Third, a highly-flexible and efficient 3D space-time non-stationary wideband massive MIMO channel model based on an ray-level evolution approach is proposed as

a candidate for the design and assessment of 5G and beyond 5G (B5G) massive MIMO wireless communication technologies. The model can capture near-field effects, (dis)appearance, and large-scale fading of both clusters and individual MPCs by employing a single approach. Its efficiency relies upon a more realistic wavefront selection criterion, namely, the effective Rayleigh distance, which accounts for the limited lifespan of MPCs over the array. This novel criterion can help improve the efficiency of both existing and B5G massive MIMO channel models by greatly reducing the need for spherical wavefronts.

to my family, specially Isa and Leo ...

Acknowledgments

This thesis would not have been possible without the support and advice of many people. First, I am grateful to my supervisor Prof. Cheng-Xiang Wang from whom I learned the difficulties of being rigorous, clear and concise at the same time. Thank you for your patience, advice and encouragement.

I am also thankful to my colleagues at the AWiTec Lab: Yu Fu, Gong Liang, Ahmed Al-Kinani, Qiuming Zhu, Qianru Zhou, Yiu Liu, Rui Feng, Shangbin Wu and many others with whom I shared office, interesting discussions and fun. The few Chinese words I remember do not reflect how much I learned from you over these years.

I am also happy to have met and worked with all ESR fellows in the 5Gwireless project: Yi Tan, Veda, Merve, Abdu, Shanshan, Thanh, Giovanni, Trinh, Amin, Panagiotis, Alex, Ahmed, Zahid and Nikos. Our meetings, schools, conferences, secondments, rehearsals for the mid-term review were intense, some times challenging, but also one of the greatest working and personal experiences I ever had.

I appreciate the warm welcome and support from Beatriz, Alberto, Carlos, Maialen and other colleagues from TTI Norte during my secondment in Santander. It is hard to believe the cutting-edge technology a small Spanish company can develop.

My life at Heriot-Watt university would have been painfully worse without my colleagues Adri, Pascu, Salva, Viki, Chechu, Jose, Rafa, Maria, Estela, Rosie, Dave, Julia, Costas, Zhou Zhou, Ibrahim, Spiros, Jessi, Alex and many other ISSS folks.

I specially thank my parents, grandparents, and the rest of my family for their support over so many years. Thank you for planting the seed of my curiosity and scepticism. I am also in debt to my family-in-law for their support and care. The Spanish provisions made these years abroad more bearable.

I feel deeply indebted to Isabel, my partner in life, my love and mother of both this thesis and a wonder named Leo. Thank you for your continuous encouragement, endless patience and invaluable sacrifice. Over these years, you have been the glue of our family and every single page of this thesis.

Carlos F. Lopez
Edinburgh, September 2019.

ACADEMIC REGISTRY
Research Thesis Submission
Please note this form should be bound into the submitted thesis.

Name*:*	Carlos Fernando Lopez Martinez		
School:	School of Engineering and Physical Sciences		
Version: *(i.e. First, Resubmission, Final)*	Final	Degree Sought:	Doctor of philosophy

Declaration

In accordance with the appropriate regulations I hereby submit my thesis and I declare that:

1. The thesis embodies the results of my own work and has been composed by myself
2. Where appropriate, I have made acknowledgement of the work of others
3. Where the thesis contains published outputs under Regulation 6 (9.1.2) these are accompanied by a critical review which accurately describes my contribution to the research and, for multi-author outputs, a signed declaration indicating the contribution of each author (complete Inclusion of Published Works Form – see below)
4. The thesis is the correct version for submission and is the same version as any electronic versions submitted*.
5. My thesis for the award referred to, deposited in the Heriot-Watt University Library, should be made available for loan or photocopying and be available via the Institutional Repository, subject to such conditions as the Librarian may require
6. I understand that as a student of the University I am required to abide by the Regulations of the University and to conform to its discipline.
7. Inclusion of published outputs under Regulation 6 (9.1.2) shall not constitute plagiarism.
8. I confirm that the thesis has been verified against plagiarism via an approved plagiarism detection application e.g. Turnitin.

* *Please note that it is the responsibility of the candidate to ensure that the correct version of the thesis is submitted.*

Signature of Candidate*:*		Date:	16-09-2019

Submission

Submitted By *(name in capitals):*	
Signature of Individual Submitting:	
Date Submitted:	

For Completion in the Student Service Centre (SSC)

Received in the SSC by *(name in capitals):*		
Method of Submission *(Handed in to SSC; posted through internal/external mail):*		
E-thesis Submitted (**mandatory for final theses**)		
Signature:	Date:	

Inclusion of Published Works

Declaration

This thesis contains one or more multi-author published works. In accordance with Regulation 6 (9.1.2) I hereby declare that the contributions of each author to these publications is as follows:

Citation details	C. F. Lopez, C.-X. Wang, and R. Feng, "A novel 2D non-stationary wideband massive MIMO channel model," in *Proc. IEEE CAMAD'16*, Toronto, Canada, Oct. 2016
Author 1	Literature review, theoretical derivations, simulations, results processing and conclusions.
Authors 2 and 3	Advice, review and corrections.
Signature:	
Date:	16-09-2019

Citation details	C. Lopez and C. -X. Wang, "A study of delay drifts on massive MIMO wideband channel models," in *Proc. WSA'18*, Bochum, Germany, Mar. 2018
Author 1	Literature review, theoretical derivations, simulations, results processing and conclusions.
Author 2	Advice, review and corrections.
Signature:	
Date:	16-09-2019

Citation details	Carlos F. Lopez and C.-X. Wang, "Novel 3D non-stationary wideband models for massive MIMO channels," *IEEE Trans. Wireless Commun.*, vol. 17, no. 5, pp. 2893-2905, May 2018.
Author 1	Literature review, theoretical derivations, simulations, results processing and conclusions.
Author 2	Advice, review and corrections.
Signature:	
Date:	16-09-2019

Declaration of Authorship

I, Carlos Fernando LÓPEZ MARTINEZ, declare that this thesis titled, 'Massive MIMO Channel Models for 5G Wireless Communication Systems and Beyond' and the work presented in it are my own. I confirm that:

- This work was done wholly while in candidature for a research degree at Heriot-Watt University.

- Where I have consulted the published work of others, this is always clearly attributed.

- Where I have quoted from the work of others, the source is always given. With the exception of such quotations, this thesis is entirely my own work.

- I have acknowledged all main sources of help.

- Where the thesis is based on work done by myself jointly with others, I have made clear exactly what was done by others and what I have contributed myself.

Signed:

Date: 16-09-2019

Contents

Contents

List of Figures

List of Tables

Abbreviations

2D	two-dimensional
3D	three-dimensional
3G	3rd generation
3GPP	3rd Generation Partnership Project
4G	4th generation
5G	5th generation
5GPPP	5th Generation Public Private Partnership
6G	6th generation
AAoA	azimuth angle of arrival
AAoD	azimuth angle of departure
ACF	auto-correlation function
AoA	angle of arrival
AoD	angle of departure
B5G	beyond 5G
BD	birth-death
BS	base station
CBSM	correlation based stochastic model
CDF	cumulative distribution function
CIR	channel impulse response

CN	condition number
COST	European Cooperation in Science and Technology
CTF	channel transfer function
DFT	discrete Fourier transform
DoA	direction of arrival
DoD	direction of departure
DS	delay spread
EAoA	elevation angle of arrival
EAoD	elevation angle of departure
ELAA	extremely large aperture array
eMBB	enhanced mobile broadband
FCF	frequency correlation function
FDD	frequency division duplexing
GBSM	geometry-based stochastic model
i.i.d.	independent and identically distributed
IEEE	Institute of Electrical and Electronics Engineers
IMT	International Mobile Telecommunications
IS-GBSM	irregular-shape geometry-based stochastic model
ITU-R	International Telecommunications Union Radiocommunication sector
KBSM	Kronecker-based stochastic model
KPI	key performance indicator
LoS	line-of-sight
LTE-A	Long Term Evolution Advanced

M-MMSE	multicell minimum mean-squared error
MBC	multi-bounce cluster
MBCM	map-based channel model
MEA	method of equal areas
MIMO	multiple-input multiple-output
mMTC	massive machine-type communication
mmWave	millimetre wave
MPC	multi-path component
MS	mobile station
MU-MIMO	multi-user multiple-input multiple-output
NLoS	non-line-of-sight
PAS	power angular spectrum
PDF	probability density function
PDP	power delay profile
PSD	power spectral density
RF	radio frequency
RMS	root mean square
RS-GBSM	regular shape geometry-based stochastic model
RSM	Riemann sum method
Rx	receiver
S-CCF	spatial cross-correlation function
SBC	single-bounce cluster
SCM	spatial channel model
SE	spectral efficiency
SF	scattering function
SISO	single input single output

SNR	signal-to-noise ratio
ST-CCF	spatial-temporal cross-correlation function
STF-CCF	spatial-temporal-frequency cross-correlation function
STV	space-time varying
TDD	time division duplexing
ToA	time of arrival
Tx	transmitter
UCA	uniform cylindrical array
UDSM	unified disk scattering model
UE	user equipment
ULA	uniform linear array
UPA	uniform planar array
URA	uniform rectangular array
URLLC	ultra-reliable low-latency communication
US	uncorrelated scattering
VCR	virtual channel representation
VMF	von Mises Fisher
VR	visibility region
w.r.t.	with respect to
WINNER	Wireless World Initiative New Radio
WSS	wide-sense stationary

Symbols

$\vec{a}$, $\boldsymbol{a}$	Vector
$\mathbf{A}$	Matrix
$(\cdot)^{\mathrm{T}}$	Transpose of a matrix/vector
$(\cdot)^{\mathrm{H}}$	Hermitian transpose of a matrix/vector
$\lvert\lvert \cdot \rvert\rvert$	Euclidean norm
$\mathcal{B}(N, p)$	Binomial distribution with parameters N and p
$\max(\cdot)$	Maximum value of a set
$\min(\cdot)$	Minimum value of a set
$\mathbb{E}\left[\cdot\right]$	Statistical expectation
$I_0(\cdot)$	Zeroth-order modified Bessel function of first kind
$\Gamma(k, \theta)$	Gamma distribution with shape parameter k and scale θ
$\mathcal{L}N(\mu, \sigma)$	Log-normal distribution with parameters μ and σ
$\mathcal{N}\mathcal{B}(r, p)$	Negative binomial distribution with parameters r and p
$\otimes$	Kronecker product of matrices
$\sum$	Summation
$\delta(\cdot)$	Dirac delta function
$u(\cdot)$	Unit-step function
$\mathcal{U}(a, b)$	Uniform distribution in the interval $[a, b]$
A_p^{T}	pth transmit-side antenna element
A_q^{R}	qth receive-side antenna element
$\boldsymbol{a}_p^{T}$	Position vector of A_p^{T} w.r.t. the transmit array's center

$\boldsymbol{a}_q^R$	Position vector of A_q^{R} w.r.t. the receive array's center
α^{T}	Azimuth orientation angle of the transmit array
α^{R}	Azimuth orientation angle of the receive array
β^{T}	Zenith orientation angle of the transmit array
β^{R}	Zenith orientation angle of the receive array
c_0	Speed of light
$\mathrm{C}_c^{\mathrm{S_T}}$	cth single-bounce cluster at the transmit side
$\mathrm{C}_c^{\mathrm{S_R}}$	cth single-bounce cluster at the receive side
$\mathrm{C}_c^{\mathrm{M_T}}$	cth multi-bounce cluster at the transmit side
$\mathrm{C}_c^{\mathrm{M_R}}$	cth multi-bounce cluster at the receive side
D_A	Largest dimension of the array
D_n^T	Distance between the transmit array's center and S_n
D_n^R	Distance between the receive array's center and S_n
$D_{n,p}^T$	Distance between A_p^{T} and S_n
$D_{n,q}^R$	Distance between A_p^{R} and S_n
$D_{n,qp}$	Distance from A_p^{T} to A_q^{R} via S_n
$D_{c,n,p}^\ell$	Distances between A_p^{T} and $\mathrm{S}_{c,n}^\ell$ with $\ell \in \{\mathrm{S_T, M_T}\}$
$D_{c,n,q}^\ell$	Distances between A_q^{R} and $\mathrm{S}_{c,n}^\ell$ with $\ell \in \{\mathrm{S_R, M_R}\}$
δ_{T}	Antenna element spacing at the transmit side
δ_{R}	Antenna element spacing at the receive side
δ_H^R	Horizontal antenna element spacing at the receive side
δ_V^R	Vertical antenna element spacing at the receive side
Δt	Time difference or lag
Δf	Frequency difference
$g_{mn,qp}$	Gain of the ray-level path A_p^{T}–$\mathrm{S}_{m,n}$–A_q^{R}
$\gamma_{c,qp}^{\mathrm{L}}$	Shadowing process of line-of-sight component between A_p^{T} and A_q^{R}
$\gamma_{c,qp}^\ell$	Shadowing process of C_c^ℓ with $\ell \in \{\mathrm{SB, MB}\}$ between A_p^{T} and A_q^{R}
$\Gamma(k,\theta)$	Gamma distribution of parameters k, θ
ζ_c^ℓ	Zenith angle of the velocity of C_c^ℓ with $\ell \in \{\mathrm{S_T, S_R, M_T, M_R}\}$
ζ^{R}	Zenith angle of the velocity vector of the Rx
$\boldsymbol{H}$	Channel matrix

h_{qp}	Channel impulse response between A_p^{T} and A_q^{R}
H_{qp}	Channel transfer function between A_p^{T} and A_q^{R}
θ_c^{ℓ}	Zenith angle of C_c^{ℓ} with $\ell \in \{\mathrm{S_T}, \mathrm{S_R}, \mathrm{M_T}, \mathrm{M_R}\}$ at the array's center
$\theta_{c,n}^{\ell}$	Zenith angle of $\mathrm{S}_{c,n}^{\ell}$ with $\ell \in \{\mathrm{S_T}, \mathrm{S_R}, \mathrm{M_T}, \mathrm{M_R}\}$ at the array's center
θ^{L}	Zenith angle of the Rx at the transmit array's center
κ	Concentration parameter of the von Mises distribution
λ	Carrier wavelength
$\lambda_{V,c}^{\ell}$	Appearance transition rate of C_c^{ℓ} with $\ell \in \{\mathrm{SB}, \mathrm{MB}\}$
$\lambda_{I,c}^{\ell}$	Disappearance transition rate of C_c^{ℓ} with $\ell \in \{\mathrm{SB}, \mathrm{MB}\}$
μ^{ϕ}	Mean of the angular distribution of the scatterers
μ^{r}	Mean of the radial distribution of the scatterers
μ^{x}	Mean of the x-component of the distribution of the scatterers
μ^{y}	Mean of the y-component of the distribution of the scatterers
m_c^{ℓ}	Area mean of $\gamma_{c,qp}^{\ell}$ with $\ell \in \{\mathrm{SB}, \mathrm{MB}\}$
N_T	Number of antennas elements of the array at the Tx
N_R	Number of antennas elements of the array at the Rx
ν	Doppler frequency
ν_{qp}^{L}	Doppler shift of the line-of-sight between A_p^{T} and A_q^{R}
$\nu_{c,n,p}^{\ell}$	Doppler shift of $\mathrm{S}_{c,n}^{\ell}$ with $\ell \in \{\mathrm{S_T}, \mathrm{M_T}\}$ measured at A_p^{T}
$\nu_{c,n,q}^{\ell}$	Doppler shift of $\mathrm{S}_{c,n}^{\ell}$ with $\ell \in \{\mathrm{S_R}, \mathrm{M_R}\}$ measured at A_q^{R}
ξ_c^{ℓ}	Azimuth angle of the velocity of C_c^{ℓ} with $\ell \in \{\mathrm{S_T}, \mathrm{S_R}, \mathrm{M_T}, \mathrm{M_R}\}$
ξ^{R}	Azimuth angle of the velocity vector of the Rx
Π_{qp}^{L}	Reappearance process of the line-of-sight between A_p^{T} and A_q^{R}
$\Pi_{c,qp}^{\ell}$	Reappearance process of C_c^{ℓ} with $\ell \in \{\mathrm{SB}, \mathrm{MB}\}$ between A_p^{T} and A_q^{R}
r_{L}	Distance between the centres of the transmit- and receive arrays
r_c^{ℓ}	Distance from transmit array's centre and C_c^{ℓ} with $\ell \in \{\mathrm{S_T}, \mathrm{M_T}\}$
r_c^{ℓ}	Distance from receive array's centre and C_c^{ℓ} with $\ell \in \{\mathrm{S_R}, \mathrm{M_R}\}$
R_{mn}^{R}	Radius of the ray-level visibility region (VR) corresponding to S_{mn}
S_n	nth scatterer
$\mathrm{S}_{c,n}$	nth scatterer in the cth cluster
$\mathrm{S}_{c,n}^{\mathrm{S_T}}$	nth scatterer in the cth single-bounce cluster at the transmit side

$\mathrm{S}_{c,n}^{\mathrm{S_R}}$	nth scatterer in the cth single-bounce cluster at the receive side
$\mathrm{S}_{c,n}^{\mathrm{M_T}}$	nth scatterer in the cth multi-bounce cluster at the transmit side
$\mathrm{S}_{c,n}^{\mathrm{M_R}}$	nth scatterer in the cth multi-bounce cluster at the receive side
σ^τ	SD of the delay or DS
σ^r	SD of the radial distribution of the scatterers
σ^x	SD of the x-component of the distribution of the scatterers
σ^y	SD of the y-component of the distribution of the scatterers
σ_c^ℓ	Shadowing standard deviation of $\gamma_{c,qp}^\ell$ with $\ell \in \{\mathrm{SB}, \mathrm{MB}\}$
t	Time
T_{mn}^R	Lifetime of the ray-level path A_p^T–$\mathrm{S}_{m,n}$–A_q^R
τ	Propagation delay
$\tau_{n,qp}$	Propagation delay from A_p^T to A_q^R via scatterer S_n
τ_{VL}	Propagation delay of the virtual link
$\boldsymbol{v}_{c,n}^\ell$	Velocity vector of $\mathrm{S}_{c,n}^\ell$ with $\ell \in \{\mathrm{S_T}, \mathrm{S_R}, \mathrm{M_T}, \mathrm{M_R}\}$
$\boldsymbol{v}^\mathrm{R}$	Velocity vector of the Rx
ϕ^L	Azimuth angle of the Rx w.r.t. the transmit array's centre
ϕ_n^T	Azimuth angle of S_n w.r.t. the transmit array's centre
ϕ_n^R	Azimuth angle of S_n w.r.t. the receive array's centre
ϕ_c^ℓ	Azimuth angle of C_c^ℓ with $\ell \in \{\mathrm{S_T}, \mathrm{S_R}, \mathrm{M_T}, \mathrm{M_R}\}$ at the array's center
$\phi_{c,n}^\ell$	Azimuth angle of $\mathrm{S}_{c,n}^\ell$ with $\ell \in \{\mathrm{S_T}, \mathrm{S_R}, \mathrm{M_T}, \mathrm{M_R}\}$ at the array's center

Chapter 1

Introduction

1.1 Background

1.1.1 The 5G wireless communications and beyond

Over the last decades, the ever-growing demand for low-latency, high-density, and high-capacity ubiquitous wireless communication services has fueled the steady development of new technologies whose capabilities have doubled every two and a half years, in agreement with Cooper's law. Recent studies on global data traffic estimated 18 billion connected devices in 2017, 2.4 per capita, and forecast more than 25 billion by 2022, 12 billion of which will be mobile [1]. A relative comparison across multiple generations of wireless telecommunication technologies indicate that mobile connections of the 4th generation (4G) generated about three times more traffic than those of the 3rd generation (3G) in 2017. A similar ratio is expected between the 5th generation (5G) and 4G global data traffic by 2022. A relative temporal analysis reveals a 17-fold growth in the global mobile data traffic per month from 2012 to 2017 and a 7-fold increase is expected from 2017 to 2022, as shown in Figure 1.1 A).

The enhancement of existing wireless communication technologies and development of new ones, such as machine to machine communications, intelligent transportation systems and wireless networks of sensors, are expected to bring remarkable benefits

1
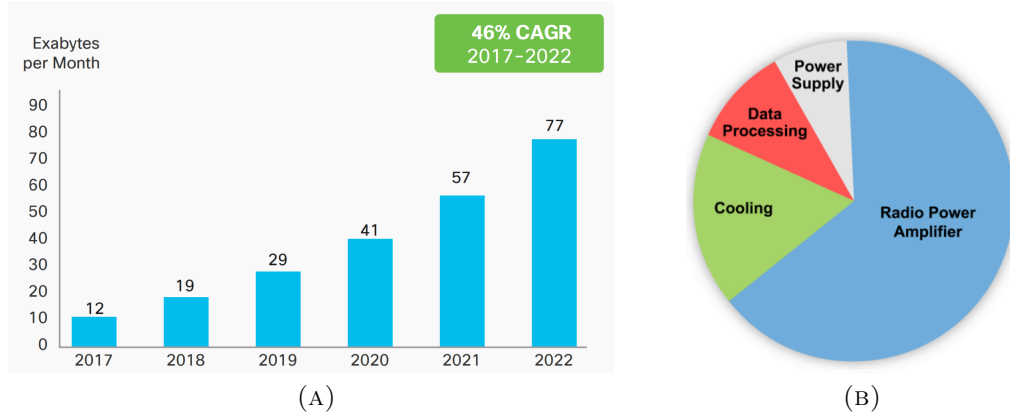
FIGURE 1.1: A) Global mobile data traffic per month from 2017 to 2022 in [1] and B) how wireless networks use electricity in [2].

to many aspects of our everyday lives. However, this progress is usually hindered and driven by technological and ethical challenges. Among the most important, the scarcity of fundamental resources such as the radio frequency (RF) electromagnetic spectrum and the damaging environmental footprint of information and communication technologies guide the development of the 5G wireless communication technologies and beyond. Studies on energy usage of communications networks showed that they add up to 1-3% of the world's total energy consumption and their environmental impact may become a major problem in the future. Wireless networks are typically less energy efficient than wired or optical networks as power-hungry RF amplifiers are employed to overcome the usually large propagation losses. Figure 1.1 B) breaks down the typical energy consumption of current wireless networks [2].

According to the 5th Generation Public Private Partnership (5GPPP) formed by the European Commission, 5G networks need to be designed, engineered and optimised by relying on innovative technologies capable of providing 1000 times higher capacity and a 90% reduction in energy consumption compared to the standards of the 4G to cope with the increase of mobile data traffic and to reduce the carbon emission footprint of mobile communications [17]. Similarly, the International Telecommunications Union Radiocommunication sector (ITU-R) published the International Mobile Telecommunications (IMT) Vision for 2020 and beyond [18], listing the minimum requirements of key performance indicators (KPIs) for 5G (IMT-2020) compared to the 4G (IMT-Advanced) wireless technologies as shown in Figure 1.2 A).

(A)

(B)
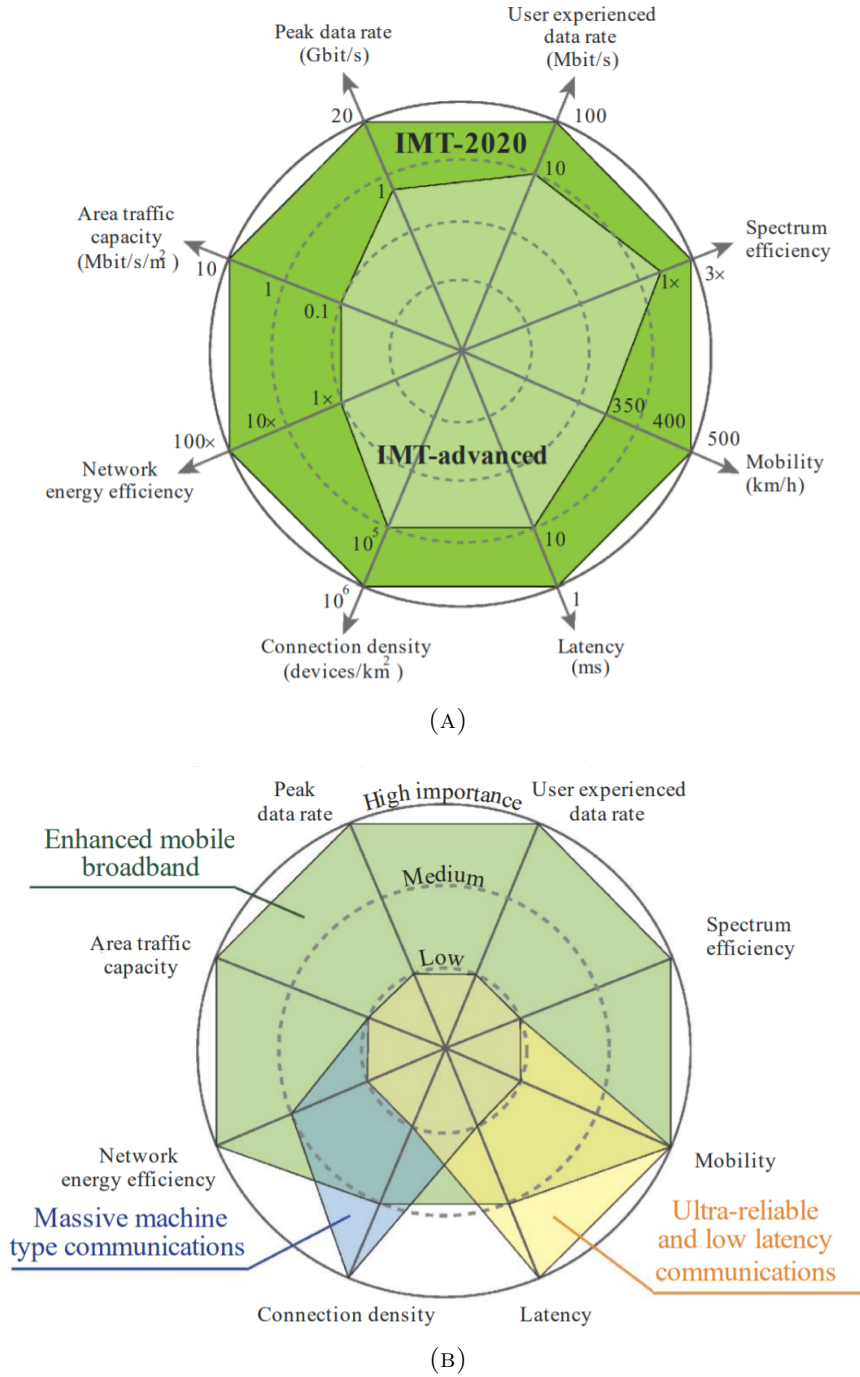
FIGURE 1.2: A) Enhancements of key capabilities from 4G to 5G and B) importance of key capabilities per use case.

As these requirements are very stringent and they cannot be all met at the same time using a single technology, multiple solutions have been proposed for different use cases. For that purpose, IMT Vision [18] put forward a classification of the three main usage scenarios for future 5G technologies: enhanced mobile broadband (eMBB), ultra-reliable low-latency communication (URLLC), and massive machine-type communication (mMTC):

- **eMBB**: It is considered an evolution of IMT-Advanced Mobile Broadband, i.e., human-centric communications for access to multimedia content, services and data, with improved user data-rate, high mobility and seamless coverage.

- **URLLC**: It is characterised by high reliability, high mobility and very low latency. The data rate requirements are less stringent when compared to eMBB. Examples are industrial manufacturing, robotics, and transportation safety.

- **mMTC**: A scenario with a very large number of low-powered devices transmitting a low volume of latency-insensitive data. Examples of this use case are sensor networks.

The importance of each capability for every use case is depicted in Figure 1.2 b). For the main use case (eMBB), different solutions have been proposed to increase the network data transmission capacity and spectrum and energy efficiencies. Among them, increasing the cell density by deploying cells of reduced coverage area, enhancing the spectrum utilisation, shifting the carrier frequency upwards to exploit larger bandwidths available and increasing the spectrum efficiency are the most important.

At a high investment cost, increasing the cell density (*cell densification*) is an effective approach to improve the network capacity in the past by spectrum reuse [19]. Cell densification mitigates the environmental footprint by reducing the energy consumption of RF amplifiers, as the closer the users are to the access network, the lower the path losses that need to be compensated. The limit of this approach is usually called the *single-user limit* and it occurs when each cell only serves one user. Beyond this

point, further densification would require a very large degree of cell activity management and the capacity gains would turn from linear to logarithmic as spectrum-reuse gains would be replaced by signal-to-noise ratio (SNR) gains [20].

With an increasingly clogged spectrum at conventional RF bands (0.4-6 GHz), smart dynamic spectrum allocation using cognitive radio and millimetre wave (mmWave) technologies operating at frequency bands beyond 30 GHz have also been proposed to increase the spectrum efficiency and network capacity, respectively. Cognitive radio technology aims at improving spectrum utilisation by exploiting information about the environment such as the activity of other nodes which share the same spectral resources [21]. Communications at mmWave frequencies can benefit from the large amount of spectrum available, but their coverage is usually limited by the difficult propagation conditions and reduced effective area of constant-gain antennas [22]. Nonetheless, ultra-dense cellular networks may leverage the characteristics of mmWave propagation by reducing inter-cell interference. For macro-cellular coverage, multiple-input multiple-output (MIMO) technologies can help overcome the propagation difficulties through beamforming techniques [23].

In addition to the aforementioned technologies, MIMO antenna technologies have demonstrated to be decisive to alleviate the scarcity of RF spectrum over the last decades. MIMO technologies introduced new degrees of freedom and a new domain (space) to the communication that can be exploited for multiplexing purposes without detriment to other limited resources, e.g., time or bandwidth. Whereas spatial multiplexing techniques have contributed to the remarkable increase in the spectral, energy and economic efficiencies of modern wireless communication systems, space-time coding helped improve their reliability [24]. A relatively small number of antenna elements are supported by current standard wireless communication systems, e.g., Long Term Evolution Advanced (LTE-A) of the 3rd Generation Partnership Project (3GPP) currently supports up to 8 parallel streams of data (layers) and antenna ports in the downlink per user [25]–[27]. In Release-15 of the 3GPP, 5G New Radio technologies can support up to 32 antenna ports in the downlink in a multi-user setup [27], [28]

and larger number is expected in subsequent releases beyond 5G (B5G), as recent Release-16 3GPP Study Items seem to indicate [29].

1.1.2 Massive MIMO: A key enabler of 5G and beyond

Recently, an increasing interest in the characteristics of massive MIMO, i.e., MIMO technologies that employ from hundreds to thousands of antennas, has appeared both in academia and industry due to some remarkable properties that many-antenna systems theoretically show. Some of these promising properties are [30]–[32]:

- **Spectral efficiency**: On a time-frequency varying channel, the achievable data-rate of a MIMO antenna system scales as $\min(M_T, M_R)\log(1+\text{SNR})$, where M_T and M_R denote the number of transmit and receive antennas, respectively, and SNR is the signal-to-noise ratio.

- **Reliability**: On a quasistatic channel, diversity schemes can greatly improve the reliability of a point-to-point link as the probability of link outage scales according to $\text{Prob}(\text{link outage}) \propto \text{SNR}^{-M_T M_R}$.

- **Energy-cost efficiency**: For a fixed transmitted power, the power per antenna element is inversely proportional to the number of antennas. With a large ratio of base station (BS) antennas to terminals, near-constant envelope signaling that requires cheap and efficient RF amplifiers can be used.

- **Interference reduction**: For a fixed inter-element spacing, the higher the number of BS antennas, the better the focusing capabilities of an antenna array. Thus, the electromagnetic field strength can be focused to a point rather than in certain direction, leading to less interference between spatially separated users.

Consequently, massive MIMO technologies have been recently proposed as one of the key enablers of 5G and B5G wireless communications. Nevertheless, these promising capabilities are not exempt of practical implementation challenges that have to be tackled before these systems can be practically deployed. Some of the most important challenges are listed below [31], [33]:

- **Spatial constraints**: The number of BS antennas is constrained by the available space where they can be deployed. Important benefits of massive MIMO, e.g., increased array gain, spatial resolution, and diversity order, depend on the total size of the antenna array and require a sufficient separation between adjacent antenna elements [34]. The limited space becomes a challenge at low frequencies as arrays composed by hundreds of antennas can become bulky.

- **Channel acquisition overhead**: The uplink channel estimation overhead is proportional to the number of user equipments (UEs) and the downlink one is proportional to the number of BS antennas in frequency division duplexing (FDD) schemes. Although FDD massive MIMO schemes seem unpractical, reciprocity-based time division duplexing (TDD) schemes do not suffer such overhead. However, it has been shown that the channel estimation quality per antenna cannot be reduced by adding more antennas to the BS.

- **Signal processing overhead**: The complexity of signal processing tasks such as channel estimation, equalisation, and precoding (beamforming) scales linearly with the number of BS antennas and the number of UEs.

- **Pilot contamination**: As the number of orthogonal training sequences (pilots) assigned to UEs for channel estimation and precoding is limited by the characteristics of the time-frequency-varying channel, these are reused in adjacent cells. Pilot reuse *contaminates* channel estimates and therefore produces UE interference when beamforming is used. This interference grows with the number of antennas and complex multi-cell signal processing is required to eliminate it.

- **Deployment of many parallel transmit/receive RF chains**: Massive MIMO requires the integration of many compact RF chains: up/down converters, analog-to-digital and digital-to-analog converters, etc. This will require a highly efficient economy of scale in manufacturing.

1.2   Motivation

In order to study some of these challenges and take advantage of them in the design of new transmission schemes, there has been a substantial progress on channel measurements and models involving both virtual and real massive MIMO systems. These measurements campaigns revealed that large-scale antenna arrays (in the order of tens of wavelengths) of different shapes and number of antennas exhibit new channel characteristics that affect important metrics like the achievable data rate and reliability of MIMO communication systems (see Section 2.1).

Furthermore, since the early years of wireless communications, channel models have played an important role in the design and evaluation of new communication systems, enabling both development and deployment in quicker and more economical manners. However, traditional standard channel models such as those developed by the Wireless World Initiative New Radio (WINNER) and European Cooperation in Science and Technology (COST) actions (see Section 2.2) neglected some of these new channel features such as near-field and non-stationary effects when many antennas are used on the transmit or receive sides. Consequently, models capable of capturing fundamental characteristics of massive MIMO channels in different environments and situations are required. Although recent works on channel modelling have partially filled that gap, there are still important unaddressed aspects of massive MIMO channel models with respect to their accuracy, flexibility and complexity.

The main goal of this PhD project is to study the propagation characteristics of wireless communication channels when many antennas are employed in one or both sides of the communications link and incorporate these characteristics into flexible, accurate and efficient channel models that can be used to assess and design new wireless transmission technologies.

1.3 Contributions

The key contributions of this thesis are summarised as follows:

Contributions of Chapter 3: A Study of Non-Stationary Massive MIMO Channels by Transformation of the Delay and Angular Power Spectral Densities

- Propose a general transformation method to study and model massive MIMO channels using the distribution of the delay and angle of arrival (AoA) and two-dimensional (2D) arbitrary-shaped arrays. Closed-form expressions of key statistical properties of widely-used massive MIMO channel models such as the scattering function (SF), auto-correlation function (ACF) and Doppler power spectral density (PSD) are derived.

- Study of the drifting and spreading of the distribution of the delay and AoA over large-scale arrays of widely-used scatterers distributions. It is shown that the delay drift and spread over the array lead to an array-varying frequency correlation function (FCF).

Contributions of Chapter 4: Novel 3D Non-Stationary Massive MIMO Channel Models based on Cluster-Level Evolution

- Propose a three-dimensional (3D) non-stationary wideband massive MIMO channel model. Parabolic wavefronts are proposed to reduce the mathematical and computational complexity of massive MIMO channel models.

- Propose a cluster-evolution process to model large-scale fading over the array, including cluster of multipath components (re)appearance and shadowing.

- Derive a 3D extension of the parameter computation method called the Riemann sum method (RSM). The amplitude and angular parameters of the 3D simulation model are obtained.

Contributions of Chapter 5: A Novel 3D Non-Stationary Massive MIMO Channel Model based on Ray-Level Evolution

- Propose a 3D non-stationary wideband massive MIMO channel model. The model incorporates a ray-level evolution process to capture space-time evolution of individual multi-path components (MPCs) or rays. The proposed model is suitable for 3D extremely large aperture array (ELAA). Close-form expressions of the statistical properties of the ray-level evolution process and analysis of the impact of its parameters on them.

- Propose a wavefront selection criterion for each cluster and MPC that can improve the efficiency of both existing and B5G massive MIMO channel models by greatly reducing the need for spherical wavefronts.

1.4   Original Publications

The work presented in this thesis has led to the following publications:

- **C. F. Lopez**, C.-X. Wang, and R. Feng, "A novel 2D non-stationary wideband massive MIMO channel model," in *Proc. IEEE CAMAD'16*, Toronto, Canada, Oct. 2016.

- L. Bai, C.-X. Wang, S. Wu, **C. F. Lopez**, X. Gao, W. Zhang, and Y. Liu, "Performance comparison of six massive MIMO channel models," in *Proc. IEEE/CIC ICCC'17*, Invited Paper, Qingdao, China, Oct. 2017.

- **C. F. Lopez** and C. -X. Wang, "A study of delay drifts on massive MIMO wideband channel models," in *Proc. WSA'18*, Bochum, Germany, Mar. 2018.

- F. Lai, **C. F. Lopez**, X. Gao, C.-X. Wang, and F. Zheng, "Analysis of performances for three massive MIMO channel models," in *Proc. WCSP'18*, Hangzhou, China, Oct. 2018.

- **C. F. Lopez** and C.-X. Wang, "Novel 3D non-stationary wideband models for massive MIMO channels," *IEEE Trans. Wireless Commun.*, vol. 17, no. 5, pp. 2893–2905, May 2018.

- **C. F. Lopez** and C.-X. Wang, "A study of 2D non-stationary massive MIMO channels by transformation of delay and angular power spectral densities," *IEEE Trans. Wireless Commun.*, under review.

- **C. F. Lopez** and C.-X. Wang, "A non-stationary 3D wideband massive MIMO channel model based on ray-level evolution," *IEEE Trans. Commun.*, to be submitted.

1.5 Thesis Organisation

The remainder of this thesis is organised as follows:

Chapter 2 reviews the state-of-the-art literature on massive MIMO channel measurements and models. First, new propagation phenomena of massive MIMO channels that have been discovered in measurements campaigns will be reviewed and key differences between conventional and massive MIMO channels will be presented. Second, this chapter will provide a comprehensive classification of channel models according to their approach. Techniques used by recent massive MIMO stochastic models to capture these new phenomena will be analysed and major limitations highlighted. From this analysis, the research gap motivating this research work will be identified.

Chapter 3 investigates fundamental properties of massive MIMO channels. This chapter will present a transformation method to model the space-time varying (STV) distributions of time of arrival (ToA) and AoA. Next, the method will be employed to study multiple array-variant properties of three widely-used geometry-based stochastic models (GBSMs): the Unified Disk, Ellipse, and Gaussian scattering models. The

chapter continues by introducing a simplified channel modelling approach based on STV parameters of the AoA distribution. Finally, a validation of the proposed methods through numerical and simulation results of the statistical properties of these three GBSMs is provided.

Chapter 4 presents a novel 3D non-stationary wideband geometry-based stochastic theoretical channel model for 5G massive MIMO communication systems. A second-order approximation to the spherical wavefront, i.e., the parabolic wavefront, is introduced to capture near-field effects. Next, the chapter develops a cluster evolution process comprising both cluster (re)appearance and large-scale fading over the array. A corresponding simulation model will be derived along with a 3D extension of the RSM for parameters computation. The most important statistical properties of the proposed model will be derived and analysed. In addition, the accuracy and flexibility of the proposed model will be demonstrated by comparing simulation results and measurements of the delay spread, cluster power variations, and size of VRs.

Chapter 5 introduces a flexible space-time non-stationary 3D wideband massive MIMO channel model for B5G communications based on a single sub-cluster level approach capable of modelling near-field effects, (dis)appearance, and cluster-level large-scale fading. Additionally, an improved Rayleigh-distance criterion to determine the most adequate wavefront for each cluster and ray is presented. The chapter continues by deriving key statistical properties of the channel, including the ACFs, Doppler PSD, spatial cross-correlation functions (S-CCFs), and FCFs, and analysing the impact of the ray-level evolution process on them. The validation of the derived statistical properties through numerical and simulation results and conclusions close the chapter.

Finally, Chapter 6 summarizes important conclusions of the work presented in this PhD thesis. In addition, this chapter concludes by proposing future lines of research on the field of massive MIMO channel modelling identified by the author.

Chapter 2

Massive MIMO Channel Modelling: Literature Review

This chapter presents a review of the state-of-the-art literature on massive MIMO channel measurements and models. Specifically, it introduces the fundamental differences between conventional and massive MIMO channel characteristics, classify multiple channel modelling techniques and present recent contributions in channel modelling to capture those new characteristics. From this analysis, a research gap motivating this work is identified.

2.1 Massive MIMO Channel Measurements

In recent years, many research groups have developed prototypes to evaluate the suitability of massive MIMO large-scale antenna systems as a solution to overcome the challenges of future wireless communications [3]–[6], [8], [16], [35]–[46]. Measurements campaigns have revealed unexpected channel effects that must be considered in order to achieve an optimal operation of modern wireless communication systems involving channel estimation, scheduling, resource allocation, modulation and coding scheme selection. The following sections will summarize the outcomes of these massive MIMO channel measurements. New channel characteristics related to the large size of the

antenna arrays such as the non-stationary effects along the array, spherical wave propagation and correlation effects will be introduced.

2.1.1 Non-stationary properties of the channel over the array

Massive MIMO measurement campaigns have demonstrated that channels cannot be regarded as wide-sense stationary (WSS) over antenna arrays spanning long distances compared to the carrier wavelength. In essence, this means that small-scale channel characteristics such as the local-average received power, delay, Doppler and angular spectra do not remain constant over large-scale arrays composed of hundreds of antenna elements. *Near-field effects* have been pointed out to be the cause of some of these new characteristics. Near-field effects appear when a source of electromagnetic waves (or an intermediate scatterer) are located within the near-field region of a receiving antenna. The radiative near-field and far-field regions are delimited by the so-called Rayleigh or Fraunhofer distance, beyond which wavefronts can be accurately approximated by a plane surface. The far-field or Rayleigh distance of an antenna is typically defined as

$$D_F = 2D_A^2/\lambda \tag{2.1}$$

where D_A is the maximum dimension of the antenna, e.g., its length in the case of a linear antenna, and λ the carrier wavelength. The near-field effects that have empirically been demonstrated are the following:

- **Spherical wave propagation** takes its name from the shape adopted by the wavefronts — surfaces of equal phase — in the near-field region. In conventional MIMO wireless communications, antenna arrays are composed of few elements of similar size to the carrier wavelength, which is usually between 5 cm and 50 cm. Thus, even in urban environments, scatterers and mobile stations (MSs) are usually beyond the Rayleigh distance of the array and plane wavefronts are sufficiently accurate for channel modelling purposes. However, when

a large-scale antenna array spanning tens of wavelengths is employed, spherical wavefronts may need to be considered. In that case, significantly different AoAs and propagation delays can be observed at different antenna elements of the array, i.e., MPCs or *rays* reaching largely separated antenna elements are not approximately parallel. Figure 2.1 illustrates these concepts with a uniform linear array (ULA). The waves transmitted by the MS are scattered by a nearby object and arrive at antennas 1 and 2 of the ULA at similar angles α and α', respectively, but at a very different angle α'' for a largely separated antenna element (N). Whereas the phase difference between waves reaching antennas 1 and 2 can be expressed as $\Delta\Phi_{1,2} = \frac{2\pi}{\lambda}d_{1,2} \approx \frac{2\pi}{\lambda}\delta\cos(\alpha)$, this linear approximation of their phase difference is inaccurate for largely separated antennas.

- **Scatterers (dis)appearance (blockage) and shadowing** refers to the fact that signals received by different antenna elements of a large array interact with different sets of scatterers or clusters of scatterers in the environment and can be blocked by them. The concept of clusters of scatterers is based on the fact that multipath components tend to appear in groups in various domains such as the delay and angular ones. The term *shadowing* or large-scale fading denotes
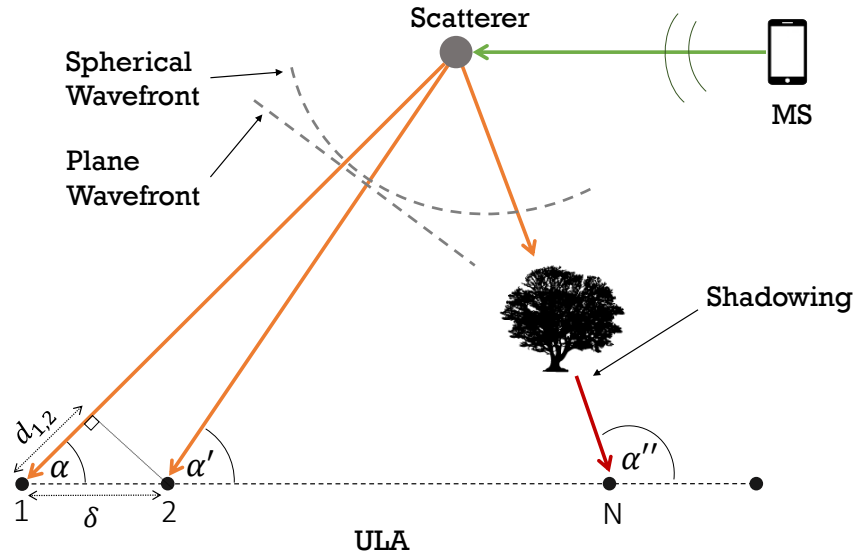
FIGURE 2.1: AoA variations and shadowing over a large ULA. As rays are not parallel for every antenna element of the array, spherical wavefronts are required.

variations of the local-average mean power of the received signal and transitions between line-of-sight (LoS) to non-line-of-sight (NLoS) communications. The distance over which shadowing needs to be considered depends on the type of environment and it usually ranges from a few to tens of wavelengths for urban and rural environments, respectively [47]. Conventional arrays formed by few antenna elements are hardly affected by shadowing over the array, but massive MIMO arrays are likely to span tens of wavelengths and therefore shadowing is likely to be present. This phenomenon has also been termed cluster (of scatterers) disappearance or birth-death (BD) of clusters by referring to the technique usually employed to model it, i.e., Markov BD processes. In Figure 2.1, it is shown how an object (tree) can significantly obstruct or reduce the signal strength for a particular set of antennas of the ULA but not for others.

A large number of massive MIMO channel measurements demonstrated that large-scale antenna arrays often result in wireless channels that cannot be regarded as WSS [3]–[6], [8], [16], [41]–[46], [48]–[54]. Measurements employed virtual ULAs [3], [5], [6], [16], [41], [44], [51]–[53], uniform cylindrical arrays (UCAs) [3], [8], [16], [41], [54], and uniform planar arrays (UPAs) [4], [41], [45], [46], [48]–[50], [53], [54] at a single frequency band, e.g, 2.6 GHz [3], [5], [6], [8], [16], and at multiple frequency bands, e.g., 11, 16, 28, and 38 GHz [45], and demonstrated multiple array-varying channel characteristic such as AoA and angle of departure (AoD), propagation delays, received power, Rician K-factor, and the number of MPCs.

In [3], Gao *et al.* conducted a measurement campaign with 128-element virtual ULA and UCA at 2.6 GHz of carrier frequency. Figures 2.2 A) and B) show the large-scale antenna arrays employed for this measurement campaign. The authors observed significant smooth variations of the AoA of the MPCs at different antenna elements, a phenomenon also referred to as *angular drift*, when the LoS component or strong reflected MPCs were present. In NLoS conditions, they showed that certain clusters of scatterers were not observable in the angular or delay spectra over the whole array as they *appeared* and *disappeared* at different antenna elements, so each antenna element may experience slightly different environments. These effects can be seen in the power
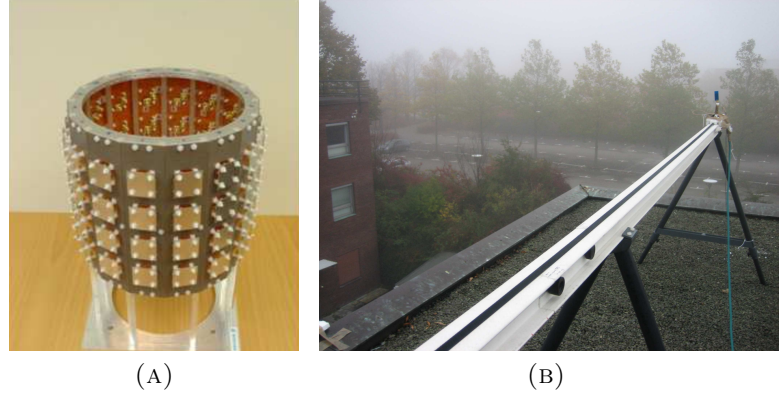
FIGURE 2.2: Large-scale antenna arrays used in [3]. A) A UCA with 128 patch antenna elements and B) a virtual ULA with 128 omni-directional antenna positions.
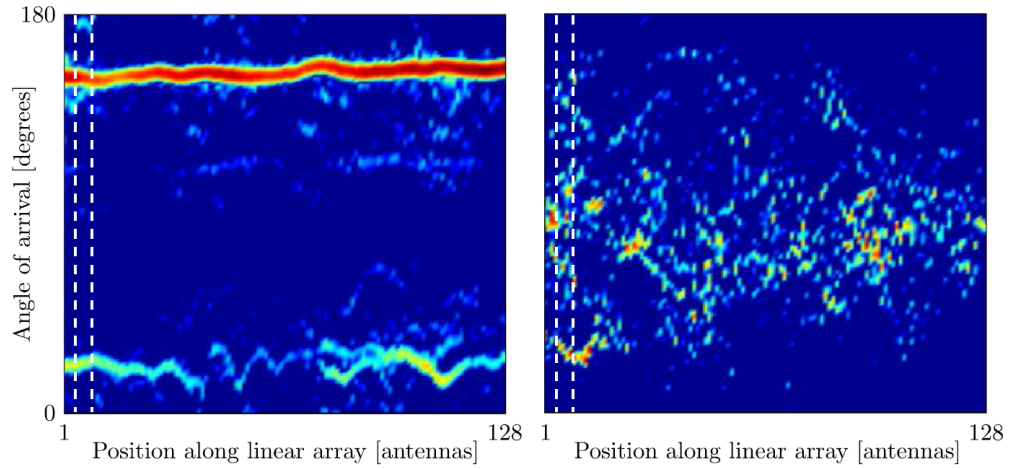
FIGURE 2.3: Angular power spectrum along a 128-element ULA. A) LoS B) NLoS scenario in [3].

spectrum of the AoA in Figure 2.3 and allow to empirically justify the non-stationary properties of the channel.

Additionally, recent measurements employed advanced clustering and sub-cluster tracking algorithms to show the existence of massive MIMO effects of both clusters and individual scatterers and MPCs as well [4]. Figure 2.4 A) shows the MPC-level evolution of the azimuth angle of departure (AAoD) across a 4-by-64 element uniform rectangular array (URA) at 6 GHz of carrier frequency. The MPC-level (dis)appearance process was characterized by an exponential cumulative distribution function (CDF) of the observed MPC length across the array as shown in Figure 2.4 B).

The angular drift of MPCs has been confirmed by many other measurements [6], [44],

17
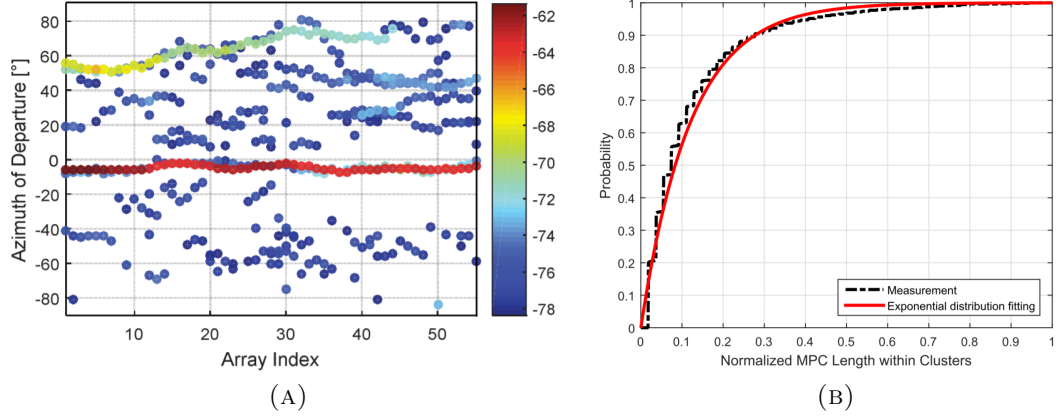
FIGURE 2.4: A) Estimated AAoD from SAGE algorithm across the URA. Each solid dot represents a multipath component. The dB-scaled power of the multipaths is represented by colour. B) CDF of the observed MPC length over the array, with the corresponding Exponential distribution fitting. The MPC length is normalized according to the observed cluster length [4].
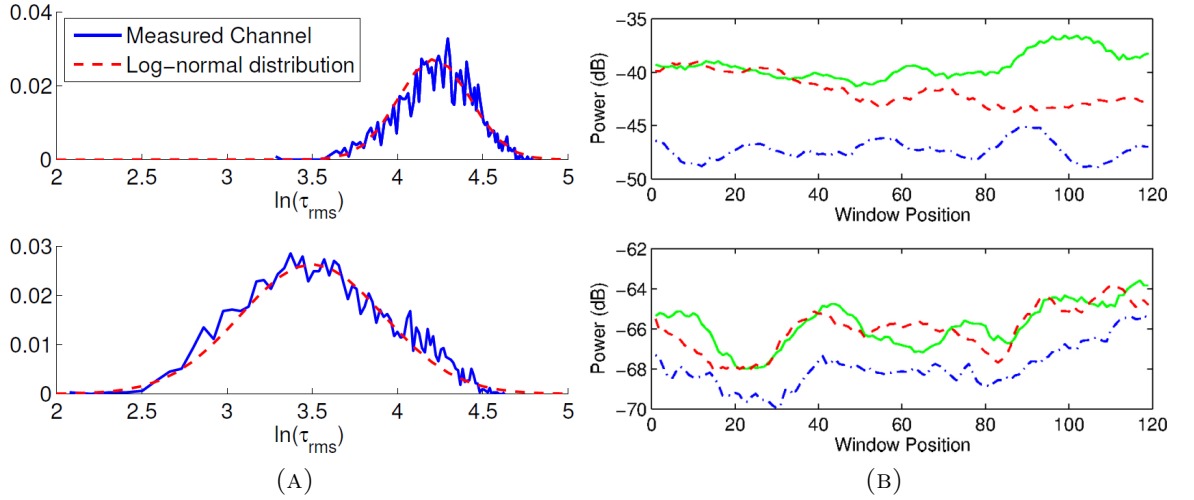
FIGURE 2.5: A) Measured histogram of the RMS DS in LoS (top), NLoS (bottom) scenario, and the approximated Log-normal PDF in [5]. B) Channel gain over the array for different users in LoS (top) and NLoS (bottom) situations, in [6].

[48], [51]. In [6], the authors found channel gain variations of 4-6 dB, Rice K-factor variations of 0.3-0.5, and MPCs angular drifts of 20 degrees along the array. Authors in [5], [49], [52], [55] also showed that a fundamental parameter for the characterization of wideband channels, the root mean square (RMS) delay spread (DS), varies along the array and a good agreement was found by modelling its probability density function (PDF) using a Log-normal distribution Log-$\mathcal{N}(3.67, 0.41)$ at 2.6 and 5 GHz in [5]. Some of the effects described are shown in Figure 2.5.

Channel gain and RMS DS variations are more pronounced in NLoS than in LoS situations. Since the LoS signal usually conveys more energy than the rest of MPCs in LoS situations, differences in clusters sets perceived by different antenna elements represent a small fraction of the total received power. Consequently, these differences have a lower impact on the stationary properties of the channel. However, a small change in the number of MPCs in NLoS situations is more relevant because that change represents a higher fraction of the total received power.

In [42], authors compared a ULA with a UCA at 2.6 GHz and confirmed the previous results. They also showed that the ULA experiences larger power variations over the measured bandwidth compared to the UCA. This is partly justified by the directivity of the antennas, as the directional antenna elements in the UCA are exposed to limited scattering in the angular domain as compared to the omnidirectional ones in the ULA.

Although there are no measurements available in the literature yet, it is expected that near-field effects will be even more accentuated in B5G cell-free massive MIMO [56] and ELAA [57] systems equipped with thousands of distributed low-cost antenna elements, as an array could span hundreds or even thousands of wavelengths [7]. An illustration of a possible deployment of ELAA in B5G systems is shown in Figure 2.6.
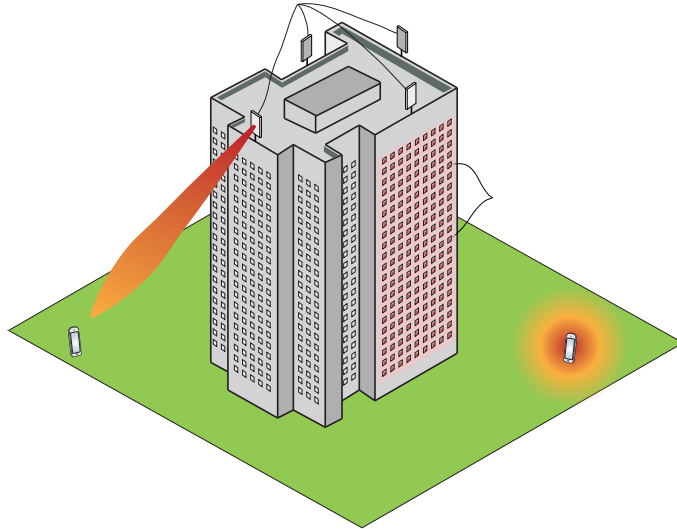
FIGURE 2.6: A future B5G massive MIMO deployment including compact arrays and ELAA in [7].

2.1.2 Correlation and channel hardening

The correlation coefficient between two channel impulse responses (CIRs) or channel vectors can be interpreted as a measure of the cross-talk between these two channels when spatial multiplexing transmission techniques are employed. Thus, it can be seen as an indicator of the unlikeness of the environments experienced by the signals received from different antennas or users. In general, the proximity of two antennas or users leads to highly correlated signals, which makes difficult to distinguish them in the spatial domain for multiplexing purposes. In multi-user multiple-input multiple-output (MU-MIMO) systems, the correlation between two channel vectors corresponding to spatially separated users at positions i, j is given by [8]

$$\rho_{i,j} = \frac{|\boldsymbol{h}_i^H \boldsymbol{h}_j|}{\|\boldsymbol{h}_i\|\|\boldsymbol{h}_j\|} \tag{2.2}$$

where $\boldsymbol{h}_i$ is a column vector representing the channel vector for the ith UE. The operators $\|\cdot\|$ and $(\cdot)^H$ denote the euclidean norm and the Hermitian or conjugate transpose, respectively. As it has been pointed out, a low correlation between the channel vectors at two different positions enables to simultaneously serve different UEs with little cross-talk.

Important spectral and energy efficiency gains can be achieved using massive MIMO technologies under favourable propagation conditions [32]. In short, favourable propagation conditions require that the elements of $\boldsymbol{h}_i$ to be independent and identically distributed (i.i.d.) random variables with zero mean and unit variance. Authors in [8] partially confirmed the existence of favourable propagation as their results showed that channel vectors become more orthogonal as the number of antennas grows with different antenna configurations, shapes and radiation patterns. As it is shown in Figure 2.7 A), the correlation coefficient between any two channel vectors decreases as the number of BS antennas increases and it is close to the correlation of the channel vectors whose coefficients are i.i.d. random variables of zero mean and unit variance.

Although the correlation between i.i.d. channel vectors converges to zero as the number of antennas increases, a saturation phenomena can be observed in real channels where a little cross-talk seems unavoidable. These results were also confirmed by [40].

In addition to the correlation coefficient in (2.2), which evaluates the orthogonality of channel vectors for any two UEs i, j, the joint orthogonality of multiple channel vectors can be measured through the condition number (CN) of $\boldsymbol{H}^H \boldsymbol{H}$ where $\boldsymbol{H} = [\boldsymbol{h}_{i_1} \cdots \boldsymbol{h}_{i_K}] \in \mathbb{C}^{N,K}$ is the channel matrix whose columns are the channel vectors for every UE (i_K) and N denotes the number of antenna elements in the BS array. The CN is defined as follows [8]

$$\kappa_{K,N} = \frac{\text{max. eigenvalue of } \boldsymbol{H}^H \boldsymbol{H}}{\text{min. eigenvalue of } \boldsymbol{H}^H \boldsymbol{H}}. \tag{2.3}$$

The CN is a widely-used indicator for the performance of linear precoders [8]. An inverse CN close to one indicates that the channel vectors or columns of $\boldsymbol{H}$ are nearly orthogonal. As it is shown in Figure 2.7 b), the inverse CN increases with the number of antennas if the ratio of the BS antennas to UEs remains large. In general, although the marginal gain of an additional antenna quickly diminishes in real systems, the authors in [8] showed that most of the benefits of massive MIMO could be realized over measured channels.
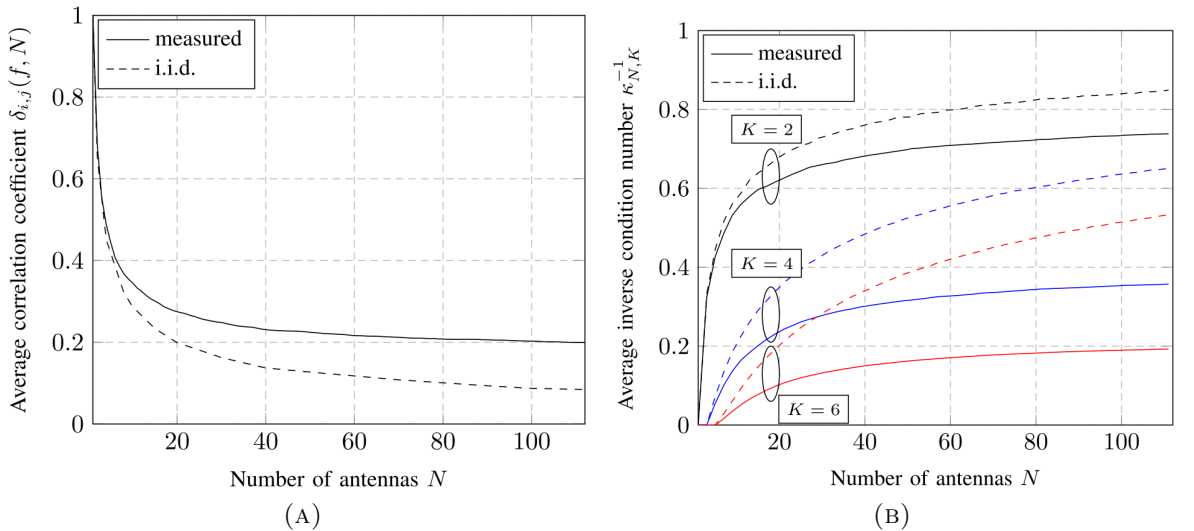
FIGURE 2.7: A) Correlation coefficient between channel vectors and B) average inverse CN as a function of the number of antennas in [8].

Channel hardening refers to the fact that the eigenvalues of the channel matrix and channel capacity become deterministic quantities as the number of transmit and receive antennas grows large and their ratio remains fixed. Channel hardening makes communications performance less dependent of small-scale fading and more dependent of large-scale fading [58, Section 2.2]. The same authors have shown that spatial correlation decreases the level of channel hardening observed for a given number of antennas, i.e., more antennas would be required to approximate asymptotic channel hardening under spatially correlated fading than with i.i.d. Rayleigh fading. Channel hardening has empirically been demonstrated in [36], [37], [59] and it has been shown in [36] that it leads to a linear increase in spectral efficiency (SE) with the number of antennas as long as the ratio of transmit/receive antennas remains large. Similar results were also confirmed by researchers in [41], [60], [61].

2.2 Massive MIMO channel modelling

Channel models assist the design and analysis of new communication systems. They represent cost-effective tools —in many cases the only one— for engineers and researchers to assess the performance of novel algorithms, transmission and coding schemes, compared to complex and expensive measurement campaigns. However, the assumptions on the propagation aspects that must be considered or neglected by the channel model determine the conclusions withdrawn from theoretical and simulation results. For example, it was theoretically proved in [62] that excessive simplification of channel models had misled many researchers on the capacity of massive MIMO systems. In addition, it was shown that an accurate characterization of near-field effects, spatial correlation and large-scale fading over the array is essential as they enable substantial advantages in large dimensional signal processing such as simple detection algorithms, e.g., pilot contamination or large-scale fading precoding, that can achieve unbounded SE even under pilot contamination conditions [58], [62], [63].

This section classifies different channel modelling techniques and describes some of the most relevant MIMO channel models and their limitations. In addition, a general view of preliminary works on massive MIMO channel models is also provided.

Channel models are usually classified by the modelling approach into **deterministic** and **stochastic**. On the one hand, deterministic models are completely defined by deterministic parameters and aim to model the propagation of electromagnetic waves in a specific environment or situation. They usually require detailed information about the environment, e.g., elevation maps, buildings, vegetation, and materials, to provide accurate predictions of the channel properties and they are computationally complex. On the other hand, stochastic channel models aim to represent a broad set of situations or environments at a time by using random variables as parameters that account for the properties of different environments. These are simplified models that usually require information regarding the statistical properties of different environments, which is often obtained by conducting measurement campaigns. An overview of this classification is shown in Figure 2.8.
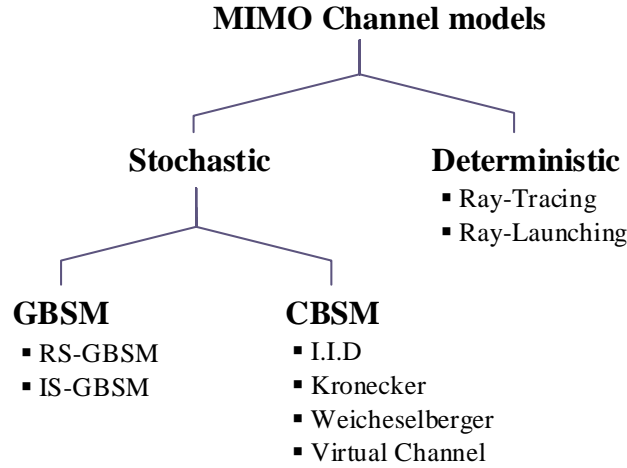
FIGURE 2.8: Classification of MIMO channel models.

2.2.1 Deterministic channel models

Deterministic models enable to simulate multiple propagation paths in relatively low-complex and small-scale environments very accurately. As these channel models employ intense computational geometry algorithms to calculate multiple propagation

paths between every antenna pair in the communication link, conventional deterministic MIMO channel models use a simple single input single output (SISO)-to-MIMO extrapolation principle. Such simple linear-varying phase extrapolation is equivalent to the use of plane wavefronts that, as introduced in Section 2.1.1, does not allow to capture near-field effects.

METIS project developed a map-based channel model (MBCM) that employs ray-tracing to extend the capability of the channel model (initially based on a stochastic approach) to support the massive MIMO prediction requirements [9]. One example of the proposed calculation is shown in Figure 2.9. Compared to the stochastic approach, deterministic channel models can accurately capture local and specific non-stationary properties of the channel by considering a realistic environment at the cost of a high computational complexity. Although ray-based deterministic models are computationally complex and the conclusions obtained from their results are limited to specific environments, they can be a valuable complement to evaluate new MIMO algorithms. The modelling of specular paths is an important asset of ray-based models for mmWave communications, as they will largely depend on these type of paths. However, as illustrated in Figure 2.10 and stressed in [10], the number of simulated rays and the level of complexity supported by the model (combining reflections and diffractions) significantly affect the prediction of the MIMO channel capacity. Since the path of each ray is traced for each antenna pair, massive MIMO channel characteristics such as near-field effects can be captured by the model. Channel capacity and
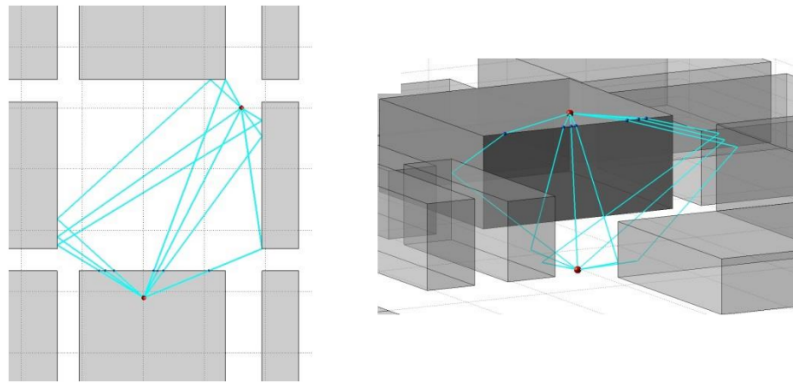
FIGURE 2.9: Illustration of the METIS ray-tracing channel model proposed in [9].
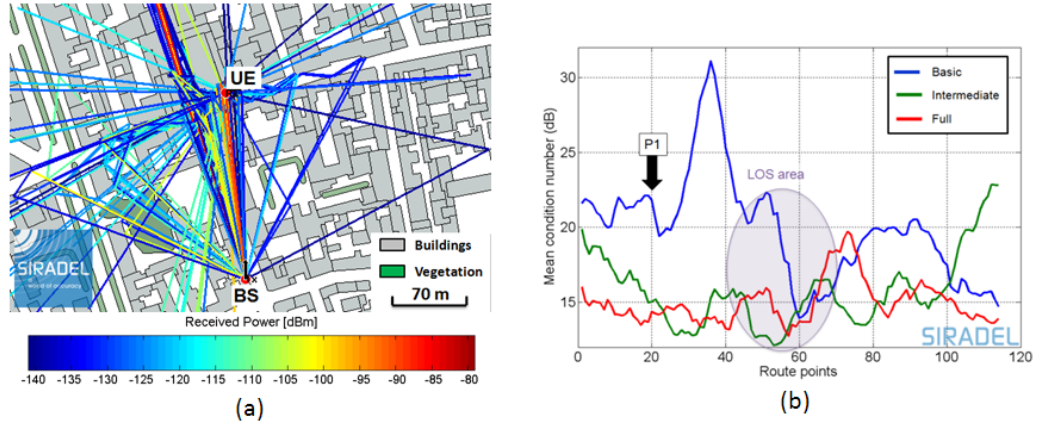
FIGURE 2.10: Impact of complexity of model on the MIMO prediction; A) MPC for a single link in [10]; B) CN along a street for three levels of complexity.

eigenvalue analysis in [64] showed that plane wavefronts are not suitable for large-scale antenna arrays and models should be enhanced with spherical wavefronts.

According to [9], a trade-off between complexity and accuracy must be reached when considering the level of details of deterministic models. However, detailed high resolution data could be important to model environment-specific non-stationary properties of the channel that affect massive MIMO systems performance. This will be more critical at mmWave frequency bands, where the blocking effect is strongly accentuated.

As the large number of antenna elements makes deterministic models time consuming in complex scenarios, authors in [65] proposed to improve the accuracy-complexity-flexibility trade-off by splitting the array in multiple smaller arrays to later compute rays at several reference points in the antenna array before extrapolation. In general, one major limitation today in the 5G MBCM devoted to massive MIMO systems is the lack of validation [66], which requires to run ray-tracing simulations and to collect a large set of channel measurements in the same environment.

2.2.2 Stochastic channel models

Stochastic channel models are usually further classified as **correlation based stochastic models (CBSMs)** and **geometry-based stochastic models GBSMs**. In CB-SMs, the spatial correlation properties of the channel are explicitly defined and they

can be used to generate multiple correlated MIMO CIRs. In general, it is the structure and properties of the spatial correlation matrix what determines the different types of CBSMs. Unlike CBSMs, GBSMs consider simplified geometric properties of the channel and compute the CIRs by using the law of wave propagation applied to specific transmitter (Tx), receiver (Rx) and scatterer geometries. From these CIRs, the statistical properties of the channel can be obtained. The regularity of the geometry defining the environment allows to further classify models into regular shape geometry-based stochastic models (RS-GBSMs) and irregular-shape geometry-based stochastic models (IS-GBSMs), respectively. In both cases, some of the properties of the channel are defined in a stochastic manner according to certain probability distributions that determine the different types of GBSMs and their correlation properties. Geometry based models are usually more accurate than CBSMs at the cost of higher computational complexity.

2.2.2.1 Correlation-based channel models

Correlation models employ eigenvalue decomposition of a predefined MIMO correlation matrix to generate CIRs through its Karhunen-Loeve expansion [58]. Due to its simplicity and mathematical tractability, the so-called i.i.d. Rayleigh fading model has extensively been used to obtain closed-form expressions of important metrics such as the MIMO channel capacity. However, this simplified model assumes that all channel links are uncorrelated, which would be realistic only if the antenna elements of the array were sufficiently separated in a rich scattering environment. As this is not usually the case, unrealistic results that overestimate the channel capacity have been obtained using the i.i.d. Rayleigh fading model [67]. Consequently, more accurate but simple CBSMs have been proposed, including the Kronecker-based stochastic model (KBSM), the virtual channel representation (VCR) and Weichselberger models.

In the KBSM, it is assumed that the direction of departure (DoD) and direction of arrival (DoA) of a MPC are independent. As a consequence, the correlation between channels links can be expressed as the Kronecker product of the correlation matrices at the transmit and receive sides, which are considered uncoupled [68]. The channel

matrix with N_R receiving and N_T transmitting antennas can expressed as

$$\boldsymbol{H} = \boldsymbol{R}_R^{\frac{1}{2}} \boldsymbol{H}_w \boldsymbol{R}_T^{\frac{1}{2}} \tag{2.4}$$

where $\boldsymbol{H}_w$ is an $N_R \times N_T$ matrix with zero-mean unit-variance complex i.i.d. Gaussian entries, and $\boldsymbol{R}_T = \mathbb{E}[\boldsymbol{H}^H \boldsymbol{H}]$ and $\boldsymbol{R}_R = \mathbb{E}[\boldsymbol{H} \boldsymbol{H}^H]$ denote the overall spatial correlation matrices at the transmit and receive, respectively.

In the conventional KBSMs, since all the transmitting (receiving) antenna elements implicitly share the same set of scatterers and their locations are not explicitly defined, non-stationary properties of the channel such as delay and angular drifts as well as scatterers (dis)appearance along the array cannot be easily modelled. The use of the KBSM to model large-scale antenna systems showed discrepancies in the predicted capacity and the joint spatial DoD-DoA spectra which are likely to be more pronounced as the number of antennas grows [69]. The authors in [70] studied the applicability conditions of the KBSM and they demonstrated that different radiation patterns of the transmitting and receiving antennas weakens the separability assumption of the KBSM, making them inappropriate for massive MIMO channel characterization. However, recent efforts have been made in [71] to develop a massive MIMO Kronecker model that improves the capacity estimation. This model incorporated clusters of scatterers (dis)appearance effects along the array into the spatial correlation matrices, but it did not consider spherical wavefronts. Examples of use of the conventional KBSM in standards can be found in LTE-A [25] and Institute of Electrical and Electronics Engineers (IEEE) 802.11 TGn [72].

The VCR model describes the channel using spatial basis functions defined by fixed virtual angles that are limited by the spatial resolution of the arrays [11]. In Figure 2.11 an schematic of the channel model is presented. The $N_T \times N_R$ size channel matrix $\boldsymbol{H}$ representing a channel with N_T transmit and N_R receive antennas is determined by virtual channel coefficients h_{qp}^v via a 2D Fourier Transform as follows

$$\boldsymbol{H} = \sum_{q=-\tilde{N}_T}^{\tilde{N}_T} \sum_{q=-\tilde{N}_R}^{\tilde{N}_R} h_{qp}^v a_R(\tilde{\theta}_{R,q}) a_T(\tilde{\theta}_{T,p})^H = \tilde{\boldsymbol{A}}_R \boldsymbol{H}^v \tilde{\boldsymbol{A}}_T^H \tag{2.5}$$

where $\tilde{N}_T = (N_T - 1)/2$ and $\tilde{N}_R = (N_R - 1)/2$, denote the number of fixed virtual directions depending on the number of antenna elements, the matrices $\tilde{\boldsymbol{A}}_R(\tilde{\boldsymbol{A}}_T)$ are $N_T \times N_T$ ($N_R \times N_R$) in size and, if the principal period of the virtual angles $\tilde{\theta}_{R,q}$ ($\tilde{\theta}_{T,p}$) is sampled uniformly, they are full rank unitary Fourier matrices. In such a case, the corresponding AoAs and AoDs are not uniformly sampled. The virtual channel coefficients matrix $\boldsymbol{H}^v$ represent the coupling between N_T virtual transmit and N_R virtual receive angles and it is the 2D Fourier Transform of $\boldsymbol{H}$. Although the accuracy of this model increases with the number of antennas [73], as long as the model depends solely on DoD-DoA measured from the centre of the array (far-field assumption) and the path gains remain the same for every antenna element, it might be difficult to include new non-stationary properties of the channel over the array. Also, as pointed out by [11], VCR is restricted to single polarized ULAs.

Finally, the Weichselberger model is inspired by and generalizes both the KBSM and VCR model [69]. This model relaxes the separability constraint of the Kronecker model and has the ability to include channel correlations at both the transmit and receive sides. In this model, a mutual coupling matrix between spatial correlation matrices at the Tx and Rx enables to model the joint DoD-DoA spectra. This approach predicted a variety of channel metrics more accurately than the i.i.d., KBSM and VCR models [73]. The Weichselberger model includes the KBSM model by constraining the coupling matrix to be rank one and can be reduced to VCR model by using discrete Fourier transform (DFT) matrices as eigenbases [69]. In the Weichselberger model,
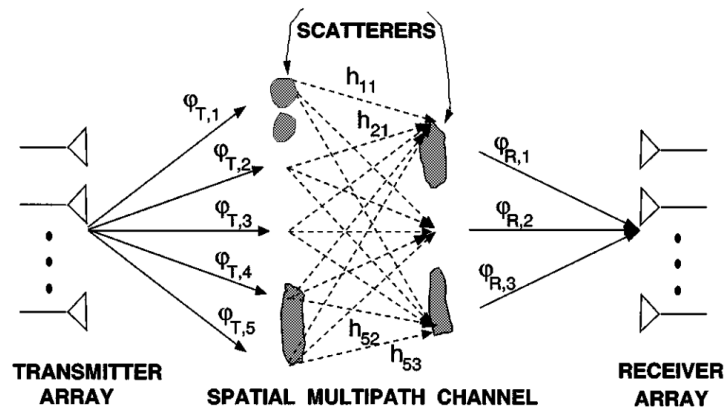
FIGURE 2.11: Schematic of the physical representation of the VCR model in [11].

the channel matrix can be written as

$$\boldsymbol{H} = \boldsymbol{U}_R(\tilde{\boldsymbol{\Omega}} \odot \boldsymbol{G})\boldsymbol{U}_T \qquad (2.6)$$

where $\boldsymbol{G}$ is a random matrix with i.i.d. zero-mean complex-normal entries with unit variance, $\boldsymbol{U}_R$ ($\boldsymbol{U}_T$) denotes the spatial eigenbasis at the receive (transmit) side, and $\tilde{\boldsymbol{\Omega}}$ is the so called *coupling matrix*, which is generally a full-rank matrix consisting of real-valued non-negative elements. The coupling matrix models the amount of energy coupled between eigenvectors of the transmit and receive sides. Unfortunately, the Weichselberger model was designed to model stationary channels, which makes it inappropriate for modelling non-stationary properties along the array.

Compared to other channel modelling approaches, CBSMs are simple, computationally efficient and provide a useful reference for system designers. The drawback of CBSMs comes from the oversimplified unrealistic representation of link correlations. It has been shown [74] that CBSMs tend to be better than other models for calibration purposes due to their balance between complexity and accuracy. However, as current CBSMs do not allow to explicitly define geometrical characteristics of the channel and properties of individual antenna elements, it can be difficult to map new channel characteristics related to the geometry of the environment or the shape/size of the antenna array to the structure of correlation and coupling matrices.

2.2.2.2 Geometry-based channel models

From the definition of the location and properties of the effective scatterers, GBSMs can be further classified into RS-GBSMs and IS-GBSMs. In RS-GBSMs, it is assumed that all the effective scatterers are placed on regular shapes such as a ring, disk, ellipse, etc., and either the Tx or the Rx are usually placed in locations where simple geometrical properties can be leveraged mathematically. GBSMs often result in simple closed-form solutions of important correlation functions of the channel [67], [75].

A geometric shape widely-used for RS-GBSMs is the ellipse. In the Ellipse model, the scatterers are assumed to be distributed on an ellipse and the Tx and Rx are

located at its foci. As the sum of the distances from the foci to any point of the ellipse is a constant, the ellipse allows to model the constant propagation delay of signals travelling from the Tx to the Rx via scatterers.

In Figure 2.12, an example of the Ellipse RS-GBSM for an $N_T \times N_R$ MIMO channel with scatterers S_n placed on an ellipse is depicted. The Tx (Rx) is equipped with a ULA centred on one focus of the ellipse and the distance between adjacent antenna elements is δ_T (δ_R). The Rx moves in the direction indicated by $\vec{v}$. The distance between the two focal points or arrays centres is $2f$ and the semi-major/minor axis lengths of the ellipse are denoted as a and b, respectively. The transmitting (receiving) arrays are tilted by an angle β_R (β_T) with respect to the x-axis and the AoA (AoD) corresponding to the scatterer S_n are denoted by α_n^T (α_n^R). Even though this is not a requirement of the model, the following assumptions are usually made in RS-GBSMs for the shake of simplicity and mathematical tractability.

- The scatterers are beyond the Rayleigh distance (far-field region) of the antenna arrays, i.e., $(N_{T(R)} - 1)\delta_{T(R)} \ll a - f$. As a consequence, the AoDs and AoAs
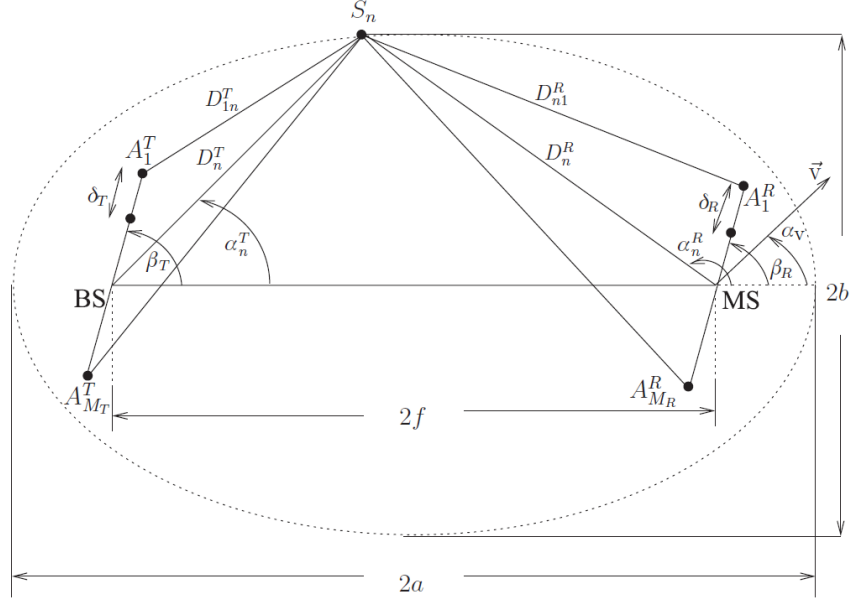
FIGURE 2.12: Geometrical Ellipse scattering model for an $N_T \times N_R$ MIMO channel with local scatterers S_n placed on an ellipse in [12].

are independent of the location of the antenna elements and homogeneous plane wave propagation is assumed.

- The period of time in which this model is valid is short, i.e., $|\vec{v}t| \ll a - f$.

Generally, the CIR of a GBSM can be obtained as the sum of multiple space-time-varying complex exponential functions modelling every path between the Tx and the Rx via scatterers. In the reference model, an infinite number of scatterers following a predefined PDF is assumed. In this case, the CIR of the reference model is usually obtained as [12]

$$h_{qp}(t) = \lim_{N \to \infty} \sum_{n=1}^{N} E_n e^{j(\Theta_n - \vec{k}_n^R \cdot \vec{r}_R(t) - k_0 D_n^{kl})} \qquad (2.7)$$

where E_n and Θ_n denote the path gain and the phase shift caused by the interaction of the nth plane wave with the local scatterer. The symbol $\vec{k}_n^R$ denotes the wave vector and $\vec{r}_R(t)$ the spatial translation vector pointing in the direction in which the Rx is moving. Furthermore, k_0 is the free-space wave number $k_0 = 2\pi/\lambda$. Finally, D_n^{kl} denotes the total length travelled by a plane wave from the lth transmitting to the kth receiving antenna. The simulation model approximates the expression (2.7) using a finite number of complex exponential functions or scatterers for a given complexity-accuracy tradeoff. Although the main advantage of these simple models is their mathematical tractability, recent studies have shown their flexibility to capture space-time non-stationary properties of the channel and near-field effects at the expense of increasing their mathematical and computational complexity [13], [76].

In [13], the authors developed a 2D non-stationary wideband massive MIMO channel model based on the concept of the Ellipse RS-GBSM, in which clusters of scatterers are placed on the edge of confocal ellipses which model delay-resolvable clusters. In Figure 2.13 the depicted model represents visible clusters using blue-coloured paths (observable links) and non-visible ones in red. In this model, spherical wavefronts are considered and a Markov BD random process is used to capture the cluster (dis)appearance over the antenna array and time axes. The results presented in [13] demonstrated some

31

FIGURE 2.13: A wideband ellipse model for massive MIMO systems in [13].

massive MIMO properties such variation of Doppler spread, local-average power variations, and angular drift along the array. The Markov BD random process employed determines the probability of survival of a cluster $P_{survival}^{T(R)}$ and the average number of newly generated clusters $\mathbb{E}[N_{new}^{T(R)}]$ along the array using exponential functions of the antenna separation as

$$P_{survival}^{T(R)} = e^{-\lambda_R \frac{\delta_{T(R)}}{D_c^a}} \tag{2.8}$$

$$\mathbb{E}[N_{new}^{T(R)}] = \frac{\lambda_G}{\lambda_R}(1 - e^{-\frac{\delta_{T(R)}}{D_c^a}}) \tag{2.9}$$

where $\mathbb{E}[\cdot]$ designates the expectation operator, $\lambda_G(m^{-1})$ and $\lambda_R(m^{-1})$ denote the cluster generation and recombination rates, respectively; and D_c^a represents an scenario-dependent correlation factor. In Figure 2.14, an example of cluster (dis)appearance over a ULA is presented.

In [14], the authors developed a non-stationary concentric multi-ring channel model for massive MIMO systems. They considered spherical wavefronts and used a Markov BD process to model cluster (dis)appearance over the array and time domain. In

FIGURE 2.14: An example of cluster evolution over a ULA. The symbol $*$ indicates that an antenna element (in the horizontal axis) can *see* a cluster (in the vertical axis). [13].

Figure 2.15 the model shows visible paths in blue and invisible ones in red colour. In this case, mobility and presence of scatterers are considered only at the transmit side.

Recent works have introduced 3D characteristics of massive MIMO channels into RS-GBSMs [77], [78]. In [77], the authors proposed a double cylinder RS-GBSM including spherical wavefronts and cluster (dis)appearance through visibility areas of spherical shape. Thus, scatterers can interact with the signal transmitted by a given antenna only if the distance from the scatterer to the antenna is smaller than a predefined value (radius of the sphere). In [78], the authors proposed a 3D extension of the Ellipse model by employing an ellipsoid generated as a solid of revolution around the
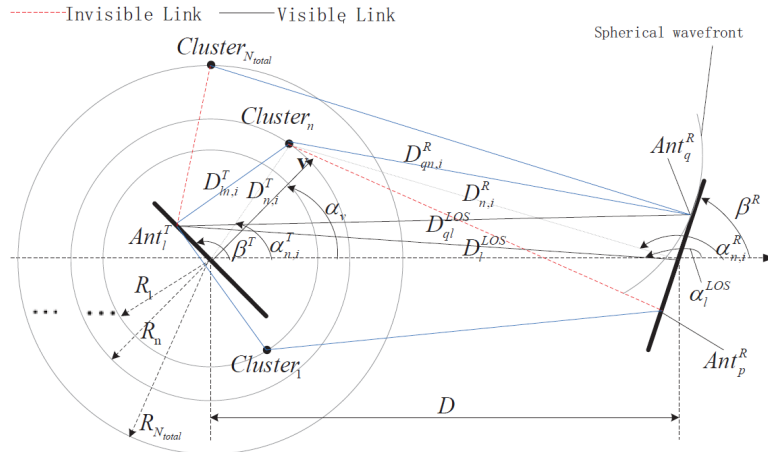
FIGURE 2.15: A wideband multi-ring massive MIMO channel model in [14].

33

straight line passing through the Tx and Rx. This model considers UPAs and includes spherical wavefronts and cluster of scatterers (dis)appearance through a Markov BD processes. Whereas the main advantages of RS-GBSMs are their higher flexibility and accuracy at a relatively low complexity, the introduction of spherical wavefronts and clusters of scatterers (dis)appearance have resulted in more complex and less insightful channel models.

In contrast to RS-GBSMs, **IS-GBSMs** assume clusters of scatterers to be randomly located across the environment. The locations of the scatterers are not constrained by any specific shape and they are usually based on statistical distributions obtained from measurement campaigns. In Figure 2.16 a schematic representation of a IS-GBSM is shown. In this approach, the CIR can similarly be obtained by adding the contribution of every MPC connecting the transmitting and receiving sides via scatterers. A general CIR of a cluster-based IS-GBSM from the transmit antenna p to the receive antenna q can be expressed as

$$h_{qp}(t) = \sum_i \sum_j a_{ij} s_t(\Omega_{ij}) s_r(\Phi_{ij}) \delta(\tau - \tau_i - \tau_{ij}) \tag{2.10}$$

where a_{ij} denotes the complex gain of the jth MPC in ith cluster, $s_t(\Omega_{ij})$ and $s_r(\Omega_{ij})$ are the transmit and receive steering vectors in the DoD Ω_{ij} and DoA Φ_{ij}. The parameter τ_i is the delay experienced by the signal from the Tx to the Rx via the cluster ith, and τ_{ij} accounts for the relative delay of the jth MPC within that cluster.
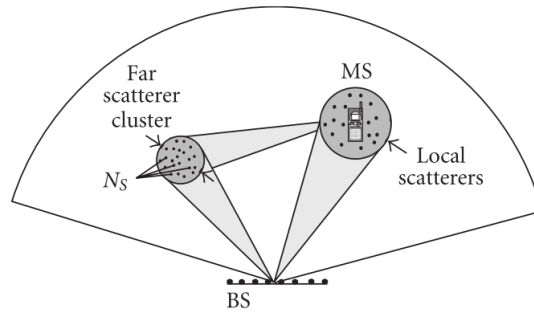
FIGURE 2.16: Principle of the clustered IS-GBSM in [15].

34

In order to decouple angular power spectra of arrival and departure and better model the power delay profile (PDP), multi-bounce components were introduced into IS-GBSMs either by double-directional properties [79] or twin-clusters [80]. The twin-cluster approach assumes two identical representations (twins) of a cluster of scatterers at each side of the communication link and a one-to-one correspondence among the transmit- and receive-side scatterers in each twin cluster. The twin cluster can accurately reflect the relationships between DoDs, DoAs, and delays, and reduces the computational complexity associated to multi-bounce channel models from quadratic to linear form. The twin-cluster model was later incorporated into the standard COST 273 [81], and maintained in COST 2100 channel models [82].

Whereas IS-GBSMs rarely lead to closed-form solutions of important statistical properties of the channel, they are sufficiently accurate and flexible models to adapt to complex environments keeping spatial consistency, i.e., building a coherent propagation environment for multiple UEs located at different positions. Also, they are able to capture non-stationary effects found in massive MIMO measurements easily at the expense of higher computational complexity. Several standard channel models employed this approach in the past [82]–[87]. However, as non-stationary properties of the channel over the array are negligible in conventional MIMO systems, channel models such as those developed in 3GPP-spatial channel model (SCM) [83], WINNER+ [85], IMT-A [86], COST 2100 [82], and 3GPP-3D [87], did not capture them.

Recently proposed IS-GBSMs [9], [88]–[95] aimed at filling that gap. Spherical wavefronts were considered by computing the exact distances between every antenna element of the array and the surrounding scatterers. In addition, in the channel models that addressed large-scale fading over the array [9], [13], [88], [89], [91]–[94], this was captured focusing on the array-varying number of clusters of scatterers only. Thus, Markov BD processes [13], [88], [89], [91], [92], [94] or VRs [9], [90] were employed.

The VR approach was first implemented in COST 259 directional channel model [96] to account for the mobility of UEs. A VR is a region of space, usually of random location and size, where a cluster of scatterers is active or, equivalently, where the signal transmitted or received by an UE interacts with that particular cluster. In [90],

the concept of the VR was extended to the BS array to account for the (dis)appearance effect found in massive MIMO measurements. In this context, if a cluster is *visible* for a particular antenna element, paths involving that specific cluster and antenna element can be formed between the Tx and Rx. In Figure 2.17 the VR approach is represented schematically, in which regions of a particular colour represent a particular VR of a cluster. Clearly, certain elements or subarrays of the BS array share a particular cluster set, so every antenna *observes* a slightly different environment.
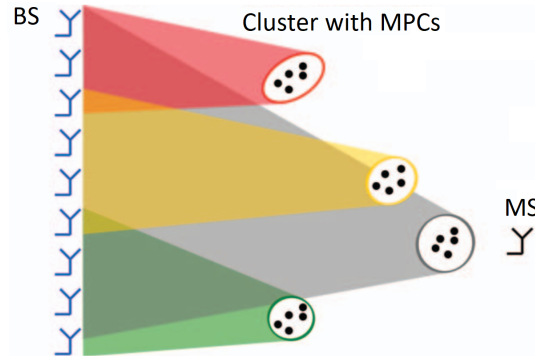
FIGURE 2.17: Concept of cluster VR applied to the BS antenna array [16].

Although the authors in [16] reported a significant large-scale fading over the array in both LoS and NLoS conditions, it is worth noting that very few works considered large-scale power variations of clusters of MPC. In [16], the authors characterized cluster-level large-scale fading using a very simple single-slope model. In [89], the authors developed a general 5G wireless channel model that included MPCs power variations over the array to capture large-scale fading by using an inverse-square law.

In summary, GBSMs demonstrate a good accuracy-complexity-flexibility trade-off when compared to the simple but inaccurate CBSMs and the very complex but precise deterministic map-based channel models. Further details on MIMO channel modelling and advances in massive MIMO channel modelling can be found in [15], [66], [97].

2.3   Research Gap

In the recent works introduced above, the authors proposed novel non-stationary massive MIMO channel models that were able to capture key characteristics of the

channel observed in measurements campaigns. Although near-field effects and large-scale fading over the array have been studied in the literature, there are important aspects of these phenomena that have not been addressed yet.

At the moment, spherical wavefronts are the only technique that has been proposed to model near-field effects and no other simpler, more efficient, and insightful techniques have been suggested. In addition, the most appropriate wavefront (plane or spherical) for a MPC is normally determined by comparing the Rayleigh distance of the array with the distance from the array to a scattering object. Since the Rayleigh distance of an array depends on its largest dimension, spherical wavefronts seem to be necessary for a large percentage of MPCs in most scenarios. However, this approach does not consider the limited lifespan of MPCs over the array. A better understanding of the characteristics of spherical wavefronts and their properties would help discover efficient and precise methods to capture near-field effects only when they are required.

It has been proved in [62] that the inaccurate modelling of spatial correlation and large-scale fading over the array led to the remarkably important but wrong conclusion in numerous studies that massive MU-MIMO capacity is limited by channel estimation interference, i.e., pilot contamination. In particular, the authors showed that the SE provided by multicell minimum mean-squared error (M-MMSE) precoding/combining scheme grows without bound as the standard deviation of the large-scale fading over the array increases, unlike previous studies that considered no large-scale fading over the array. In addition, it was shown in [58, Section 2.2] that the distribution of the small-scale fading has a smaller impact on communication performance than that of large-scale fading as the channel hardening effect increases.

Existing massive MIMO channel models considered large-scale fading over the array as a consequence of cluster of scatterers (dis)appearance only. Thus, those works modelled exclusively the (dis)appearance phenomena by employing either Markov BD processes or VRs. However, it has been pointed out in measurements [16] that clusters of MPCs can also experience large-scale fading over the array. In addition, Markov BD processes and VRs usually model the occlusion of clusters for short intervals over the array as multiple independent clusters [13], [89], [90]. This increases the number

of clusters per simulation and can underestimate the correlation of the channel in the large scale. Both Markov BD and VR approaches predict that the random number of clusters at any location of the array is Poisson distributed. However, measurements reported that a negative Binomial distribution is more accurate [16]. How to resolve this apparent contradiction is still an open question. An approach that can model cluster-level large-scale fading over the array and reappearance effects at the same time would result in a more accurate and efficient description of the shadowing effect.

Although sub-cluster ray-level (dis)appearance over the array was also reported in measurements [4], models including these phenomena and comprehensive studies of its impact on their statistical properties are still missing. The assessment of performance metrics such as the channel capacity of new precoding/combining spatial multiplexing MU-MIMO techniques would benefit from a deeper understanding and more appropriate modelling of these phenomena as demonstrated in [58] and [62].

2.4   Summary

In this chapter, the state-of-the-art massive MIMO measurements and models have been introduced and reviewed. Measurements campaigns revealed fundamental differences between the channel characteristics of conventional MIMO systems employing few antenna elements and massive MIMO systems equipped with large-scale antenna arrays. The key difference is that massive MIMO channels cannot be regarded as WSS over the array as they are subject to near-field effects, i.e., spherical wave propagation, scatterers (dis)appearance and shadowing over the array.

These new channel characteristics fostered the development of highly accurate, flexible and complex channel models. Both deterministic map-based and stochastic channel models can capture massive MIMO channel characteristics. Whereas deterministic models are appropriate for a detailed analysis of concrete environments, their specificity and high computational complexity make stochastic models a more affordable and attractive solution for a broad set of scenarios. Although the mathematical tractability and low complexity of CBSMs compensated for their poor accuracy, their

limited flexibility to adapt and capture new massive MIMO effects has hindered their recent progress. In contrast, the more versatile GBSMs have demonstrated to be sufficiently flexible to incorporate these new channel features with higher accuracy than CBSMs and lower computational complexity than deterministic ones.

Despite the recent progress, fundamental aspects of these new channel effects and models need to be addressed in order to improve their accuracy, efficiency and flexibility. Spherical wavefronts are considered as a flexible approach to model near-field effects, but more efficient methods and criteria to determine when they are required would be beneficial. Markov BD processes and VRs are two fundamental methods to model large-scale fading over the array, but a deeper understanding and accurate modelling of this phenomenon that complements clusters of scatterers (dis)appearance is required to assess the potential benefits of massive MIMO technologies.

Chapter 3

A Study of Non-Stationary Massive MIMO Channels by Transformation of the Delay and Angular Power Spectral Densities

3.1 Introduction

In order to assess and design new wireless communication technologies, it is important to study the underlying propagation channels and incorporate their most relevant features into existing and new channel models. As discussed in Chapter 2, the large size of massive MIMO arrays lead to complex propagation effects, e.g., near-field effects, that were not present in conventional MIMO systems equipped with few co-located antennas. As near-field effects such as the non-linear phase variations over the array due to the angular drifting and shadowing along the array introduce a dependency of the spatial correlation on the absolute position of the antenna elements in the array, massive MIMO CIRs cannot generally be regarded as WSS.

In the past, time-domain non-WSS wireless channels were firstly studied to enable high-mobility communication systems [98], [99], e.g., vehicular and high-speed train [100], due to their rapidly-varying characteristics. Recent high-mobility channel models [101]–[107] employed the so called *parameters drifting*, i.e., time-varying channel

parameters such as ToAs and AoAs, with increased theoretical and computational complexity. Alternatively, the family of COST channel models, e.g., COST 207 [81] and COST 2100 [82], were intrinsically designed as non-stationary in the time domain by computing the location of clusters of scatterers in the environment and the exact distance between these and transceivers. A similar approach was used in recent works on massive MIMO channel modelling that incorporated spherical wavefronts [13], [88], [89]. Spherical wavefronts require computing the exact distances between the scatterers and the antenna elements of the array. Similarly to the parameters-drifting approach, spherical wavefronts capture non-WSS channel properties over the array at the expense of high theoretical and computational complexity. In [13], [88], [89], the authors proposed 2D [13] and 3D [88], [89] wideband massive MIMO GBSMs that used spherical wavefronts, temporal parameter drifting, and space-time Markov BD processes to capture near-field effects and (dis)appearance of clustered MPCs, respectively. However, these works [13], [88], [89] neglected variations of the ToA over the array and did not study the STV distribution of ToA and AoA. The quasi-deterministic channel models QuaDRiGa [91] and mmMAGIC [92] employed a combined approach including spherical wavefronts and temporal parameters drifting. The stochastic COST 2100 [82], METIS [9], 3GPP-NR [93] and IMT-2020 [94] channel models did not consider spherical wavefronts and supported mobility at the MS side only. Although COST 2100 [82] channel model did originally not supported large-scale arrays, its extension [90] incorporates spherical wavefronts and VRs over the array. The map-based deterministic METIS model and the quasi-deterministic MiWEBA [95] channel model implicitly included spherical wavefronts and temporal channel evolution through ray-tracing techniques with high computational complexity. Among these works, delay drifts over the array were only considered in the deterministic map-based METIS [9] and quasi-deterministic QuaDRiGa [91] models. However, these [9], [91] did not study the effects of delay drifts on the statistical properties of massive MIMO channels and none of the works above studied the STV distribution of ToA and AoA.

A novel approach to channel modelling was presented in [108]. The authors employed

the theory of transformation of random variables to investigate the spatial configuration of the scatterers in multiple coordinate systems for predefined joint probability density functions (PDFs) of the AoA and ToA. Similar investigations were conducted in the past for specific GBSMs [109], [110], but they did not study non-WSS channels in space or time domains.

Theoretical studies on the STV joint PDF of the ToA and AoA and space-time parameters drifting for non-WSS massive MIMO channels are still missing. Moreover, the equivalence of the spherical wavefront and parameters drifting approaches to model the statistical properties of massive MIMO channels has not been investigated yet. To fill these gaps, this chapter introduces a general transformation method capable of modelling the STV joint PDF of the ToA and AoA. The proposed method produces analytical expressions of the STV SF, delay and angular PSDs for arbitrary configurations of the scatterers. In addition, this chapter introduces an approximation method to obtain the STV angular spread, which was not considered in previous theoretical studies of massive MIMO channels. The main contributions and novelties of this chapter are the following:

1. A general transformation method to model the STV joint PDF of the ToA and AoA for 2D non-WSS massive MIMO channels is proposed. This method can be used to obtain closed-form expressions of this joint-PDF for the three most common ways of specifying the distribution of the scatterers, e.g., in the ToA-AoA, polar, and Cartesian domains, and for arbitrary-shaped 2D arrays. Through numerical evaluation and simulation, the equivalence of the proposed methods and the spherical-wavefront approach to capture the statistical properties of the channel is demonstrated.

2. Approximate expressions for the STV angular spread of the channel when the AoA follows a von Mises distribution through a geometry-based method are presented. Additionally, new closed-form approximate solutions of key statistical properties of massive MIMO channels, such as the temporal ACF and the Doppler PSD, are obtained by employing the closed-form solutions of the STV angular spread.

3. A study of the STV joint-PDFs of the AoA and ToA of widely-used MIMO GBSMs such as the Ellipse, Unified Disk, and Gaussian scattering models is conducted. In all cases, the joint-PDFs of the AoA and ToA are subject to drifting and spreading over the array. Leveraging on this study, it is shown that the array-varying properties of the FCF of these three GBSMs are caused not only by the disappearance of MPCs, but also by the drift and spread of the ToA over the array.

4. Limitations of existing MIMO GBSMs that were upgraded to simulate massive MIMO channels, e.g., the Unified Disk, Ellipse, and Gaussian scattering models, due to the array-variant characteristics of the joint PDF of the ToA and AoA.

The rest of this chapter is organized as follows. In Section 3.2, the non-stationary wideband massive MIMO channel model employed in the following sections is introduced. Section 3.3 presents the general transformation method for the three most-used coordinate systems. Key statistical properties of the channel are derived using the transformed joint PDF of the ToA and AoA in Section 3.4. Section 3.5 compares important statistical properties obtained through the transformation method, the approximation method, the conventional spherical wavefront approach, and simulation results. Finally, conclusions are summarized in Section 3.6.

3.2 A 2D Wideband Massive MIMO Stochastic Channel Model

Let us consider a 2D wideband massive MIMO channel model depicted in Figure 3.1 where the Tx and Rx are equipped with ULAs. The transmitting (receiving) ULA is composed of N_T (N_R) omnidirectional antenna elements equally spaced with a distance δ_T (δ_R) and it is tilted at an angle α^T (α^R) with respect to (w.r.t.) the x-axis of a Cartesian coordinate system centred at the receiving array's centre. The p-th ($p = 1, 2, ..., N_T$) transmitting and q-th ($q = 1, 2, ..., N_R$) receiving antenna elements are denoted by A_p^T and A_q^R, respectively. We assume that the signal is omnidirectionally
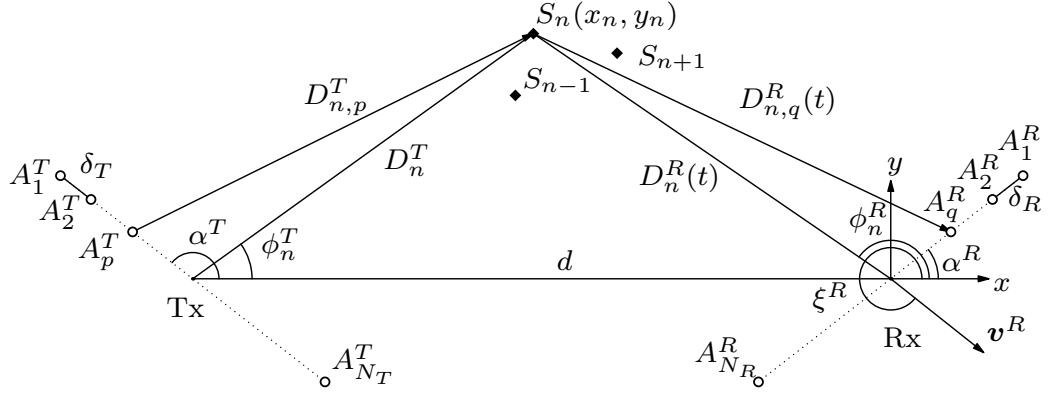
FIGURE 3.1: A 2D wideband massive MIMO channel model.

bounced only once by each scatterer, denoted by S_n ($n = 1, 2, ..., N_S$), and it travels a distance $D_{n,qp}(t) = D_{n,p}^T + D_{n,q}^R(t)$ from A_p^T to A_q^R via S_n at time instant t. The phase shifts θ_n introduced by the scatterers are modeled as i.i.d. random variables obeying a uniform distribution over $[0, 2\pi)$ [12]. The massive MIMO channel is represented by the matrix $\boldsymbol{H}(t, \tau) = [h_{qp}(t, \tau)]_{N_R \times N_T}$ whose (q, p) entry denotes the CIR between the antennas A_p^T and A_q^R. The CIR is given by

$$h_{qp}(t, \tau) = \sum_{n=1}^{N_S} c_n e^{j\psi_{n,qp}(t)} \delta(\tau - \tau_{n,qp}(t)) \tag{3.1}$$

where $j = \sqrt{-1}$, $\delta(\cdot)$ is the Dirac delta function. The term $\psi_{n,qp}(t) = k_0 D_{n,qp}(t) + \theta_n$ denotes the phase of the signal, $k_0 = 2\pi/\lambda$, and λ denotes the carrier wavelength. The n-th scattered signal is received with amplitude c_n and its associated propagation delay is $\tau_{n,qp}(t) = D_{n,qp}(t)/c_0$, where c_0 denotes the speed of light. Since signals from and to sufficiently separated antenna elements of the array experience different ToAs, $\tau_{n,qp}(t)$ in (3.1) depends on the antenna indices p and q. The channel transfer function (CTF), i.e., the Fourier transform of the CIR w.r.t. τ, is given by

$$H_{qp}(t, f) = \sum_{n=1}^{N_S} c_n e^{j\psi_{n,qp}(t)} e^{-j2\pi f \tau_{n,qp}(t)}. \tag{3.2}$$

For simplicity, we assume that the centre of the receiving array is located at the origin at $t = 0$ and it moves at a constant speed v^R forming an angle ξ^R w.r.t. the x-axis. The Tx is static and located at a distance d from the Rx along the negative x-axis.

Accordingly, the distance traveled by the signal radiated by A_p^T and received by A_q^R via S_n can be computed as

$$D_{n,qp}(t) = \sqrt{(x_n - x_q^R - v_x^R t)^2 + (y_n - y_q^R - v_y^R t)^2} + \sqrt{(x_n + d - x_q^T)^2 + (y_n - y_p^T)^2}$$

(3.3)

where (x_n, y_n) denote the Cartesian coordinates of S_n. The terms $x_q^R = \delta_q^R \cos(\alpha^R)$ and $y_q^R = \delta_q^R \sin(\alpha^R)$ with $\delta_q^R = (N_R - 2q + 1)\delta_R/2$ denote the Cartesian coordinates of the antenna A_q^R at $t = 0$. Similarly, $x_q^T = \delta_p^T \cos(\alpha^T)$ and $y_p^T = \delta_p^T \sin(\alpha^T)$ with $\delta_p^T = (N_T - 2p + 1)\delta_T/2$ are the projections of the position vector of A_p^T w.r.t. the centre of the transmitting array onto x and y axes, respectively. The Cartesian components of the velocity vector are $v_x^R = v^R \cos(\xi^R)$ and $v_y^R = v^R \sin(\xi^R)$.

Although the distance in (3.3) depends on the Cartesian coordinates (x_n, y_n), it is often convenient to describe the channel in terms of delays and angles, which is more suitable for channel characterization through measurements [108]. However, there are channel models, e.g., the One-Ring model, in which the scatterers' locations are described in other coordinates such as polar.

3.2.1 Spherical and plane wavefronts

Spherical wavefronts are considered in the model as long as (3.3) is used to compute the phase of the signal $\psi_{n,qp}(t)$ in (3.1). The conventional approximation for short periods of time and small arrays, i.e., the first-order or plane wavefront approximation, reduces the distance $D_{n,qp}(t)$ to

$$D_{n,qp}(t) \approx D_n - \delta_p^T \cos(\phi_n^T - \alpha^T) - \delta_q^R \cos(\phi_n^R - \alpha^R) - v^R t \cos(\phi_n^R - \xi^R) \qquad (3.4)$$

where $D_n = D_n^T + D_n^R(0) = \sqrt{(x_n + d)^2 + y_n^2} + \sqrt{x_n^2 + y_n^2}$ denotes the distance between the arrays' centres, and the terms ϕ_n^T and ϕ_n^R denote the AoD and AoA of the n-th scattered signal w.r.t. to the arrays' centres, which can be calculated as $\phi_n^R = \arctan(y_n/x_n)$ and $\phi_n^T = \arctan(y_n/(x_n + d))$.

In spatial WSS non-massive MIMO channel models, the plane-wavefront approximation in (3.4) is usually employed to compute the phase of the signal in (3.1) [12]. From (3.1) and (3.4), it can be seen that this approximation leads to linear space-time variations of the phase, which do not allow to capture the non-WSS properties of massive MIMO channels. In addition, the ToA $\tau_{n,qp}(t)$ in (3.1) and (3.2) is usually approximated as a constant value for every scatterer, i.e., $\tau_{n,qp}(t) = \tau_n$. We will show that this assumption may be inaccurate for large antenna arrays.

3.3   A Transformation Method of the STV joint-PDF of the ToA and AoA

In conventional WSS GBSMs [12], scatterers are assumed to be randomly distributed in the environment according to a predefined PDF that models the ToA and AoA of the received signal, and this PDF is space-time-frequency independent [108]. Unlike WSS channels, measurements [3], [5], [6], [16], [42]–[45], [66] have shown that ToAs and AoAs may change over the array and time for large arrays and periods of time, respectively. In addition, systems employing extremely large bandwidths, i.e., millimeter-wave systems, may be subject to frequency non-stationary effects that would need to be incorporated into the PDF of the ToA and AoA. However, we will assume that the PDF of ToA and AoA is frequency independent in this work.

In this section, we will introduce a method to obtain the STV joint PDF of ToA-AoA for every antenna pair A_p^T–A_q^R at any time instant t using the theory of transformation of random variables and the joint-PDF of ToA-AoA defined at the centre of both arrays and time instant $t = 0$. In addition, we will derive the transformation equations for the three most common ways of specifying the distribution of the scatterers, e.g., in the ToA-AoA [108], polar, and Cartesian domains. We will provide examples of application and derive the STV distributions of widely-used channel models such as the Ellipse, One-Ring, unified disk scattering model (UDSM), and Gaussian cluster models. These STV distributions will be used to compute the statistical properties of the channel in Section 3.5.

3.3.1 Transformation in ToA-AoA domain

As the direct transformation of the random ToA and AoA is rather complicated and leads to cumbersome expressions for the Jacobian determinant, we use a stepped transformation to obtain the STV joint PDF of ToA-AoA. For clarity, the most important elements of the transformation are illustrated in Figure 3.2 for a MIMO system employing 2×2 antennas at time instant $t = 0$. Note that we have depicted ULAs for convenience, but the proposed method is not constrained by any arrangement of the antenna arrays, i.e., it can be applied to arbitrary-shaped 2D arrays.

The origin of the Cartesian coordinate systems (X, Y) and (X_1, Y_1) are located at the centre of the receiving array and A_1^R, respectively. The AoAs of the signal scattered by S_n and measured at (X, Y) and (X_1, Y_1) are denoted by ϕ_n^R and $\phi_{1,n}^R$, respectively. Signals radiated from the centre of the transmitting array and bounced by the scatterers located in the ellipse ϵ, e.g., S_j and S_n, arrive at the centre of the receiving array with the same ToA, which is denoted as τ_n. Likewise, the ellipse ϵ_1 illustrates the same concept as ϵ when the signals transmitted from A_2^T and received at A_1^R experience a
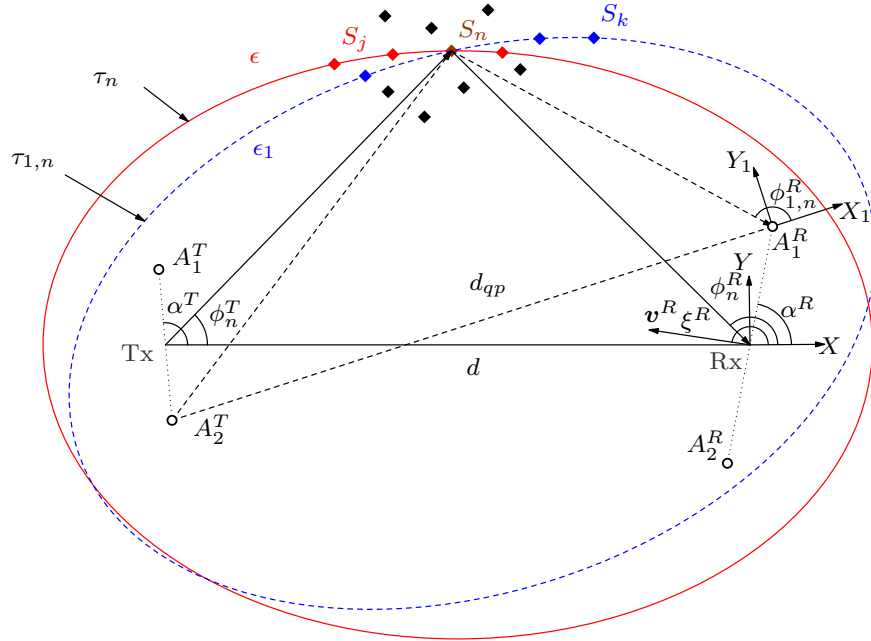
FIGURE 3.2: Elements of the transformation of the joint PDF of the ToA and AoA at $t = 0$.

constant delay denoted as $\tau_{1,n}$. The distribution of the ToA-AoA of a signal radiated from A_2^T and received at A_1^R can be obtained using the following method:

1. From a given distribution of ToA-AoA $f_{\tau,\phi^R}(\tau, \phi^R)$, the joint PDF of the location of the scatterers $f_{XY}(x, y)$ in the Cartesian coordinates (X, Y) is derived as proposed in [108]. The transformation of the random variables (τ, ϕ^R) is indeed a transformation of coordinates.

2. A second transformation is performed from (X, Y) into (X_1, Y_1), resulting in the PDF $f_{X_1 Y_1}(x_1, y_1; \delta_1^R, \delta_2^T, t)$. These coordinate systems are related by shift and rotation operations dependent of the positions of the antennas A_2^T and A_1^R.

3. The random variables determining the locations of the scatterers in the system (X_1, Y_1) are transformed back into the ToA-AoA domain, obtaining the joint PDF $f_{\tau_1, \phi_1^R}(\tau_1, \phi_1^R; \delta_1^R, \delta_2^T, t)$ for the antenna elements A_2^T and A_1^R.

The main advantage of this stepped approach compared to the direct one from (τ, ϕ^R) to (τ_1, ϕ_1^R) is that the transformation equations can be reused for other specifications of the scatterers' distribution in different domains, as it will be shown later. Also the resulting expressions for the Jacobian determinant of the transformations are less cumbersome than those of the direct transformation. Using the previous method, the joint PDF $f_{\tau_1, \phi_1^R}(\tau_1, \phi_1^R; \delta_q^R, \delta_p^T, t)$ can be obtained as (see Appendix A)

$$
\begin{aligned}
f_{\tau_1, \phi_1^R}(\tau_1, \phi_1^R; \delta_q^R, \delta_p^T, t) = & |J_1(x, y)|^{-1} |J_3(\tau_1, \phi_1^R)|^{-1} \\
& \times f_{\tau,\phi^R}\left(c_0^{-1}(\sqrt{x^2 + y^2} + \sqrt{(x+d)^2 + y^2}), \arctan(y/x)\right)
\end{aligned}
$$

(3.5)

with

$$
x = \frac{1}{2}\left(\frac{(c_0 \tau_1)^2 - d_{qp}^2(t)}{c_0 \tau_1 + d_{qp}(t) \cos \phi_1^R}\right) \cos(\phi_1^R + \alpha_{qp}(t)) + x_q^R + v_x^R t \tag{3.6}
$$

$$
y = \frac{1}{2}\left(\frac{(c_0 \tau_1)^2 - d_{qp}^2(t)}{c_0 \tau_1 + d_{qp}(t) \cos \phi_1^R}\right) \sin(\phi_1^R + \alpha_{qp}(t)) + y_q^R + v_y^R t \tag{3.7}
$$

and the Jacobian determinants $J_1(x, y)$ and $J_3(\tau_1, \phi_1^R)$ can be found in Appendix A. Notice that the actual AoA measured from A_q^R is not ϕ_1^R but $\phi_1^R - \alpha_{qp}(t)$ due to

the rotation of the coordinate system (X_1, Y_1) w.r.t. (X, Y). It can be seen that for small arrays and periods of time, i.e., $\delta_{N_T}^T \ll (c_0\tau - d)$, $\delta_{N_R}^R \ll (c_0\tau - d)$, and $v^R t \ll (c_0\tau - d)$, then $|J_1(x, y)|^{-1}|J_3(\tau_1, \phi_1^R)|^{-1} \approx 1$, $\alpha_{qp}(t) \approx 0$, $d_{qp}(t) \approx d$, and $f_{\tau_1, \phi_1^R}(\tau_1, \phi_1^R; \delta_q^R, \delta_p^T, t) \approx f_{\tau, \phi^R}(\tau, \phi^R)$. In such conditions, the joint PDF of ToA-AoA is independent of the antenna element and time instant. Hence, the channel can be considered as WSS.

It is important to highlight the difference between the transformation method proposed and the ones used in previous theoretical works (e.g., [104]–[106] and [13], [88], [89]). In the proposed method, the parameters that define $f_{\tau, \phi^R}(\tau, \phi^R)$ are space-time invariant, but this distribution gets transformed for different antenna elements of the arrays and time instants. In those previous works, it was assumed that only some parameters, e.g., the mean AoA, defining the distribution are STV, but the distribution remained space-time invariant. The previous approach is an approximation that may only hold in some limited cases as we will show in subsequent sections.

3.3.1.1 Ellipse narrowband and wideband channel models

In the Ellipse channel model, the scatterers are located in the perimeter of an ellipse with foci at the center of the transmitting and receiving arrays. In the single-ellipse model, the ToA is fixed to a single value τ_0, but the AoA distribution is not defined. Here, we will employ the widely-used von Mises distribution to model the AoA as an example, as it can cover both isotropic and non-isotropic angular distributions through its parameters [12], [111]. The joint PDF is given by

$$f_{\tau, \phi^R}(\tau, \phi^R) = \delta(\tau - \tau_0) \cdot \frac{1}{2\pi I_0(\kappa)} e^{\kappa \cos(\phi^R - \mu^\phi)} \tag{3.8}$$

where μ^ϕ and κ are the mean AoA and concentration parameter, respectively, and $I_0(\cdot)$ denotes the zero-order modified Bessel function of the first kind. It is important to remark that (3.8) implies independent time dispersion and frequency dispersion [12], i.e., its joint PDF of ToA-AoA is separable, and is also a narrowband channel model, i.e., the absolute value of the FCF is constant. A more flexible distribution of the

scatterers that includes the previous one as a special case and permits to capture wideband characteristics of the channel is

$$f_{\tau,\phi^R}(\tau,\phi^R) = \frac{1}{\sigma^\tau}e^{-\frac{(\tau-\tau_0)}{\sigma^\tau}} \cdot u(\tau-\tau_0) \cdot \frac{1}{2\pi I_0(\kappa)}e^{\kappa\cos(\phi^R-\mu^\phi)} \tag{3.9}$$

where $u(\cdot)$ denotes the unit-step function, i.e., $u(x) = 1$ for $x > 0$ and zero otherwise. Note that the marginal distribution of delays $\delta(\tau-\tau_0)$ in (3.8) has been substituted in (3.9) by a shifted exponential distribution with minimum delay τ_0 and standard deviation σ^τ, which denotes the delay spread of the channel. The unit-step function is used to guarantee that the model is causal. It is clear that as $\sigma^\tau \to 0$, the PDF in (3.9) converges to that in (3.8). From the communications system's perspective, as long as σ^τ is much smaller than the time-resolution of the system considered, both distributions model equivalent channels. The transformed PDFs at the antennas A_p^T, A_q^R and time instant t can be obtained by plugging (3.8) and (3.9) into (3.5). As it will be shown in the results presented in Section 3.5, the transformation of (3.8) breaks down the separability of the distribution of ToA-AoA, introducing a dependence between these two random variables. This can be easily seen by noting that the term $\delta(\tau-\tau_0)$ in (3.8) is transformed into $\delta(c_0^{-1}[\sqrt{x^2+y^2}+\sqrt{(x+d)^2+y^2}]-\tau_0)$, with x and y given by (3.6) and (3.7), respectively. As the values of ϕ_1^R that solve $\sqrt{x^2+y^2}+\sqrt{(x+d)^2+y^2} = c_0\tau_0$ depend on the the delay τ_1, the ToA and AoA are dependent and therefore correlated. As this argument can be applied to any separable distribution, the important *independent time dispersive and Doppler frequency dispersive* property [12] of the Ellipse and other channel models is broken down by the large dimensions of the array.

3.3.2 Transformation in polar domain

Analogous to the previous section, the PDF of the position of the scatterers is transformed in three steps. However, as the given PDF is defined in polar coordinates, i.e., $f_{R,\phi^R}(r,\phi^R)$, the first transformation into the coordinates (X,Y) is performed using $X = R\cos(\phi^R)$ and $Y = R\sin(\phi^R)$. Applying the theory of transformation of random

variables, the joint PDF of (X, Y) is given by

$$f_{X,Y}(x,y) = |J_1(x,y)|^{-1} f_{R,\phi^R}\left(\sqrt{x^2 + y^2}, \arctan(y/x)\right) \tag{3.10}$$

where $J_1(x,y)$ is the Jacobian of the transformation, i.e.,

$$|J_1(x,y)|^{-1} = \left| \frac{1}{\sqrt{x^2 + y^2}} \right|. \tag{3.11}$$

Finally, the joint PDF $f_{\tau_1,\phi_1^R}(\tau_1, \phi_1^R; \delta_q^R, \delta_p^T, t)$ can be obtained as

$$f_{\tau_1,\phi_1^R}(\tau_1, \phi_1^R; \delta_q^R, \delta_p^T, t) = |J_1(x,y)|^{-1}|J_3(\tau_1, \phi_1^R)|^{-1} f_{R,\phi^R}\left(\sqrt{x^2 + y^2}, \arctan(y/x)\right) \tag{3.12}$$

where $|J_3(\tau_1, \phi_1^R)|^{-1}$, x, and y are defined in (A.14), (3.6), and (3.7), respectively.

3.3.2.1   One-ring model and unified disk scattering model

The one-ring model defines the geometrical configuration of the scatterers in a circular ring around the center of the receiving array. This geometry is usually applied to model narrowband channels, although its delay spread is not zero and varies according to the radius of the ring and the distribution of the AoA [112]. Using the von Mises distribution for the AoA, the PDF of the position of the scatterers in polar coordinates is given by

$$f_{R,\phi^R}(r, \phi^R) = \delta(r - r_0) \cdot \frac{1}{2\pi I_0(\kappa)} e^{\kappa \cos(\phi^R - \mu^\phi)} \tag{3.13}$$

where r_0 is the radius of the ring. A more flexible distribution that includes the one-ring model as a special case is the UDSM [113]. Although the UDSM is constrained to uniform distributions of the AoA, the PDF of the position of the scatterers can be extended to account for other distributions as

$$f_{r,\phi^R}(r, \phi^R) = \frac{(k_U + 1)}{r_0^{(k_U+1)}} r^{k_U} \cdot \left[u(r) - u(r - r_0) \right] \cdot \frac{1}{2\pi I_0(\kappa)} e^{\kappa \cos(\phi^R - \mu^\phi)} \tag{3.14}$$

where $k_U > -1$ is a real-valued parameter called the shape factor that controls the spread of the scatterers w.r.t. the radial distance. As $k_U \to \infty$, the scatterers become more concentrated near the edge of the disk forming a ring of radius r_0 and (3.14) converges to (3.13). The transformed PDFs at the antennas A_p^T, A_q^R and time instant t can be obtained by plugging (3.13) and (3.14) into (3.12). The resulting PDFs are omitted here for brevity.

3.3.3   Transformation in Cartesian domain

In this case, the transformation procedure is reduced to two steps as it is not necessary to perform a transformation to cartesian coordinates. Thus, the joint PDF $f_{\tau_1,\phi_1^R}(\tau_1, \phi_1^R; \delta_q^R, \delta_p^T, t)$ is a function of the joint PDF $f_{X,Y}(x, y)$ and can be obtained as

$$f_{\tau_1,\phi_1^R}(\tau_1, \phi_1^R; \delta_q^R, \delta_p^T, t) = \left| J_3(\tau_1, \phi_1^R) \right|^{-1} f_{X,Y}(x, y) \qquad (3.15)$$

where x and y are defined in (3.6) and (3.7), respectively.

3.3.3.1   Gaussian cluster channel model

The Gaussian cluster model has widely been used in multiple standard GBSMs, e.g., COST 207 [81] and COST 2100 [82], to model single- and multi-bounce clustered MPCs including intra-cluster delay and angle spreads. A simplified PDF of the position of the scatterers for this model in Cartesian coordinates is given by

$$f_{X,Y}(x, y) = \frac{1}{2\pi(\sigma^{xy})^2} e^{\frac{-1}{2(\sigma^{xy})^2}[(x-x_0)^2 + (y-y_0)^2]} \qquad (3.16)$$

where (x_0, y_0) denote the coordinates of the center of the cluster and σ^{xy} the spread of the cluster in the xy-plane. The spreads of the cluster in the x and y axes are assumed to be equal here for simplicity. The joint PDF $f_{\tau_1,\phi_1^R}(\tau_1, \phi_1^R; \delta_q^R, \delta_p^T, t)$ can be obtained by plugging (3.16) into (3.15). The resulting PDF is omitted here for brevity.

3.4 Statistical Properties of the Channel

In the following, the STV PDF $f_{\tau_1,\phi_1^R}(\tau_1,\phi_1^R;\delta_q^R,\delta_p^T,t)$ obtained in Section 3.3 will be used to compute the Doppler, delay, and angular PSDs, and the spatial-temporal-frequency cross-correlation function (STF-CCF).

3.4.1 Computation of statistical properties from the transformed distribution of the ToA-AoA

3.4.1.1 Delay power spectral density (PSD)

The delay PSD or PDP measures the distribution of the received power in the delay domain. In addition, the PDP is proportional to the distribution of the ToA of the received signal [12, p. 348]. Accordingly, the STV PDP can be obtained through the marginal PDF of τ_1 as $S_{\tau_1}(\tau_1,\delta_q^R,\delta_p^T,t) = \sigma_0^2 f_{\tau_1}(\tau_1,\delta_q^R,\delta_p^T,t)$ where σ_0^2 denotes the total received power and $f_{\tau_1}(\tau_1,\delta_q^R,\delta_p^T,t)$ denotes the marginal PDF of the ToA.

3.4.1.2 Angular power spectral density (PSD)

Similarly, the angular PSD or power angular spectrum (PAS) is a measure of the incoming power in the angular domain. Thus, the STV PAS can be analogously obtained through the marginal PDF of the AoA ϕ_1^R as $S_{\phi_1^R}(\phi_1^R,\delta_q^R,\delta_p^T,t) = \sigma_0^2 f_{\phi_1^R}(\phi_1^R,\delta_q^R,\delta_p^T,t)$ where $f_{\phi_1^R}(\phi_1^R,\delta_q^R,\delta_p^T,t)$ denotes the marginal PDF of the AoA.

3.4.1.3 Doppler power spectral density (PSD)

For a mobile station moving at a constant speed v^R and direction defined by the angle ξ^R, the Doppler frequency ν is a function of the AoA as $\nu = \nu_{\max}\cos(\phi_1^R - \xi^R)$, where $\nu_{\max} = v^R/\lambda$ denotes the maximum Doppler frequency. According to this definition,

it can be proved that the Doppler PSD is given by [12]

$$S_\nu(\nu, \delta_q^R, \delta_p^T, t) = \frac{2\sigma_0}{\nu_{\max}\sqrt{1 - (\nu/\nu_{\max})^2}} \cdot g_{\phi_1^R}(\arccos[\nu/\nu_{\max}]; \delta_q^R, \delta_p^T, t) \qquad (3.17)$$

where

$$g_{\phi_1^R}(\phi_1^R; \delta_q^R, \delta_p^T, t) = \frac{1}{2}\left(f_{\phi_1^R}(\phi_1^R, \delta_q^R, \delta_p^T, t) + f_{\phi_1^R}(-\phi_1^R, \delta_q^R, \delta_p^T, t)\right) \qquad (3.18)$$

is the even part of the STV PDF of the AoA.

3.4.1.4 Space-time-frequency cross-correlation function

In the proposed approach, the cross-correlation between the signal corresponding to the link A_p^T–A_q^R at time instant t and frequency f, and that of the link $A_{p'}^T$–$A_{q'}^R$ at time $t + \Delta t$ and frequency $f + \Delta f$ can be obtained as $\rho_{qp,q'p'}(t, \Delta t, \Delta f) = \mathbb{E}[H_{qp}(t,f)H_{q'p'}^*(t + \Delta t, f + \Delta f)]$, with $\mathbb{E}(\cdot)$ denoting the expectation operator and H^* the complex conjugate of H. Thus, the STF-CCF can be computed as

$$\rho_{qp,q'p'}(t, \Delta t, \Delta f) = \sigma_0^2 \int_0^\infty \int_0^{2\pi} e^{-jk_0\Psi_{qp}^{q'p'}(t,\Delta t)} e^{-j2\pi\Delta f\tau_1} f_{\tau_1,\phi_1^R}(\tau_1, \phi_1^R; \delta_q^R, \delta_p^T, t)\mathrm{d}\tau_1\mathrm{d}\phi_1^R$$

$$(3.19)$$

where $\Psi_{qp}^{q'p'}(t, \Delta t) = \Delta_{pp'}\cos(\phi_1^T - \alpha^T + \alpha_{qp}(t)) + \Delta_{qq'}\cos(\phi_1^R - \alpha^R + \alpha_{qp}(t)) + v^R\Delta t\cos(\phi_1^R - \xi^R + \alpha_{qp}(t))$ denotes the phase difference between the signal transmitted from A_p^T and received by A_q^R at time t and the signal transmitted from $A_{p'}^T$ and received by $A_{q'}^R$ at $t + \Delta t$. The distance between A_p^T and $A_{p'}^T$ is $\Delta_{pp'} = (p - p')\delta_T$, and that between A_q^R and $A_{q'}^R$ is $\Delta_{qq'} = (q - q')\delta_R$.

Although the STF-CCF in (3.19) approximates the correlation between two signals separated in time by Δt and transmitted (received) by antennas separated by $\Delta_{pp'}$ ($\Delta_{qq'}$), the joint PDF of the ToA-AoA $f_{\tau_1,\phi_1^R}(\tau_1, \phi_1^R; \delta_q^R, \delta_p^T, t)$ is defined for two specific antennas A_p^T and A_q^R, and a single time instant t. This indicates that (3.19) remains valid for a space-time region around the antennas A_p^T and A_q^R, and time instant t where $f_{\tau_1,\phi_1^R}(\tau_1, \phi_1^R; \delta_q^R, \delta_p^T, t)$ is approximately space-time invariant. The short-term

invariance of this PDF can be justified by noting that the coherence region of most channels, i.e., the region where the STF-CCF is above certain threshold, is usually much smaller than the region where the channel can be considered WSS. This also justifies the use of the plane wavefront approximation in (3.4) to obtain (3.19).

When the spherical wavefront is used, the STF-CCF can be calculated as [88]

$$\hat{\rho}_{qp,q'p'}(t,\Delta t,\Delta f) = \sigma_0^2 \int_0^\infty \int_0^{2\pi} e^{-jk_0 \hat{\Psi}_{qp}^{q'p'}(t,\Delta t)} e^{-j2\pi \Delta f \tau} f_{\tau,\phi^R}(\tau,\phi^R) \mathrm{d}\tau \mathrm{d}\phi^R \qquad (3.20)$$

where $\hat{\Psi}_{qp}^{q'p'}(t,\Delta t) = D_{qp}(t) - D_{q'p'}(t+\Delta t)$ and $D_{qp}(t)$ denotes the total distance traveled by the signal from A_p^T to A_q^R at time instant t as given by (3.3). Notice that the ToA and AoA used in (3.20) are defined at the center of the transmitting and receiving arrays at time $t = 0$ and they are space-time invariant. Consequently, the spherical wavefront is required to capture non-WSS properties of the channel and the plane wavefront approximation in (3.4) cannot be used.

With respect to the deterministic simulation model as defined in (3.1) and (3.2) once the random variables involved are drawn, the STF-CCF can be computed as a local time-average, i.e.,

$$\tilde{\rho}_{qp,q'p'}(t,\Delta t,\Delta f) \approx \frac{1}{T} \int_{t-T/2}^{t+T/2} H_{qp}(t',f) H_{q'p'}^*(t'+\Delta t, f+\Delta f) \mathrm{d}t'. \qquad (3.21)$$

The temporal ACFs can be obtained by setting $\Delta f = \Delta_{qq'} = \Delta_{pp'} = 0$ in (3.19), (3.20), and (3.21) as $\rho_{qp,qp}(t,\Delta t,0)$, $\hat{\rho}_{qp,qp}(t,\Delta t,0)$, and $\tilde{\rho}_{qp,qp}(t,\Delta t,0)$, respectively. By setting $\Delta t = \Delta f = 0$ in the same equations, we can calculate the S-CCFs as $\rho_{qp,q'p'}(t,0,0)$, $\hat{\rho}_{qp,q'p'}(t,0,0)$, and $\tilde{\rho}_{qp,q'p'}(t,0,0)$. The FCFs are computed by setting $\Delta_{qq'} = \Delta_{pp'} = \Delta t = 0$ as $\rho_{qp,qp}(t,0,\Delta f)$, $\hat{\rho}_{qp,qp}(t,0,\Delta f)$, and $\tilde{\rho}_{qp,qp}(t,0,\Delta f)$. The ACFs, S-CCFs, and FCFs obtained depend on the antenna indices and the time instant through the joint PDF $f_{\tau_1,\phi_1^R}(\tau_1,\phi_1^R;\delta_q^R,\delta_p^T,t)$ in (3.19) and through the total distance in $\hat{\Psi}_{qp}^{q'p'}(t,\Delta t)$ in (3.20), indicating that the channel is space-time non-WSS.

3.4.2   Approximate solutions to the ACF and Doppler PSD

Although analytic solutions for the STF-CCF in (3.19) are difficult to obtain due to the complexity of the STV joint-PDF of the ToA and AoA, approximate expressions for the ACF, Doppler PSD, and S-CCF can be derived for non-WSS massive MIMO channels. We propose a simplified approach based on an implicit assumption of previous works, e.g., [103] and [104], in which the PAS was assumed space-time invariant, but some of its parameters were not.

Let us consider that the AoA defined at the center of the array (ϕ^R) follows a von Mises distribution with parameters (κ, μ^ϕ). If we assume that only the parameters of this distribution are STV, the PDF of the AoA for any A_p^T, A_q^R and time instant t is

$$f_{\phi_1^R}(\phi_1^R; \delta_p^T, \delta_q^R, t) = \frac{1}{2\pi I_0(\kappa_{qp}(t))} e^{\kappa_{qp}(t) \cos(\phi_1^R - \mu_{qp}^\phi(t))} \qquad (3.22)$$

where the mean AoA $\mu_{qp}^\phi(t)$ and concentration parameter $\kappa_{qp}(t)$ are now dependent of time and antenna indices. In slowly varying channels, we can assume that the rates of change of $\mu_{qp}^\phi(t)$ and $\kappa_{qp}(t)$ are small. If the spatial-temporal evolution of these parameters is known, the STV ACF can be approximated as [12]

$$\rho(\Delta_t; \delta_p^T, \delta_q^R, t) \approx \frac{2\sigma_0^2}{I_0(\kappa_{qp}(t))}$$
$$\times I_0\left(\sqrt{\kappa_{qp}^2(t) - (2\pi\nu_{\max}\Delta t)^2 - j4\pi\kappa_{qp}(t)\nu_{\max}\Delta t \cos(\mu_{qp}^\phi(t) - \xi^R))}\right).$$
$$(3.23)$$

As the parameters $\mu_{qp}^\phi(t)$ and $\kappa_{qp}(t)$ depend on the position over the array and time instant, the channel is non-WSS in these domains. Similarly, according to (3.17), the STV Doppler PSD is

$$S_\nu(\nu, \delta_q^R, \delta_p^T, t) \approx \frac{2\sigma_0^2 \, e^{\kappa_{qp}^2(t)\cos(\mu_{qp}^\phi(t) - \xi^R)\nu/\nu_{\max}}}{\pi\nu_{\max} I_0(\kappa_{qp}^2(t))\sqrt{1 - (\nu/\nu_{\max})^2}}$$
$$\times \cosh\left(\kappa_{qp}^2(t)\sin(\mu_{qp}^\phi(t) - \xi^R)\sqrt{1 - \left(\frac{\nu}{\nu_{\max}}\right)^2}\right). \qquad (3.24)$$

56

In Appendix B, we derive approximate solutions of the STV concentration $\kappa_{qp}(t)$ and mean AoA $\mu_{qp}^{\phi}(t)$ as

$$
\kappa_{qp}(t) = \kappa \left(1 + \left(\frac{\delta_q^R}{r_c} \right)^2 + \left(\frac{v^R t}{r_c} \right)^2 - 2 \frac{\delta_q^R}{r_c} \cos(\mu_c^{\phi} - \alpha^R) \right.
$$
$$
\left. - 2 \frac{v^R t}{r_c} \cos(\mu_c^{\phi} - \xi^R) + 2 \frac{v^R t \delta_q^R}{r_c^2} \cos(\alpha^R - \xi^R) \right)
\tag{3.25}
$$

and

$$
\mu_{qp}^{\phi}(t) = \arctan \left(\frac{r_c \sin(\mu_c^{\phi}) - \delta_q^R \sin(\alpha^R) - v^R t \sin(\xi^R)}{r_c \cos(\mu_c^{\phi}) - \delta_q^R \cos(\alpha^R) - v^R t \cos(\xi^R)} \right),
\tag{3.26}
$$

respectively. It can be easily seen that, for small arrays and short periods of time, i.e., $N_R \delta_R / 2 \ll r_c$ and $v^R t \ll r_c$, the concentration parameter and mean AoA become invariant, i.e., $\kappa_{c,q}(t) \approx \kappa_c$ and $\mu_{qp}^{\phi}(t) \approx \mu_c^{\phi}$.

3.5   Results and Analysis

In this section, the array-varying distribution of channel parameters and statistical properties obtained using the proposed transformation method, approximation method, spherical wavefront approach, and simulation results, for three channel models introduced in Section 3.3 are presented and compared. The results corresponding to the transformation method were obtained by numerical evaluation of (3.5), (3.12), and (3.15). Similarly, those corresponding to the approximation method were computed by evaluating (3.23)–(3.24) and making use of the variant parameters as determined by (3.25) and (3.26). We evaluated (3.20) to obtain the results corresponding to the spherical wavefront approach. For the simulation results, we generated 10^3 scatterers randomly distributed and computed the CIR as in (3.2). Realizations of the channel parameters, e.g., ToA and AoA, were obtained by the inverse transform sampling method [114]. In this method, samples of a uniformly distributed random variable are transformed by the inverse of the aimed cumulative distribution function (CDF), e.g., the AoAs were generated as $\phi^R = F_{\phi^R}^{-1}(U)$ where U denotes a random variable uniformly distributed over the interval $[0, 1)$ and $F_{\phi^R}^{-1}(\cdot)$ denotes the inverse of

the aimed CDF of the AoA. To obtain the simulation results, the statistical properties were computed by averaging 10^3 realizations of the STF-CCF in (3.21).

In the following, we assume that no line-of-sight path exists between the Tx and Rx, which are located 100 m apart along the x-axis at $t = 0$ and both count on ULAs composed of 100 antenna elements each. The separation between adjacent antennas is $\lambda/2$ at 2 GHz of carrier frequency. Other parameters used may be different and they will be specified for every result.

3.5.1 Array-variant ToA-AoA joint-PDF

In Figure 3.3, we present the STV joint-PDFs of the ToA-AoA in logarithmic scale (dB) of the wideband Ellipse model at the extremes and center of the receiving array, i.e., at A_1^R (left), A_{50}^R (center), and A_{100}^R (right). We imposed a minimum ToA of $\tau_0 = 400$ ns and a concentration parameter $k = 0$, i.e., uniform AoA. On one hand, the joint PDF of the ToA-AoA at A_{50}^R (center) shows the properties imposed by the channel model such as uniformity in the AoA domain, exponential decay in the ToA domain, and independence between ToA and AoA. On the other hand, the PDFs at the extremes of the array are remarkably affected by the transformation. The resulting meandering shape of the PDFs at A_1^R and A_{100}^R shows that the ToA varies as a function of the AoA. This is most noticeable when the receiving antenna is farthest
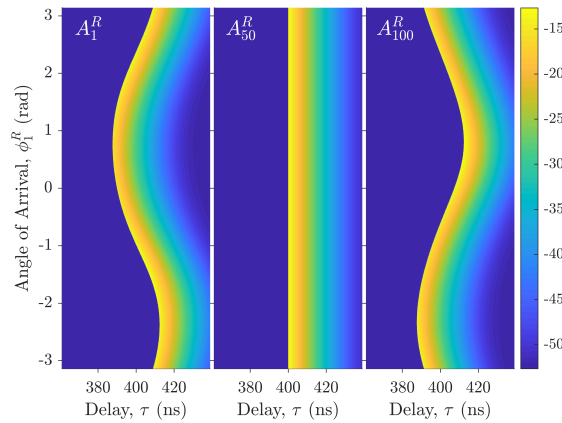
FIGURE 3.3: Joint-PDF of the ToA and AoA at A_1^R (left), A_{50}^R (center), and A_{100}^R (right), for the wideband Ellipse channel model in (3.9) ($d = 100$ m, $f_c = 2$ GHz, $\tau_0 = 400$ ns, $\sigma^\tau = 2$ ns, $\mu^\phi = \pi/5$, $\kappa = 0$, $N_R = 100$, $\delta_R = \lambda/2$, $\alpha^R = \pi/4$, $t = 0$ s).

from the focus of the ellipse, i.e., at A_1^R and A_{100}^R, as the sum of the distances from the opposite focus (Tx) to such antennas via scatterers of the ellipse is highly variant. In the AoA domain, the uniformity imposed ($\kappa = 0$) at the center of the array is no longer valid at its ends. Two maxima of the PDF appear around $\phi_1^R \approx -\pi/2$ and $\phi_1^R \approx \pi/4$ for A_1^R and A_{100}^R, respectively, indicating a reduction of the angular spread.

In Figure 3.4, an analogous comparison with a different value of the concentration parameter ($\kappa = 10$) is shown. In the AoA domain, whereas the PDF at A_1^R is stretched and the maximum is slightly shifted toward lower values, the PDF at A_{100}^R becomes more concentrated and shifted toward higher values, resulting in higher and lower values of the angular spread, respectively.

Similarly, in the delay domain, the distributions at A_1^R and A_{100}^R are shifted toward lower and higher values, respectively, but the variations of the ToA are relatively small. We have observed that the angular spread increases and the mean ToA decreases at one end of the array and vice versa at the other end. These results can be easily explained by noting that A_1^R and A_{100}^R are closer to the ellipse of scatterers than A_{50}^R.

The results presented show that, at the extremes of a large-scale array, additional delay spread may be introduced into the channel model with unforeseen consequences. This artifact of the Ellipse channel model produced by the large dimensions of the array was not considered in previous works, e.g., [13], [88], [89], [115], [116]. Moreover,
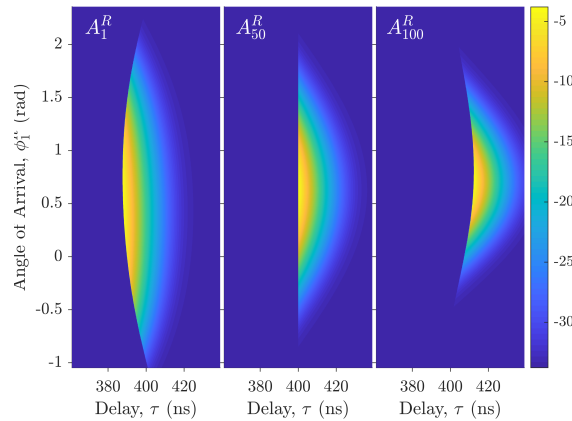
FIGURE 3.4: Joint-PDF of the ToA and AoA at A_1^R (left), A_{50}^R (center), and A_{100}^R (right), for the wideband Ellipse channel model in (3.9) ($d = 100$ m, $f_c = 2$ GHz, $\tau_0 = 400$ ns, $\sigma^\tau = 2$ ns, $\mu^\phi = \pi/5$, $\kappa = 10$, $N_R = 100$, $\delta_R = \lambda/2$, $\alpha^R = \pi/4$, $t = 0$ s).

both Figures 3.3 and 3.4 indicate that the transformation performed breaks down the separability of the joint PDF of the ToA and AoA, as the conditional distribution of the AoA given a specific ToA depends on the delay considered.

As the STV statistical properties of the channel are noticeable only when the scatterers are relatively close to any of the arrays, we will use the parameters of the channel models presented in Table 3.1 in the following unless otherwise stated. In this case, the scatterers are clustered 11 m away from the centre of the receiving array, with mean AoA of 36 degrees and angular spread of 18.6 degrees approximately ($\kappa = 10$). The parameters of the Ellipse, modified UDSM, and Gaussian cluster models are selected so that the maximum concentrations of the scatterers of all three models are coincident. Thus, by setting μ^ϕ and σ^{ϕ^R}, the remaining parameters are $\mu^x = \mu^r \cos(\mu^\phi)$ and $\mu^y = \mu^r \cos(\mu^\phi)$, with

$$\mu^r = \frac{1}{2} \frac{(c_0\mu^\tau)^2 - d^2}{c_0\mu^\tau + d\cos(\mu^\phi)}. \tag{3.27}$$

The parameters σ^x and σ^y can be obtained according to the relationship $\sigma^x = \sigma^y = \mu^r/\sqrt{\kappa}$ established in Section 3.4.2. The delay spread of the Ellipse model σ^τ and distance spread of the UDSM model σ^r can be chosen arbitrarily small.

3.5.2 Delay and angular power spectral densities (PSDs)

In Figures 3.5 and 3.6 we present these two marginal distributions at both extremes of the array, i.e., at A_1^R and A_{100}^R. Along with the drift of the marginal PDFs, variations of the angular and delay spreads over the array can be observed. Specifically, the mean AoA drifts approximately 0.13 rad ($\approx$ 7 degrees) and the angular spread is approximately 12 degrees higher at A_1^R than that at A_{100}^R. As it was stated above, the

TABLE 3.1: Parameters of the PDF of the three channel models.

Ellipse				UDSM				Gaussian			
ϕ^R (deg)		τ (ns)		ϕ^R (deg)		r (m)		X (m)		Y (m)	
μ^ϕ	σ^{ϕ^R}	μ^τ	σ^τ	μ^ϕ	σ^{ϕ^R}	μ^r	σ^r	μ^x	σ^x	μ^y	σ^y
36.0	18.6	400	1	36.0	18.6	11	1	8.9	3.5	6.4	3.5

angular spread at A_1^R is higher because this antenna is closer to the maximum of the scattering region than A_{100}^R and it is well known that the angular size of a region is inversely proportional to the distance to it.

As the marginal PDFs of the AoA are the same for the three models (von Mises), their variations over the array result in almost identical distributions. Note that this is consistent with the approximations used in (3.25) and (3.26) to obtain the STV parameters of the AoA distribution. Although each model presents a different
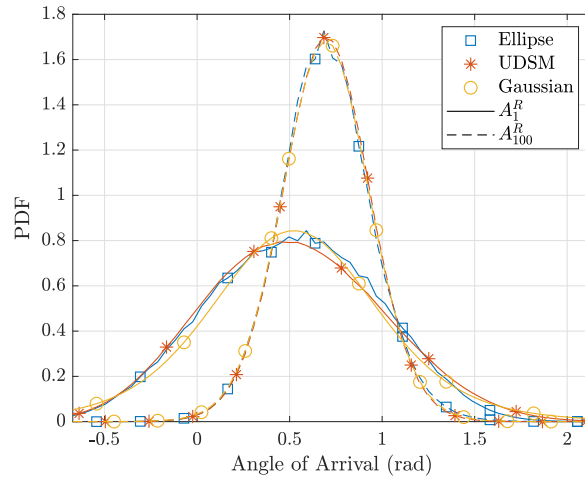
FIGURE 3.5: Comparison of the PDF of the AoA at the two extremes of the array for the Ellipse, modified UDSM, and Gaussian cluster channel models ($d = 100$ m, $f_c = 2$ GHz, $\tau_0 = 400$ ns, $r_0 \approx 11$ m, $\sigma^\tau = 3.4$ ns, $k_U = 10$, $\sigma^{xy} \approx 3.5$ m^{-1} $\mu^\phi = \pi/5$, $\kappa = 10$, $N_R = 100$, $\delta_R = \lambda/2$, $\alpha^R = \pi/4$, $t = 0$ s).
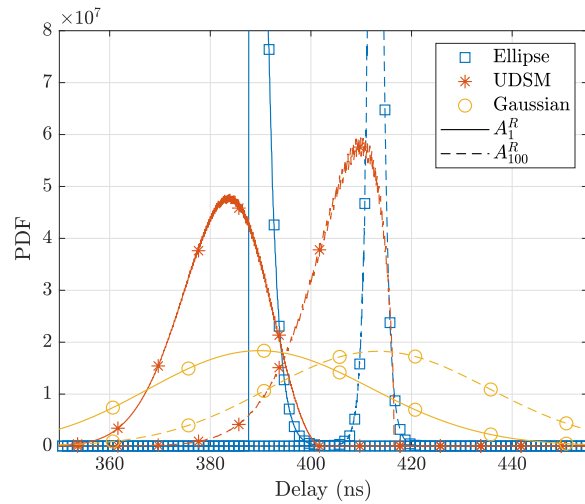
FIGURE 3.6: Comparison of the PDF of the ToA at the two extremes of the array for the Ellipse, modified UDSM, and Gaussian cluster channel models ($d = 100$ m, $f_c = 2$ GHz, $\tau_0 = 400$ ns, $r_0 \approx 11$ m, $\sigma^\tau = 3.4$ ns, $k_U = 10$, $\sigma^{xy} \approx 3.5$ m^{-1} $\mu^\phi = \pi/5$, $\kappa = 10$, $N_R = 100$, $\delta_R = \lambda/2$, $\alpha^R = \pi/4$, $t = 0$ s).

TABLE 3.2: Mean and spread values of the AoA and ToA at three antenna elements of the receive ULA.

	Ellipse				UDSM				Gaussian			
	Angle (deg)		Delay (ns)		Angle (deg)		Delay (ns)		Angle (deg)		Delay (ns)	
	μ	σ	μ	σ	μ	σ	μ	σ	μ	σ	μ	σ
A_1^R	31.2	26.4	389.7	1.8	31.4	28.0	382.1	8.2	30.9	32.2	390.6	21.2
A_{50}^R	36.0	18.6	400.8	1.0	36.0	18.6	392.4	7.8	35.9	19.2	401.5	21.6
A_{100}^R	38.5	14.3	413.0	1.3	38.3	13.8	404.5	7.7	38.3	14.1	413.7	21.8

marginal PDF of the ToA, a similar drift of approximately 23 ns of the mean ToA and small variations of the delay spread (below 1 ns) can be observed in Figure 3.6 for the three models. For the reader's convenience, Table 3.2 summarizes the mean values and spreads of both marginal distributions at the two extremes of the receiving array for the three models. For comparison purposes, the same parameters are provided for one of the two innermost receiving antennas (A_{50}^R), i.e., approximately at the centre of the receiving array.

As we will show, the differences between joint PDFs of the AoA and ToA at different positions of the array will result in STV statistical properties of the channel such as the ACF, S-CCF, Doppler PSD, and FCF.

3.5.3 Temporal autocorrelation function (ACF)

In Figure 3.7, we present a comparison of the absolute values of the array-variant local ACFs obtained by the transformation method, approximation method, spherical wavefront approach, and simulation, at the two extremes of the receiving ULA and for different directions of motion ξ^R. Although there are small differences between the results corresponding to each method, the ACFs obtained through the transformation and approximation methods are very similar in the whole range. Moreover, the good agreement between the methods proposed and the spherical wavefront approach indicates that all these methods are approximately equivalent.

Note that only the ACF of the Ellipse model is presented in Figure 3.7. This is because in equal conditions of motion, i.e., v^R and ξ^R are equal for the three models,
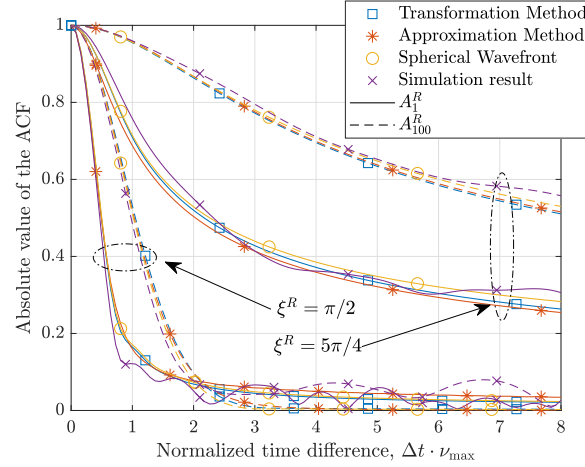
FIGURE 3.7: Comparison of the absolute values of the local ACF obtained by the transformation method, approximation method, spherical wavefront approach, and simulation at the two extremes of the receiving array ($d = 100$ m, $f_c = 2$ GHz, $\tau_0 = 400$ ns, $\sigma^\tau = 3.4$ ns, $\mu^\phi = \pi/5$, $\kappa = 10$, $N_R = 100$, $\delta_R = \lambda/2$, $\alpha^R = \pi/4$, $\nu_{\max} = 90$ Hz, $v^R = 13.5$ m/s, $\delta_T = 0$ m, $t = 0$).

the ACF is only determined by the PDF of the AoA. As the PDFs of the AoA of the three models are approximately equal as shown in Figure 3.5, it is not necessary to show the ACFs corresponding to the other models.

3.5.4 Doppler power spectral density (PSD)

In Figure 3.8, we present a comparison of the absolute values of the array-variant Doppler PSDs obtained through the transformation method, the approximation method, the spherical wavefront approach, and simulation, at the two extremes of the ULA and for different directions of motion ξ^R. The variations of the Doppler PSD along the array can be attributed to the difference in relative motion w.r.t. the scatterers at sufficiently separated antenna elements, e.g., A_1^R and A_{100}^R. It can be seen that not only the Doppler PSD drifts along the array, but also the Doppler spread is affected. On one hand, when the ULA points to the maximum concentration of the scatterers, i.e., $\alpha^R - \mu^\phi \approx 0$ or $\alpha^R - \mu^\phi \approx \pi$, the Doppler PSD hardly drifts, but there is a noticeable variation of the Doppler spread along the array. On the other hand, for a perpendicular orientation of the ULA, i.e., when $\alpha^R - \mu^\phi \approx \pm\pi/2$, the Doppler PSD tends to drift over the array, but the Doppler spread hardly varies.
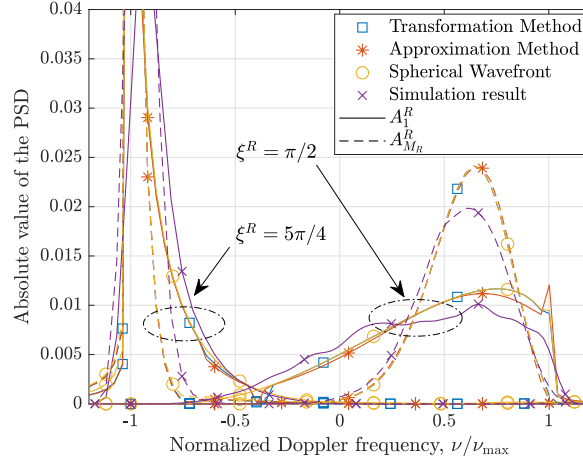
FIGURE 3.8: Comparison of the absolute values of the local Doppler PSD obtained by the transformation method, the approximation method, and simulation at the two extremes of the receiving array ($d = 100$ m, $f_c = 2$ GHz, $\tau_0 = 400$ ns, $\sigma^\tau = 3.4$ ns, $\mu^\phi = \pi/5$, $\kappa = 10$, $N_R = 100$, $\delta_R = \lambda/2$, $\alpha^R = \pi/4$, $\nu_{\max} = 90$ Hz, $v^R = 13.5$ m/s, $\delta_T = 0$ m, $t = 0$).

3.5.5   Spatial cross-correlation function (S-CCF)

In Figure 3.9, we present a comparison of the absolute values of the array-variant receive-side S-CCFs obtained by using the transformation method, the approximation method of variant parameters, the spherical wavefront approach, and simulation, at the receive antenna positions A_1^R and A_{100}^R for different values of the angular tilt of the receiving antenna α^R. There is clearly a good agreement between the transformation and approximation methods proposed. As in the ACFs presented in Figure 3.7, the differences between the transformation and approximation methods can be attributed to the fact that the latter assumes that the function determining the PAS remains the same, e.g., von Mises (3.22), at any position of the array and only the parameters of that function, i.e., κ and μ^ϕ, are array-variant.

3.5.6   Frequency correlation function (FCF)

In Figure 3.10, the absolute values of the array-variant FCFs of the Ellipse, modified UDSM, and Gaussian cluster models are presented. In the figure, it can be seen that the variant distribution of the ToA results in array-variant FCFs as a consequence of the large dimensions of the receiving array. This effect is specially significant for
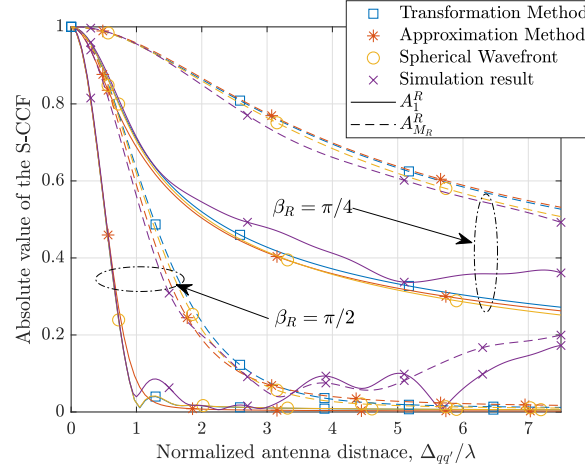
FIGURE 3.9: Comparison of the absolute values of the local S-CCF obtained by the transformation method, the approximation method, the spherical wavefront approach, and simulation at the two extremes of the receiving array ($d = 100$ m, $f_c = 2$ GHz, $\tau_0 = 400$ ns, $\sigma^\tau = 3.4$ ns, $\mu^\phi = \pi/5$, $\kappa = 10$, $N_R = 100$, $\delta_R = \lambda/2$, $\alpha^R = \pi/4$, $\delta_T = 0$ m, $t = 0$ s).

the modified UDSM and the Ellipse model. In the last one, the imposed narrowband property ($\sigma^\tau = 0.3$ ns) or frequency flatness is slowly degraded as the distance between the centre of the array and the considered antenna element increases. The cause of this artefact has already been explained in the analysis of Figure 3.3. As a consequence, what it was designed as a frequency non-selective and frequency-uncorrelated channel model may change to a frequency-selective and frequency-correlated channel for sufficiently large arrays. Note that in the case of the Ellipse model we have chosen
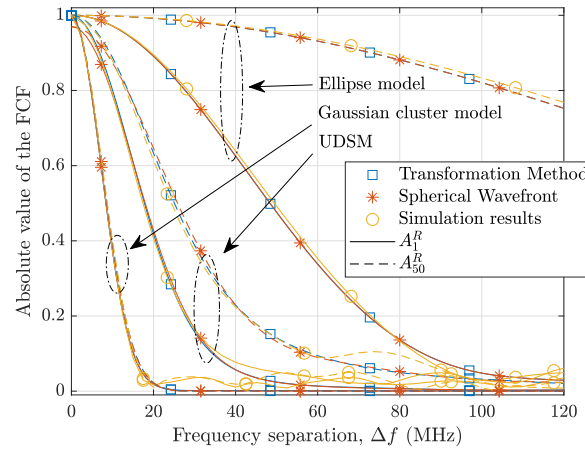
FIGURE 3.10: Comparison of the absolute values of the local FCFs at A_1^R and A_{50}^R obtained by the transformation method, the spherical wavefront approach, and simulation ($d = 100$ m, $f_c = 2$ GHz, $\tau_0 = 400$ ns, $r_0 \approx 11$ m, $\sigma^\tau = 0.3$ ns, $k_U = 10$, $\sigma^{xy} \approx 3.5$ m^{-1}, $\mu^\phi = \pi/5$, $\kappa = 10$, $N_R = 100$, $\delta_R = \lambda/2$, $\alpha^R = \pi/2$, $\delta_T = 0$ m, $t = 0$ s).

65

a sufficiently small value of the delay spread σ^τ to consider the channel as frequency non-selective in most practical cases, as it can be seen in the almost-flat FCF depicted for A_{50}^R. Conversely, the FCF of the Gaussian cluster model is barely affected as the shift and rotation of a 2D symmetric Gaussian distribution only affects its mean values, but not its spread. Hence, its delay PSD only experiences a shift (see Figure 3.6 and Table 3.2), which affects the phase but not the absolute value of the FCF.

In general, channels with large delay spreads are less prone to experience variations of the FCF along the array as compared to channels with highly concentrated PDPs. We have observed that the variations of the FCF over the array are usually negligible when the delay spread is sufficiently large compared to the spread induced by the transformation over the array.

## 3.6   Summary

In this chapter, a novel method to model the STV joint PDF of the ToA and AoA for massive MIMO channels has been proposed. The method can be used to study massive MIMO channel characteristics of both channel measurements and channel models. In addition, an approximation method based on STV parameters of the AoA for the von Mises distribution has been presented and approximate closed-form expressions of key statistical properties of the channel have been derived. The statistical properties obtained with these two methods have shown a good agreement between them and with the spherical wavefront approach. The proposed methods incorporate the non-stationary properties of the channel model through the STV joint PDF of the ToA and AoA. Moreover, both the means and spreads of the AoA and ToA have been shown to vary over the array. As a consequence of the drift and spread of the delays, the FCF of massive MIMO channels is array-variant as well. Finally, it has been demonstrated that artifacts may appear when conventional MIMO models such as the Ellipse model and UDSM are applied to large-scale antenna arrays.

Chapter 4

Novel 3D Non-Stationary Massive MIMO Channel Models based on Cluster-Level Evolution

4.1 Introduction

In the previous massive MIMO channel modelling works [9], [13], [88]–[92], [95], the authors employed spherical wavefronts to capture the so-called near-field effects. This method requires computing the exact distance between every scattering object and every antenna element of a large-scale array. However, the flexibility and accuracy of this approach to model all possible scenarios is traded off against a high mathematical and computational complexity. Measurements reported in Chapter 2 and the results presented in Chapter 3 indicate that the AoAs tend to vary smoothly over the array and the rate of change is higher when the distance between the scatterers and the array is shorter. This observation can be used to develop a more efficient but sufficiently flexible and accurate method capable of capturing near-field effects.

In addition, existing massive MIMO GBSMs captured cluster (dis)appearance by employing BD processes [13], [88], [91], [92], [95] or VRs [90]. In those works, clusters occluded over small regions of the array were considered as multiple independent

clusters, i.e., once a cluster has disappeared over the array, it cannot reappear again with similar characteristics. This increases the number of clusters per simulation, underestimates the spatial-temporal correlation of the channel in the large-scale, and may not capture the blocking effect accurately.

It is worth noting that previous works assumed that cluster (dis)appearance is the main cause of large-scale fading over the array, but measurements [4], [16] demonstrated that large-scale fading of clusters, i.e., cluster shadowing, is not negligible. Very few works have considered this phenomenon. The authors in [89] employed an inverse-square law that captured path loss but no large-scale fading of clusters of MPCs. Similarly, other works approximated cluster-level large-scale fading using a single-slope attenuation model [90]. Although deterministic models such as map-based METIS model [9] used realistic maps to account for large-scale fading effects, its stochastic counterpart neglected cluster-level (re)appearance and shadowing.

This chapter introduces advanced and efficient methods that overcome the problems introduced above to capture near-field effects. The main contributions and novelties of this work are the following:

1. An efficient parabolic wavefront is proposed as an alternative to the spherical wavefront. As a second-order Taylor approximation to the spherical wavefront, the parabolic wavefront is a more mathematically and computationally efficient method to capture near-field effects and non-stationary properties of the channel in both space and time domains with a small degradation in accuracy.

2. An *cluster-level evolution* process to accurately capture large-scale fading over the array is proposed. First, cluster (re)appearance processes are employed to model the visibility of clusters and LoS to NLoS transitions. Second, shadowing processes are used to model smooth variations of the clusters' average power over the array and time domains.

3. Approximate expressions for the relationship between non-stationary properties of the channel, e.g., spatial-temporal Doppler frequency drifts, and the distances

between the transmitting and receiving arrays as well as between these arrays and clusters are provided.

4. A 3D extension of the RSM [117] to compute the amplitude and angular parameters of the 3D simulation model is derived and we use the von Mises Fisher (VMF) distribution to jointly model azimuth and zenith angles of the scatterers.

The rest of this chapter is organized as follows. Section 4.2 proposes a theoretical non-stationary wideband massive MIMO channel model. In this section, the parabolic wavefront and cluster-level evolution processes are described. Section 4.3 derives important statistical properties of the theoretical model, e.g., the spatial-temporal cross-correlation function (ST-CCF). In Section 4.4, a corresponding simulation model and its statistical properties are obtained, along with the 3D extension of the RSM. Section 4.5 shows the excellent agreement between the theoretical and simulation model results along with a comparison between the simulation results and measurements. Section 4.6 concludes the chapter.

4.2 A Theoretical Non-Stationary Wideband Massive MIMO Channel Model

Let us consider a 3D channel model represented in Figure 4.1 where the ULA at the Tx or base station is composed of N_T equally δ_T-spaced antenna elements oriented by the zenith and azimuth angles β^T and α^T, respectively. Similarly, the Rx or MS ULA is composed of N_R equally δ_R-spaced antenna elements oriented by the zenith and azimuth angles β^R and α^R, respectively. The pth transmit and qth receive antenna-elements are denoted by A_p^T and A_q^R, respectively. Moreover, the MS moves at a constant speed v^R in the direction indicated by the zenith and azimuth angles ζ^R and ξ^R, respectively. The signal received at the MS is a superposition of the LoS and scattered components through C_S single-bounce clusters (SBCs) and C_M multi-bounce clusters (MBCs). However, only the cth MBC is represented in the figure for clarity. This cluster is modeled as a one-to-one pair at both sides of the
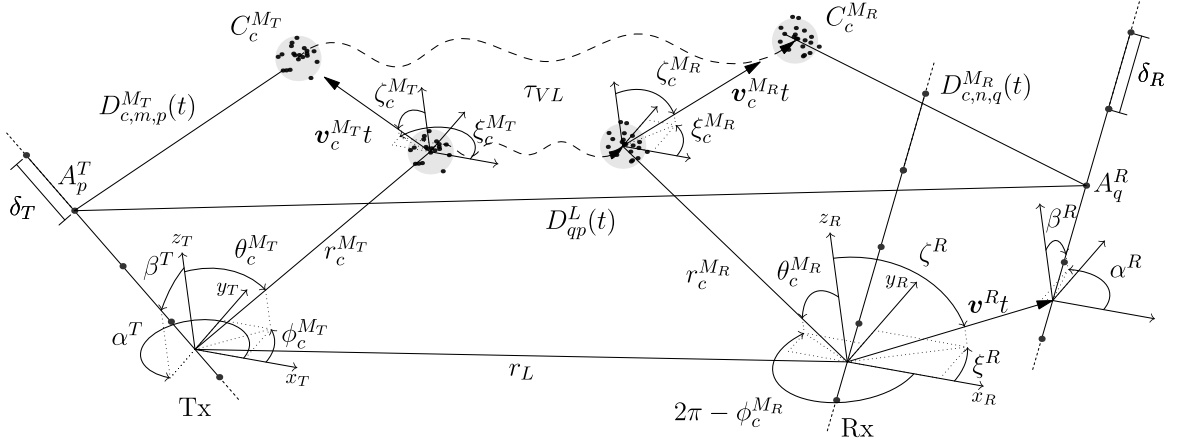
FIGURE 4.1: A 3D wideband massive MIMO channel model.

communication link, where the transmit-side MBC is represented as $\mathrm{C}_c^{\mathrm{M_T}}$ and the receive-side MBC as $\mathrm{C}_c^{\mathrm{M_R}}$ for $c = 1, 2, \ldots, C_{\mathrm{M}}$. Every pair of MBCs $\mathrm{C}_c^{\mathrm{M_T}} - \mathrm{C}_c^{\mathrm{M_R}}$ is connected through a virtual link that models the delay as in [82]. Clusters $\mathrm{C}_c^{\mathrm{M_T}}$ and $\mathrm{C}_c^{\mathrm{M_R}}$ are comprised of M_c and N_c scatterers, denoted as $\mathrm{S}_{c,m}^{\mathrm{M_T}}$ for $m = 1, 2, \ldots, M_c$ and $\mathrm{S}_{c,n}^{\mathrm{M_R}}$ for $n = 1, 2, \ldots, N_c$, respectively. Although the cth SBC, denoted as $\mathrm{C}_c^{\mathrm{S}}$, is a single cluster and has a uniquely defined position, it is convenient for notation simplicity to use two representations as $\mathrm{C}_c^{\mathrm{S_T}}$ and $\mathrm{C}_c^{\mathrm{S_R}}$ for $c = 1, 2, \ldots, C_{\mathrm{S}}$, denoting the SBC from the Tx and Rx frames of reference, respectively. The cth SBC $\mathrm{C}_c^{\mathrm{S}}$ is comprised of I_c scatterers whose transmit- and receive-side representations are denoted as $\mathrm{S}_{c,i}^{\mathrm{S_T}}$ and $\mathrm{S}_{c,i}^{\mathrm{S_R}}$ for $i = 1, 2, \ldots, I_c$, respectively. The position vector of the ith transmit-side SBC scatterer at time t is $\boldsymbol{s}_{c,i}^{\mathrm{S_T}}(t) = \boldsymbol{s}_{c,i}^{\mathrm{S_T}}(0) + \boldsymbol{v}_{c,i}^{\mathrm{S_T}}t$, with

$$\boldsymbol{s}_{c,i}^{\mathrm{S_T}}(0) = r_{c,i}^{\mathrm{S_T}}(\sin\theta_{c,i}^{\mathrm{S_T}}\cos\phi_{c,i}^{\mathrm{S_T}}, \sin\theta_{c,i}^{\mathrm{S_T}}\sin\phi_{c,i}^{\mathrm{S_T}}, \cos\theta_{c,i}^{\mathrm{S_T}}) \tag{4.1}$$

$$\boldsymbol{v}_{c,i}^{\mathrm{S_T}} = v_{c,i}^{\mathrm{S_T}}(\sin\zeta_{c,i}^{\mathrm{S_T}}\cos\xi_{c,i}^{\mathrm{S_T}}, \sin\zeta_{c,i}^{\mathrm{S_T}}\sin\xi_{c,i}^{\mathrm{S_T}}, \cos\zeta_{c,i}^{\mathrm{S_T}}) \tag{4.2}$$

denoting the initial position and velocity vectors of the scatterer, respectively. Similarly, the position vectors of receive-side scatterers are computed as in (4.1) and (4.2) by substituting $\mathrm{S_T}$ by $\mathrm{S_R}$. For clarity, the rest of the parameters of the channel model are presented in Table 4.1.

In general, it is assumed that every scatterer within a cluster is approximately at the same distance from the centre of the corresponding array and moves with the same velocity, e.g., $r_{c,i}^{\mathrm{S_T}} \approx r_c^{\mathrm{S_T}}$, $v_{c,i}^{\mathrm{S_T}} \approx v_c^{\mathrm{S_T}}$, $\zeta_{c,i}^{\mathrm{S_T}} \approx \zeta_c^{\mathrm{S_T}}$, and $\xi_{c,i}^{\mathrm{S_T}} \approx \xi_c^{\mathrm{S_T}}$. The centre

TABLE 4.1: Definition of parameters of the channel model in Figure 4.1.

Parameter	Definition
$\delta_{\mathrm{T}}, \delta_{\mathrm{R}}$	Distances between consecutive elements in the transmit- and receive-array, respectively
$r_c^{\mathrm{S_{T(R)}}}, r_c^{\mathrm{M_{T(R)}}}$	Distances from the centre of the transmit- (receive-) array to $\mathrm{C}_c^{\mathrm{S_{T(R)}}}$ and $\mathrm{C}_c^{\mathrm{M_{T(R)}}}$, respectively
$D_{c,i,p}^{\mathrm{S_T}}(t), D_{c,i,q}^{\mathrm{S_R}}(t)$	Distances from A_p^{T} to $\mathrm{S}_{c,i}^{\mathrm{S_T}}$ and from A_q^{R} to $\mathrm{S}_{c,i}^{\mathrm{S_R}}$, respectively
$D_{c,m,p}^{\mathrm{M_T}}(t), D_{c,n,q}^{\mathrm{M_R}}(t)$	Distances from A_p^{T} to $\mathrm{S}_{c,m}^{\mathrm{M_T}}$ and from A_q^{R} to $\mathrm{S}_{c,n}^{\mathrm{M_R}}$, respectively
r_{L}	Distance between the centres of the transmit- and the receive-array
$\theta_c^\ell, \phi_c^\ell$	Elevation and azimuth angles of C_c^ℓ with $\ell \in \{\mathrm{S_T}, \mathrm{S_R}, \mathrm{M_T}, \mathrm{M_R}\}$, respectively
$\theta_{c,i}^{\mathrm{S_{T(R)}}}, \phi_{c,i}^{\mathrm{S_{T(R)}}}$	Elevation and azimuth angles of the scatterer $\mathrm{S}_{c,i}^{\mathrm{S_{T(R)}}}$, respectively
$\theta_{c,m(n)}^{\mathrm{M_{T(R)}}}, \phi_{c,m(n)}^{\mathrm{M_{T(R)}}}$	Elevation and azimuth angles of the scatterer $\mathrm{S}_{c,m(n)}^{\mathrm{M_{T(R)}}}$, respectively
$\theta^{\mathrm{L}}, \phi^{\mathrm{L}}$	Elevation and azimuth angles of the Rx with respect to the Tx, respectively
ζ_c^ℓ, ξ_c^ℓ	Elevation and azimuth angles of the velocity of C_c^ℓ with $\ell \in \{\mathrm{S_T}, \mathrm{S_R}, \mathrm{M_T}, \mathrm{M_R}\}$, respectively
$\zeta^{\mathrm{R}}, \xi^{\mathrm{R}}$	Elevation and azimuth angles of the velocity vector of the Rx, respectively
$\beta^{\mathrm{T(R)}}, \alpha^{\mathrm{T(R)}}$	Elevation and azimuth orientation angles of the transmit (receive) array, respectively
v_c^ℓ, v^{R}	Speeds of the cluster C_c^ℓ with $\ell \in \{\mathrm{S_T}, \mathrm{S_R}, \mathrm{M_T}, \mathrm{M_R}\}$ and speed of the Rx, respectively

of the receive array with respect to the centre of the transmit array at any time t is $\boldsymbol{r}(t) = \boldsymbol{r}(0) + \boldsymbol{v}^{\mathrm{R}}t$, where

$$\boldsymbol{r}(0) = r_{\mathrm{L}} \left(\sin\theta^{\mathrm{L}}\cos\phi^{\mathrm{L}}, \sin\theta^{\mathrm{L}}\sin\phi^{\mathrm{L}}, \cos\theta^{\mathrm{L}} \right) \qquad (4.3)$$

$$\boldsymbol{v}^{\mathrm{R}} = v^{\mathrm{R}} \left(\sin\zeta^{\mathrm{R}}\cos\xi^{\mathrm{R}}, \sin\zeta^{\mathrm{R}}\sin\xi^{\mathrm{R}}, \cos\zeta^{\mathrm{R}} \right). \qquad (4.4)$$

The position vector of A_p^{T} from the centre of the transmit array is given by

$$\boldsymbol{a}_p^{\mathrm{T}} = \delta_p^{\mathrm{T}}(\sin\beta^{\mathrm{T}}\cos\alpha^{\mathrm{T}}, \sin\beta^{\mathrm{T}}\sin\alpha^{\mathrm{T}}, \cos\beta^{\mathrm{T}}) \qquad (4.5)$$

with $\delta_p^{\mathrm{T}} = (N_{\mathrm{T}} - 2p + 1)\delta_{\mathrm{T}}/2$ for $p = 1, 2, \ldots, N_{\mathrm{T}}$. The position vector of A_q^{R} from the centre of the receive array can be analogously obtained by substituting T by R and p by q in (4.5). Unlike conventional MIMO channel models, the far-field assumption or Rayleigh criterion, i.e., $r_{\mathrm{L}} \gg \max[2(N_{\mathrm{T}} - 1)^2\delta_{\mathrm{T}}^2, 2(N_{\mathrm{R}} - 1)^2\delta_{\mathrm{R}}^2]/\lambda$ and $r_c^\ell \gg \max[2(N_{\mathrm{T}} - 1)^2\delta_{\mathrm{T}}^2, 2(N_{\mathrm{R}} - 1)^2\delta_{\mathrm{R}}^2]/\lambda$ with $\ell \in \{\mathrm{S_T}, \mathrm{S_R}, \mathrm{M_T}, \mathrm{M_R}\}$, is not imposed.

4.2.1   Channel impulse response (CIR)

The massive MIMO channel is represented by the matrix $\boldsymbol{H}(t,\tau) = [h_{qp}(t,\tau)]_{N_{\mathrm{R}} \times N_{\mathrm{T}}}$ for $p = 1, 2, \ldots, N_{\mathrm{T}}$ and $q = 1, 2, \ldots, N_{\mathrm{R}}$. The CIR $h_{qp}(t,\tau)$ is calculated as a superposition of the LoS, SBC, and MBC components as

$$h_{qp}(t,\tau) = h_{qp}^{\mathrm{L}}(t)\delta(\tau - \tau^{\mathrm{L}}) + \sum_{c=1}^{C_{\mathrm{S}}} h_{c,qp}^{\mathrm{SB}}(t)\delta(\tau - \tau_c^{\mathrm{SB}}) + \sum_{c=1}^{C_{\mathrm{M}}} h_{c,qp}^{\mathrm{MB}}(t)\delta(\tau - \tau_c^{\mathrm{MB}}) \quad (4.6)$$

where the superscripts L, SB, and MB refer to LoS, SBC, and MBC components, respectively. The propagation delays $\tau^{\mathrm{L}}, \tau_c^{\mathrm{SB}}$, and τ_c^{MB} are computed geometrically as $\tau^{\mathrm{L}} = r_{\mathrm{L}}/c_0$, $\tau_c^{\mathrm{SB}} = (r_c^{\mathrm{S_T}} + r_c^{\mathrm{S_R}})/c_0$, and $\tau_c^{\mathrm{MB}} = (r_c^{\mathrm{M_T}} + r_c^{\mathrm{M_R}})/c_0 + \tau_{\mathrm{VL}}$, respectively, with c_0 denoting the speed of light and τ_{VL} the delay of the virtual link. Here, τ_{VL} is randomly generated according to the uniform distribution over $(\tau^{\mathrm{L}}, \tau_{\max}]$, where $\tau_{\max}$ is the maximum delay of the virtual link [88].

As there are I_c rays in the link A_p^T–C_c^{S}–A_q^R and $M_c \times N_c$ rays in the link A_p^T–$C_c^{\mathrm{M_T}}$–$C_c^{\mathrm{M_R}}$–A_q^R, the LoS, SBC, and MBC components of the CIR are modeled as

$$h_{qp}^{\mathrm{L}}(t) = \sqrt{P_{qp}^{\mathrm{L}}(t)} e^{jk_0 D_{qp}^{\mathrm{L}}(t)} \quad (4.7)$$

$$h_{c,qp}^{\mathrm{SB}}(t) = \sqrt{P_{c,qp}^{\mathrm{SB}}(t)} \lim_{I_c \to \infty} \sum_{i=1}^{I_c} a_{c,i} e^{-j(k_0 D_{c,i,qp}^{\mathrm{SB}}(t) - \Theta_{c,i}^{\mathrm{SB}})} \quad (4.8)$$

$$h_{c,qp}^{\mathrm{MB}}(t) = \sqrt{P_{c,qp}^{\mathrm{MB}}(t)} \lim_{\substack{M_c \to \infty \\ N_c \to \infty}} \sum_{\substack{m=1 \\ n=1}}^{M_c, N_c} a_{c,mn} e^{-j(k_0 D_{c,mn,qp}^{\mathrm{MB}}(t) - \Theta_{c,mn}^{\mathrm{MB}})} \quad (4.9)$$

with $j = \sqrt{-1}$ and $k_0 = 2\pi/\lambda$. The terms $\Theta_{c,i}^{\mathrm{SB}}$ and $\Theta_{c,mn}^{\mathrm{MB}}$ are independent and identically distributed (i.i.d.) random variables uniformly distributed over $(0, 2\pi]$ that model the phase shift produced by the scatterers. The amplitudes of the rays $a_{c,i}$ and $a_{c,mn}$ are constrained to $\mathbb{E}[a_{c,i}^2] = 1/I_c$ and $\mathbb{E}[a_{c,nm}^2] = 1/N_c M_c$ with $\mathbb{E}[\cdot]$ denoting the expectation operator. The processes $P_{qp}^{\mathrm{L}}(t)$, $P_{c,qp}^{\mathrm{SB}}(t)$, and $P_{c,qp}^{\mathrm{MB}}(t)$ are the array- and time-dependent local average powers associated to the LoS, SBCs, and MBCs paths, respectively (see Section 4.2.3). The distance travelled by the signal from A_p^{T}

to A_q^R via $S_{c,i}^S$ is $D_{c,i,qp}^{SB}(t) = D_{c,i,p}^{S_T}(t) + D_{c,i,q}^{S_R}(t)$, where

$$D_{c,i,p}^{S_T}(t) = \Big[(r_c^{S_T})^2 + (v_c^{S_T}t)^2 + (\delta_p^T)^2 + 2r_c^{S_T}v_c^{S_T}t\cos\psi_{1,c,i}^{S_T}$$
$$- 2r_c^{S_T}\delta_p^T\cos\psi_{2,c,i}^{S_T} - 2\delta_p^T v_c^{S_T}t\cos\psi_{3,c}^{S_T} \Big]^{1/2} \tag{4.10}$$

and the terms $\cos\psi_{1,c,i}^{S_T}$, $\cos\psi_{2,c,i}^{S_T}$, and $\cos\psi_{3,c}^{S_T}$ are given by

$$\cos\psi_{1,c,i}^{S_T} = \sin\theta_{c,i}^{S_T}\sin\zeta_c^{S_T}\cos(\phi_{c,i}^{S_T}-\xi_c^{S_T}) + \cos\theta_{c,i}^{S_T}\cos\zeta_c^{S_T} \tag{4.11}$$

$$\cos\psi_{2,c,i}^{S_T} = \sin\theta_{c,i}^{S_T}\sin\beta^T\cos(\phi_{c,i}^{S_T}-\alpha^T) + \cos\theta_{c,i}^{S_T}\cos\beta^T \tag{4.12}$$

$$\cos\psi_{3,c}^{S_T} = \sin\zeta_c^{S_T}\sin\beta^T\cos(\xi_c^{S_T}-\alpha^T) + \cos\zeta_c^{S_T}\cos\beta^T. \tag{4.13}$$

The receive-side distance $D_{c,i,q}^{S_R}(t)$ can be analogously computed by substituting T by R and p by q in (4.10)–(4.13). The vector $\boldsymbol{s}_{c,i}^{S_R}(t)$ is related to $\boldsymbol{s}_c^{S_T}(t)$ as $\boldsymbol{s}_{c,i}^{S_R}(t) = \boldsymbol{s}_{c,i}^{S_T}(t) - \boldsymbol{r}(t) = \boldsymbol{s}_{c,i}^{S_T}(0) - \boldsymbol{r}(0) + (\boldsymbol{v}_c^{S_T} - \boldsymbol{v}^R)t = \boldsymbol{s}_{c,i}^{S_R}(0) + \boldsymbol{v}_c^{S_R}t$. Hence, the spherical coordinates of $\boldsymbol{s}_c^{S_R}(0)$ are

$$\theta_{c,i}^{S_R} = \cos^{-1}\left(\frac{r_c^{S_T}\cos\theta_{c,i}^{S_T} - r_L\cos\theta^L}{r_c^{S_R}}\right) \tag{4.14}$$

$$\phi_{c,i}^{S_R} = \tan^{-1}\left(\frac{r_c^{S_T}\sin\theta_{c,i}^{S_T}\sin\phi_{c,i}^{S_T} - r_L\sin\theta^L\sin\phi^L}{r_c^{S_T}\sin\theta_{c,i}^{S_T}\cos\phi_{c,i}^{S_T} - r_L\sin\theta^L\cos\phi^L}\right) \tag{4.15}$$

where the distance $r_c^{S_R}$ from the centre of the receiving array to the SBC is given by

$$r_c^{S_R} = \left(r_L^2 + (r_c^{S_T})^2 - 2r_L r_c^{S_T}\cos\psi_{4,c,i}\right)^{1/2} \tag{4.16}$$

with

$$\cos\psi_{4,c,i} = \sin\theta_{c,i}^{S_T}\sin\theta^L\cos(\phi_{c,i}^{S_T}-\phi^L) + \cos\theta_{c,i}^{S_T}\cos\theta^L. \tag{4.17}$$

The distance travelled by the the rays from A_p^T to A_q^R via the cth MBC is $D_{c,mn,qp}^{MB}(t) = D_{c,m,p}^{M_T}(t) + D_{c,n,q}^{M_R}(t) + c_0 \cdot \tau_{VL}$, where

$$D_{c,m,p}^{M_T}(t) = \Big[(r_c^{M_T})^2 + (v_c^{M_T}t)^2 + (\delta_p^T)^2 + 2r_c^{M_T}v_c^{M_T}t\cos\psi_{1,c,m}^{M_T}$$
$$- 2r_c^{M_T}\delta_p^T\cos\psi_{2,c,m}^{M_T} - 2\delta_p^T v_c^{M_T}t\cos\psi_{3,c}^{M_T} \Big]^{1/2} \tag{4.18}$$

where $\cos \psi_{1,c,m}^{\mathrm{M_T}}$, $\cos \psi_{2,c,m}^{\mathrm{M_T}}$, and $\cos \psi_{c,3}^{\mathrm{M_T}}$ are computed analogously to (4.11)–(4.13) and hence they are omitted. The receive-side distance $D_{c,n,q}^{\mathrm{M_R}}(t)$ can be computed by substituting T by R, p by q, and m by n in (4.18). Unlike SBCs, there is no relationship between the transmit- and receive-side representations of MBCs.

The distance associated to the LoS path from A_p^{T} to A_q^{R} is

$$D_{qp}^{\mathrm{L}}(t) = \left[r_{\mathrm{L}}^2 + (v^{\mathrm{R}}t)^2 + (\delta_q^{\mathrm{R}})^2 + (\delta_p^{\mathrm{T}})^2 + 2r_{\mathrm{L}}v^{\mathrm{R}}t \cos \psi_1^{\mathrm{L}} + 2r_{\mathrm{L}}\delta_q^{\mathrm{R}} \cos \psi_2^{\mathrm{L}} \right.$$
$$\left. - 2r_{\mathrm{L}}\delta_p^{\mathrm{T}} \cos \psi_3^{\mathrm{L}} + 2\delta_q^{\mathrm{R}}v^{\mathrm{R}}t \cos \psi_4^{\mathrm{L}} - 2\delta_p^{\mathrm{T}}v^{\mathrm{R}}t \cos \psi_5^{\mathrm{L}} - 2\delta_q^{\mathrm{R}}\delta_p^{\mathrm{T}} \cos \psi_6^{\mathrm{L}} \right]^{1/2} \quad (4.19)$$

where the terms $\cos \psi_i^{\mathrm{L}}$ for $i = 1, 2, \ldots, 6$ are given by

$$\cos \psi_1^{\mathrm{L}} = \sin \theta^{\mathrm{R}} \sin \zeta^{\mathrm{R}} \cos(\phi^{\mathrm{R}} - \xi^{\mathrm{R}}) + \cos \theta^{\mathrm{R}} \cos \zeta^{\mathrm{R}} \quad (4.20)$$

$$\cos \psi_2^{\mathrm{L}} = \sin \theta^{\mathrm{R}} \sin \beta^{\mathrm{R}} \cos(\phi^{\mathrm{R}} - \alpha^{\mathrm{R}}) + \cos \theta^{\mathrm{R}} \cos \beta^{\mathrm{R}} \quad (4.21)$$

$$\cos \psi_3^{\mathrm{L}} = \sin \theta^{\mathrm{R}} \sin \beta^{\mathrm{T}} \cos(\phi^{\mathrm{R}} - \alpha^{\mathrm{T}}) + \cos \theta^{\mathrm{R}} \cos \beta^{\mathrm{T}} \quad (4.22)$$

$$\cos \psi_4^{\mathrm{L}} = \sin \zeta^{\mathrm{R}} \sin \beta^{\mathrm{R}} \cos(\xi^{\mathrm{R}} - \alpha^{\mathrm{R}}) + \cos \zeta^{\mathrm{R}} \cos \beta^{\mathrm{R}} \quad (4.23)$$

$$\cos \psi_5^{\mathrm{L}} = \sin \zeta^{\mathrm{R}} \sin \beta^{\mathrm{T}} \cos(\xi^{\mathrm{R}} - \alpha^{\mathrm{T}}) + \cos \zeta^{\mathrm{R}} \cos \beta^{\mathrm{T}} \quad (4.24)$$

$$\cos \psi_6^{\mathrm{L}} = \sin \beta^{\mathrm{T}} \sin \beta^{\mathrm{R}} \cos(\alpha^{\mathrm{T}} - \alpha^{\mathrm{R}}) + \cos \beta^{\mathrm{T}} \cos \beta^{\mathrm{R}}. \quad (4.25)$$

4.2.2 Spatial-temporal parabolic wavefronts

Equations (4.10), (4.18), and (4.19) enable to model near-field effects and non-stationary properties of the channel in arbitrary situations. However, second-order approximations to these expressions can capture the non-stationary properties of the CIR for small angular drifts and reduce the computational complexity. The second-order Taylor series expansion of the distance $D_{c,i,p}^{\mathrm{S_T}}(t)$ in (4.10) with respect to the ratios $\delta_p^{\mathrm{T}}/r_c^{\mathrm{S_T}}$ and $v_c^{\mathrm{S_T}}t/r_c^{\mathrm{S_T}}$ when $\delta_p^{\mathrm{T}}/r_c^{\mathrm{S_T}} < 1$ and $v_c^{\mathrm{S_T}}t/r_c^{\mathrm{S_T}} < 1$ is

$$D_{c,i,p}^{\mathrm{S_T}}(t) \approx \overbrace{r_c^{\mathrm{S_T}} + v_c^{\mathrm{S_T}}t \cos \psi_{1,c,i}^{\mathrm{S_T}} - \delta_p^{\mathrm{T}} \cos \psi_{2,c,i}^{\mathrm{S_T}}}^{\text{Plane-wavefront approximation}}$$
$$\underbrace{+ \frac{(v_c^{\mathrm{S_T}}t)^2}{2r_c^{\mathrm{S_T}}} \sin^2 \psi_{1,c,i}^{\mathrm{S_T}} + \frac{(\delta_p^{\mathrm{T}})^2}{2r_c^{\mathrm{S_T}}} \sin^2 \psi_{2,c,i}^{\mathrm{S_T}} + \frac{v_c^{\mathrm{S_T}}t\delta_p^{\mathrm{T}}}{r_c^{\mathrm{S_T}}} Q(\psi_{1,c,i}^{\mathrm{S_T}}, \psi_{2,c,i}^{\mathrm{S_T}}, \psi_{3,c}^{\mathrm{S_T}})}_{\text{Parabolic-wavefront approximation}} \quad (4.26)$$

where we defined $Q(\psi_i, \psi_j, \psi_k) = \cos\psi_i \cos\psi_j - \cos\psi_k$. Analogously, the distances $D_{c,i,q}^{\mathrm{S_R}}(t)$, $D_{c,m,p}^{\mathrm{M_T}}(t)$, and $D_{c,n,q}^{\mathrm{M_R}}(t)$ can be approximated by substituting $\{\mathrm{S_T}, i, p\}$ by $\{\mathrm{S_R}, i, q\}$, $\{\mathrm{M_T}, n, p\}$, and $\{\mathrm{M_R}, m, q\}$ in (4.26), respectively. The distance of the LoS path $D_{qp}^{\mathrm{L}}(t)$ can be approximated as

$$
D_{qp}^{\mathrm{L}}(t) \approx \overbrace{r_{\mathrm{L}} + v^{\mathrm{R}}t\cos\psi_1^{\mathrm{L}} + \delta_q^{\mathrm{R}}\cos\psi_2^{\mathrm{L}} - \delta_p^{\mathrm{T}}\cos\psi_3^{\mathrm{L}}}^{\text{Plane-wavefront approximation}}
$$

$$
\overbrace{+\frac{(v^{\mathrm{R}}t)^2}{2r_{\mathrm{L}}}\sin^2\psi_1^{\mathrm{L}} + \frac{(\delta_q^{\mathrm{R}})^2}{2r_{\mathrm{L}}}\sin^2\psi_2^{\mathrm{L}} + \frac{(\delta_p^{\mathrm{T}})^2}{2r_{\mathrm{L}}}\sin^2\psi_3^{\mathrm{L}}}^{\text{Parabolic-wavefront approximation}}
$$

$$
-\frac{\delta_q^{\mathrm{R}}v^{\mathrm{R}}t}{r_{\mathrm{L}}}Q(\psi_1^{\mathrm{L}}, \psi_2^{\mathrm{L}}, \psi_4^{\mathrm{L}}) + \frac{\delta_p^{\mathrm{T}}v^{\mathrm{R}}t}{r_{\mathrm{L}}}Q(\psi_1^{\mathrm{L}}, \psi_3^{\mathrm{L}}, \psi_5^{\mathrm{L}})
$$

$$
+\frac{\delta_q^{\mathrm{R}}\delta_p^{\mathrm{T}}}{r_{\mathrm{L}}}Q(\psi_2^{\mathrm{L}}, \psi_3^{\mathrm{L}}, \psi_6^{\mathrm{L}}). \tag{4.27}
$$

Unlike the first-order terms in (4.26) and (4.27), labeled as *plane-wavefront approximation*, the second-order terms and cross-products, labeled as *parabolic-wavefront approximation*, depend on the distances to the cluster $r_c^{\mathrm{S_T}}$ and between the arrays r_{L}, respectively. Subsequently, it will be shown that the second-order terms cause the non-stationarity of the CIR in time and space. In addition, the time-array cross-products, e.g., $v_c^{\mathrm{S_T}}t \cdot \delta_p^{\mathrm{T}}$, lead to a dependence of the S-CCF and temporal ACF with respect to time and space, respectively. Note that the second-order terms are reduced to zero for small arrays and short periods of time, i.e., $\delta_p^{\mathrm{T}}/r_{\mathrm{L}} \ll 1$, $\delta_p^{\mathrm{T}}/r_c^{\mathrm{S_T}} \ll 1$, $v^{\mathrm{R}}t/r_{\mathrm{L}} \ll 1$, and $v_c^{\mathrm{S_T}}t/r_c^{\mathrm{S_T}} \ll 1$. In these conditions, only the first-order terms in (4.26) and (4.27) remain as in conventional MIMO channel models [82], [83], [85]–[87].

On one hand, it is usually considered that the accuracy of the approximation obtained through the second-order expansion of (4.10) is excellent when the ratios $\delta_p^{\mathrm{T}}/r_{\mathrm{L}}, \delta_p^{\mathrm{T}}/r_c^{\mathrm{S_T}}, v^{\mathrm{R}}t/r_{\mathrm{L}}$, and $v_c^{\mathrm{S_T}}t/r_c^{\mathrm{S_T}}$ are lower than 0.1. Using this criterion, the parabolic wavefront approximation in (4.26) can be considered very accurate when the distance from the centre of the array to any cluster is at least 5 times the length of the ULA. Nonetheless, we will show in Section 4.5 that very accurate results of the statistical properties of the channel model can be obtained using the parabolic wavefront under less conservative conditions. On the other hand, the reduction of the

computational complexity associated to the parabolic wavefront compared to that of the spherical wavefront is obtained from the simplification of the exact distance in (4.10) to the second-order polynomial in (4.26). Firstly, with the same number of terms in (4.10) and (4.26), the second-order approximation does not require the repetitive computation of the square root function in (4.10) for every AoA in every cluster at any time instant and antenna element of the receive array. Secondly, efficient quadratic-phase rotation algorithms, which are analogous to the efficient linear-phase rotation algorithms used in the case of the plane wavefront [91], can be employed to compute the phase associated to the parabolic wavefront.

4.2.3   Cluster-level shadowing and reappearance

Variations of the average received power in time and over the array are caused by *(re)appearance* and *shadowing* of both LoS and cluster components, which are modeled here by *Markov two-state* and *Lognormal shadowing* processes, respectively. As in [115], in this work the WINNER+ [85] and COST 2100 [82] models are used as references for the development of the cluster evolution processes. In [85] and [82], the average power associated to the cth cluster, P_c, is modeled as

$$P_c = \exp\left[-\tau_c \frac{r_\tau - 1}{r_\tau \sigma_{\tau,c}}\right] \cdot 10^{-\frac{\eta_c}{10}} \qquad (4.28)$$

where τ_c is the delay of the signal scattered by the cth cluster, $\sigma_{\tau,c}$ is the DS of the channel, and r_τ is the ratio of the standard deviation of the delays to the RMS DS. The parameter η_c is a zero-mean Gaussian random variable used to model a shadowing randomization effect on each cluster for each stationary simulation drop or segment [82], [85]. Since the cluster-level evolution processes for LoS, SBCs, and MBCs are analogous, only the SBC case will be considered in the following. Only when it is necessary, the differences between SBCs and MBCs will be pointed out. In this model, we propose the following modification

$$P_{c,qp}^{\text{SB}}(t) = \exp\left[-\tau_c \frac{r_\tau - 1}{r_\tau \sigma_{\tau,c}}\right] \cdot \gamma_{c,qp}^{\text{SB}}(t) \cdot \Pi_{c,qp}^{\text{SB}}(t) \qquad (4.29)$$

where the shadowing randomization factor $10^{-\frac{n_c}{10}}$ in (4.28) is superseded by the product of the processes $\gamma_{c,qp}^{\mathrm{SB}}(t)$ and $\Pi_{c,qp}^{\mathrm{SB}}(t)$. First, cluster (re)appearance (visibility) is modeled by a two-state Markov process $\Pi_{c,qp}^{\mathrm{SB}}(t)$. Second, smooth variations of the clusters average power in time domain and over both arrays are modeled by a Log-normal process $\gamma_{c,qp}^{\mathrm{SB}}(t)$. Analogously, transitions between LoS and NLoS states and smooth power variations of the LoS component are modeled by the processes $\Pi_{qp}^{\mathrm{L}}(t)$ and $\gamma_{qp}^{\mathrm{L}}(t)$, respectively. Thus, the local average power of the LoS component in (4.7) is $P_{qp}^{\mathrm{L}}(t) = \gamma_{qp}^{\mathrm{L}}(t) \cdot \Pi_{qp}^{\mathrm{L}}(t)$.

4.2.3.1 Spatial-temporal LoS/cluster reappearance

The product of the three two-state Markov processes $\Pi_c^{\mathrm{S_T}}(\delta_p^{\mathrm{T}})$, $\Pi_c^{\mathrm{S_R}}(\delta_q^{\mathrm{R}})$, and $\Pi_c^{\mathrm{SB}}(t)$ models cluster (re)appearance over the transmit- and receive-arrays and in time, respectively. As every cluster may only be visible over certain array and time intervals, these processes take value (0)1 if the cluster is (in)visible over the corresponding dimensions. The product of the processes is used because a cluster is visible only if it is visible from both sides of the communication link at the same time. Similarly to [13], [88], [101], the size of the invisibility and VRs of a cluster is modeled by exponential i.i.d. random variables with intensities λ_I and λ_V, respectively. For the spatial process $\Pi_c^{\mathrm{S_T}}(\delta_p^{\mathrm{T}})$ the transition matrix is [118]

$$\mathbf{T}_c(\delta_p^{\mathrm{T}}) = \begin{pmatrix} P_{I,c}^{\mathrm{S_T}} + P_{V,c}^{\mathrm{S_T}} e^{-\lambda_{T,c}^{\mathrm{S_T}}\delta_p^{\mathrm{T}}} & P_{V,c}^{\mathrm{S_T}} - P_{V,c}^{\mathrm{S_T}} e^{-\lambda_{T,c}^{\mathrm{S_T}}\delta_p^{\mathrm{T}}} \\ P_{I,c}^{\mathrm{S_T}} - P_{I,c}^{\mathrm{S_T}} e^{-\lambda_{T,c}^{\mathrm{S_T}}\delta_p^{\mathrm{T}}} & P_{V,c}^{\mathrm{S_T}} + P_{I,c}^{\mathrm{S_T}} e^{-\lambda_{T,c}^{\mathrm{S_T}}\delta_p^{\mathrm{T}}} \end{pmatrix} \tag{4.30}$$

where $\lambda_{T,c}^{\mathrm{S_T}} = \lambda_{V,c}^{\mathrm{S_T}} + \lambda_{I,c}^{\mathrm{S_T}}$. The entries in the transition matrix in (4.30) represent the probability of transition between visibility and invisibility regions of a cluster. The probabilities that a cluster is visible or invisible at any position along the array are $P_{V,c}^{\mathrm{S_T}} = \lambda_{V,c}^{\mathrm{S_T}}/\lambda_{T,c}^{\mathrm{S_T}}$ or $P_{I,c}^{\mathrm{S_T}} = \lambda_{I,c}^{\mathrm{S_T}}/\lambda_{T,c}^{\mathrm{S_T}}$, respectively. For the temporal process $\Pi_c^{\mathrm{SB}}(t)$, the transition matrix must be modified by substituting δ_p^{T} by the channel fluctuation $q(t)$, which can be expressed as $q(t) = (v_c^{\mathrm{S_T}} + v_c^{\mathrm{S_R}})t$ assuming constant cluster and Rx speeds [101]. Note that unlike the models in [13], [88], [101], the transition rates $\lambda_{V,c}^{\mathrm{S_T}}$ and $\lambda_{I,c}^{\mathrm{S_T}}$ might be different for every cluster and dependent of the characteristics of

the environment, hence resulting in a more flexible model. The total spatial-temporal (re)appearance process for SBCs is given by

$$\Pi_{c,qp}^{\mathrm{SB}}(t) = \Pi_c^{\mathrm{S_T}}(\delta_p^{\mathrm{T}}) \cdot \Pi_c^{\mathrm{S_R}}(\delta_q^{\mathrm{R}}) \cdot \Pi_c^{\mathrm{SB}}(t). \tag{4.31}$$

Finally, it is important to highlight that unlike previous models where clusters can only (dis)appear, the reappearance process proposed here can model clusters that keep their properties while they are occluded before becoming visible again. This results in a higher spatial consistency of the channel and reduces the total number of clusters generated per simulation.

4.2.3.2 Spatial-temporal LoS/cluster shadowing

Applying the concept of spatial shadowing processes described in [12], [119], [120], the spatial-temporal shadowing process $\gamma_{c,qp}^{\mathrm{SB}}(t)$ can be obtained as the product of three Lognormal processes: two spatial processes evaluated at the positions of every antenna element of the transmit/receive array and a temporal process to account for smooth power variations in time domain. The process $\gamma_{c,qp}^{\mathrm{SB}}(t)$ can be expressed as

$$\gamma_{c,qp}^{\mathrm{SB}}(t) = 10^{\left(m_c^{\mathrm{SB}} + \sigma_c^{\mathrm{SB}}\eta_c^{\mathrm{SB}}(t) + \sigma_c^{\mathrm{S_T}}\eta_c^{\mathrm{S_T}}(\delta_p^{\mathrm{T}}) + \sigma_c^{\mathrm{S_R}}\eta_c^{\mathrm{S_R}}(\delta_q^{\mathrm{R}})\right)/10} \tag{4.32}$$

where the terms $\eta_c^{\mathrm{S_T}}(\delta_p^{\mathrm{T}})$, $\eta_c^{\mathrm{S_R}}(\delta_q^{\mathrm{R}})$, and $\eta_c^{\mathrm{SB}}(t)$ are three independent real-valued zero-mean Gaussian WSS processes with unit variance. The parameters $\sigma_c^{\mathrm{S_T}}$, $\sigma_c^{\mathrm{S_R}}$, and σ_c^{SB} are the *shadow standard deviations* of the cluster's power and m_c^{SB} is called the *area mean*. Since they are zero-mean independent Gaussian processes, the resulting sum $\sigma_c^{\mathrm{S_T}}\eta_c^{\mathrm{S_T}}(\delta_p^{\mathrm{T}}) + \sigma_c^{\mathrm{S_R}}\eta_c^{\mathrm{S_R}}(\delta_q^{\mathrm{R}}) + \sigma_c^{\mathrm{SB}}\eta_c^{\mathrm{SB}}(t)$ is also a zero-mean Gaussian process whose standard deviation is $\sigma_c^e = [(\sigma_c^{\mathrm{S_T}})^2 + (\sigma_c^{\mathrm{S_R}})^2 + (\sigma_c^{\mathrm{SB}})^2]^{1/2}$. As indicated in (4.32), the standard deviations and area mean can be different for every cluster and dependent of the characteristics of the environment. Usually, the parameter m_c^{SB} depends on the distance between the arrays and the cluster, frequency, and other parameters of the path-loss model applied [119]. As it will be shown, the parameter σ_c^e controls the amplitude of the power variations over the array and in time.

The theoretical model of the process $\eta_c^{\mathrm{S_T}}(\delta_p^{\mathrm{T}})$ is an infinite sum-of-sinusoids (SoS) [12] given by

$$\eta_c^{\mathrm{S_T}}(\delta_p^{\mathrm{T}}) = \lim_{K_c^{\mathrm{S_T}} \to \infty} \sum_{n=1}^{K_c^{\mathrm{S_T}}} b_{c,n}^{\mathrm{S_T}} \cos\left(2\pi s_{c,n}^{\mathrm{S_T}} \delta_p^{\mathrm{T}} + \Theta_{c,n}^{\mathrm{S_T}}\right) \tag{4.33}$$

where $K_c^{\mathrm{S_T}}$, $s_{c,n}^{\mathrm{S_T}}$, $b_{c,n}^{\mathrm{S_T}}$, and $\Theta_{c,n}^{\mathrm{S_T}}$ denote the number of sinusoids, the spatial frequency, amplitude, and initial phase of each sinusoid, respectively. The phases $\Theta_{c,n}^{\mathrm{S_T}}$ are i.i.d. random variables uniformly distributed over $[0, 2\pi)$ and the amplitudes $b_{c,n}^{\mathrm{S_T}}$ are subject to the condition $\mathbb{E}[(b_{c,n}^{\mathrm{S_T}})^2] = 1/K_c^{\mathrm{S_T}}$. Analogously, the temporal Gaussian process $\eta_c^{\mathrm{SB}}(t)$ is given by

$$\eta_c^{\mathrm{SB}}(t) = \lim_{K_c^{\mathrm{SB}} \to \infty} \sum_{n=1}^{K_c^{\mathrm{SB}}} b_{c,n}^{\mathrm{SB}} \cos\left(2\pi \nu_{c,n}^{\mathrm{SB}} t + \theta_{c,n}^{\mathrm{SB}}\right) \tag{4.34}$$

where $\nu_{c,n}^{\mathrm{SB}}$ denotes the temporal frequency of the nth sinusoid and the rest of the parameters have an analogous meaning to those of the spatial processes in (4.33).

4.3 Statistical Properties of the Channel Model

In this section, key statistical properties of the model, e.g., the ST-CCF and Doppler frequency shifts, considering the parabolic wavefront, cluster (re)appearance, and cluster shadowing will be derived.

4.3.1 Spatial-temporal cross-correlation function (ST-CCF)

The ST-CCF is defined as $\mathbb{E}[h_{qp}(t, \tau) h_{q'p'}^*(t + \Delta t, \tau)]$ and it can be split into three terms as

$$\rho_{qp}(\delta_{\mathrm{T}}, \delta_{\mathrm{R}}, \Delta t, t) = \rho_{qp}^{\mathrm{L}}(\delta_{\mathrm{T}}, \delta_{\mathrm{R}}, \Delta t, t) + \sum_{c=1}^{C_{\mathrm{S}}} \rho_{c,qp}^{\mathrm{SB}}(\delta_{\mathrm{T}}, \delta_{\mathrm{R}}, \Delta t, t) + \sum_{c=1}^{C_{\mathrm{M}}} \rho_{c,qp}^{\mathrm{MB}}(\delta_{\mathrm{T}}, \delta_{\mathrm{R}}, \Delta t, t) \tag{4.35}$$

where uncorrelated scattering (US) in the delay domain was assumed. Due to the independence of the large- and small-scale fading processes, every ST-CCF can be

expressed as the product of a large- and small-scale ST-CCF, e.g., $\rho^{\mathrm{SB}}_{c,qp}(\delta_{\mathrm{T}}, \delta_{\mathrm{R}}, \Delta t, t) = \rho^{\mathrm{SB}}_{\mathrm{LS},c,qp}(\delta_{\mathrm{T}}, \delta_{\mathrm{R}}, \Delta t) \cdot \rho^{\mathrm{SB}}_{\mathrm{SS},c,qp}(\delta_{\mathrm{T}}, \delta_{\mathrm{R}}, \Delta t, t)$. Note that the large-scale ST-CCF does not depend on absolute time t since, as it will be demonstrated, the (re)appearance and shadowing processes are WSS. Next, these correlation functions will be derived.

4.3.1.1 Small-Scale ST-CCF

The small-scale ST-CCFs of the LoS, SBCs, and MBCs are given by

$$\rho^{\mathrm{L}}_{\mathrm{SS},qp}(\delta_{\mathrm{T}}, \delta_{\mathrm{R}}, \Delta t, t) = e^{-jk_0 \Delta^{\mathrm{L}}_{qp}(\delta_{\mathrm{T}}, \delta_{\mathrm{R}}, \Delta t, t)} \tag{4.36}$$

$$\rho^{\mathrm{SB}}_{\mathrm{SS},c,qp}(\delta_{\mathrm{T}}, \delta_{\mathrm{R}}, \Delta t, t) = \lim_{I_c \to \infty} \sum_{i=1}^{I_c} \mathbb{E}\left[a^2_{c,i} e^{-jk_0 \Delta^{\mathrm{SB}}_{c,i,qp}(\delta_{\mathrm{T}}, \delta_{\mathrm{R}}, \Delta t, t)} \right] \tag{4.37}$$

$$\rho^{\mathrm{MB}}_{\mathrm{SS},c,qp}(\delta_{\mathrm{T}}, \delta_{\mathrm{R}}, \Delta t, t) = \lim_{\substack{M_c \to \infty \\ N_c \to \infty}} \sum_{\substack{m=1 \\ n=1}}^{M_c, N_c} \mathbb{E}\left[a^2_{c,mn} e^{-jk_0 \Delta^{\mathrm{MB}}_{c,qp,nm}(\delta_{\mathrm{T}}, \delta_{\mathrm{R}}, \Delta t, t)} \right] \tag{4.38}$$

where the distance differences are obtained as $\Delta^{\mathrm{L}}_{qp}(\delta_{\mathrm{T}}, \delta_{\mathrm{R}}, \Delta t, t) = D^{\mathrm{L}}_{qp}(t) - D^{\mathrm{L}}_{q'p'}(t + \Delta t)$, $\Delta^{\mathrm{SB}}_{c,i,qp}(\delta_{\mathrm{T}}, \delta_{\mathrm{R}}, \Delta t, t) = D^{\mathrm{SB}}_{c,i,qp}(t) - D^{\mathrm{SB}}_{c,i,q'p'}(t + \Delta t)$, and $\Delta^{\mathrm{MB}}_{c,mn,qp}(\delta_{\mathrm{T}}, \delta_{\mathrm{R}}, \Delta t, t) = D^{\mathrm{MB}}_{c,mn,qp}(t) - D^{\mathrm{MB}}_{c,mn,q'p'}(t + \Delta t)$. Thus, using the second-order approximations in (4.26) and (4.27), it can be seen that $\Delta^{\mathrm{L}}_{qp}(\delta_{\mathrm{T}}, \delta_{\mathrm{R}}, \Delta t, t) \approx$

$$\begin{aligned}
\approx &-v^{\mathrm{R}} \Delta t \cos \psi^{\mathrm{L}}_1 - \Delta_{qq'} \cos \psi^{\mathrm{L}}_2 + \Delta_{pp'} \cos \psi^{\mathrm{L}}_3 - \frac{(v^{\mathrm{R}})^2 \Delta t (\Delta t + 2t)}{2r_{\mathrm{L}}} \sin^2 \psi^{\mathrm{L}}_1 \\
&- \frac{\Delta_{qq'}(\Delta_{qq'} + 2\delta^{\mathrm{R}}_q)}{2r_{\mathrm{L}}} \sin^2 \psi^{\mathrm{L}}_2 - \frac{\Delta_{pp'}(\Delta_{pp'} + 2\delta^{\mathrm{T}}_p)}{2r_{\mathrm{L}}} \sin^2 \psi^{\mathrm{L}}_3 \\
&+ \frac{v^{\mathrm{R}} t \Delta_{qq'} + v^{\mathrm{R}} \Delta t \delta_{q'}}{r_{\mathrm{L}}} Q(\psi^{\mathrm{L}}_1, \psi^{\mathrm{L}}_2, \psi^{\mathrm{L}}_4) - \frac{v^{\mathrm{R}} t \Delta_{pp'} + v^{\mathrm{R}} \Delta t \delta_{p'}}{r_{\mathrm{L}}} Q(\psi^{\mathrm{L}}_1, \psi^{\mathrm{L}}_3, \psi^{\mathrm{L}}_5) \\
&- \frac{(N_{\mathrm{R}} + 1)\delta_{\mathrm{R}} \Delta_{pp'} + (N_{\mathrm{T}} + 1)\delta_{\mathrm{T}} \Delta_{qq'} - (qp - q'p')\delta_{\mathrm{T}} \delta_{\mathrm{R}}}{r_{\mathrm{L}}} Q(\psi^{\mathrm{L}}_2, \psi^{\mathrm{L}}_3, \psi^{\mathrm{L}}_6).
\end{aligned} \tag{4.39}$$

where $\Delta_{pp'} = \delta_{\mathrm{T}}(p - p')$ and $\Delta_{qq'} = \delta_{\mathrm{R}}(q - q')$.

For the case of SBCs and MBCs in (4.37) and (4.38), it can be seen that the distance differences can be expressed as $\Delta^{\mathrm{SB}}_{c,i,qp}(\delta_{\mathrm{T}}, \delta_{\mathrm{R}}, \Delta t, t) = \Delta^{\mathrm{S}_{\mathrm{T}}}_{c,i,p}(\delta_{\mathrm{T}}, \Delta t, t) + \Delta^{\mathrm{S}_{\mathrm{R}}}_{c,i,q}(\delta_{\mathrm{R}}, \Delta t, t)$ for SBCs and $\Delta^{\mathrm{MB}}_{c,mn,qp}(\delta_{\mathrm{T}}, \delta_{\mathrm{R}}, \Delta t, t) = \Delta^{\mathrm{M}_{\mathrm{T}}}_{c,m,p}(\delta_{\mathrm{T}}, \Delta t, t) + \Delta^{\mathrm{M}_{\mathrm{R}}}_{c,n,q}(\delta_{\mathrm{R}}, \Delta t, t)$ for MBCs,

where $\Delta_{c,i,p}^{\mathrm{S_T}}(\delta_{\mathrm{T}}, \Delta t, t)$ is obtained as

$$\Delta_{c,i,p}^{\mathrm{S_T}}(\delta_{\mathrm{T}}, \Delta t, t) \approx -v_c^{\mathrm{S_T}} \Delta t \cos \psi_{1,c,i}^{\mathrm{S_T}} + \Delta_{pp'} \cos \psi_{2,c,i}^{\mathrm{S_T}} - \frac{(v_c^{\mathrm{S_T}})^2 \Delta t (\Delta t + 2t)}{2 r_c^{\mathrm{S_T}}} \sin^2 \psi_{1,c,i}^{\mathrm{S_T}}$$
$$- \frac{\Delta_{pp'} (\Delta_{pp'} + 2\delta_p^{\mathrm{T}})}{2 r_c^{\mathrm{S_T}}} \sin^2 \psi_{2,c,i}^{\mathrm{S_T}} - \frac{1}{r_c^{\mathrm{S_T}}} \left(v_c^{\mathrm{S_T}} t \Delta_{pp'} + v_c^{\mathrm{S_T}} \Delta t \delta_{p'} \right)$$
$$\times Q(\psi_{1,c,i}^{\mathrm{S_T}}, \psi_{2,c,i}^{\mathrm{S_T}}, \psi_{3,c}^{\mathrm{S_T}}) \tag{4.40}$$

The difference $\Delta_{c,i,q}^{\mathrm{S_R}}(\delta_{\mathrm{R}}, \Delta t, t)$ can be analogously computed by substituting $\mathrm{S_T}$ by $\mathrm{S_R}$ and p by q in (4.40). The terms $\Delta_{c,m,p}^{\mathrm{M_T}}(\delta_{\mathrm{T}}, \Delta t, t)$ and $\Delta_{c,n,q}^{\mathrm{M_R}}(\delta_{\mathrm{R}}, \Delta t, t)$ can be computed analogously and they are omitted here for brevity.

In the limit $I_c \to \infty$, the ST-CCF of the SBC in (4.37) can be computed as [12]

$$\rho_{\mathrm{SS},c,qp}^{\mathrm{SB}}(\delta_{\mathrm{T}}, \delta_{\mathrm{R}}, \Delta t, t) = \int_{-\pi}^{\pi} \int_0^{\pi} e^{-jk_0 \Delta_{c,qp}^{\mathrm{SB}}(\delta_{\mathrm{T}}, \delta_{\mathrm{R}}, \Delta t, t)} f_c^{\mathrm{S_T}}(\theta_c^{\mathrm{S_T}}, \phi_c^{\mathrm{S_T}}) \, \mathrm{d}\theta_c^{\mathrm{S_T}} \, \mathrm{d}\phi_c^{\mathrm{S_T}} \tag{4.43}$$

where the discrete random variables $\Delta_{c,i,qp}^{\mathrm{SB}}(\delta_{\mathrm{T}}, \delta_{\mathrm{R}}, \Delta t, t)$, $\phi_{c,i}^{\mathrm{S_{T(R)}}}$, $\theta_{c,i}^{\mathrm{S_{T(R)}}}$, $\psi_{1,c,i}^{\mathrm{S_{T(R)}}}$, and $\psi_{2,c,i}^{\mathrm{S_{T(R)}}}$ in (4.37) have been substituted by their continuous versions $\Delta_{c,qp}^{\mathrm{SB}}(\delta_{\mathrm{T}}, \delta_{\mathrm{R}}, \Delta t, t)$, $\phi_c^{\mathrm{S_{T(R)}}}$, $\theta_c^{\mathrm{S_{T(R)}}}$, $\psi_{1,c}^{\mathrm{S_{T(R)}}}$, and $\psi_{2,c}^{\mathrm{S_{T(R)}}}$, respectively. The function $f_c^{\mathrm{S_T}}(\theta_c^{\mathrm{S_T}}, \phi_c^{\mathrm{S_T}})$ denotes the joint-PDF of the elevation angle of departures (EAoDs) and AAoDs of $\mathrm{C}_c^{\mathrm{S}}$. The elevation angle of arrivals (EAoAs) and azimuth angle of arrivals (AAoAs) implicit in (4.43) are a function of the AoDs as indicated in (4.14) and (4.15).

Due to the angular independence of the transmit- and receive-side MBCs, this MBC contribution to the ST-CCF in (4.38) admits a Kronecker form as the product of the transmit-side and receive-side ST-CCFs, i.e., $\rho_{\mathrm{SS},c,qp}^{\mathrm{MB}}(\delta_{\mathrm{T}}, \delta_{\mathrm{R}}, \Delta t, t) = \rho_{\mathrm{SS},c,pp'}^{\mathrm{M_T}}(\delta_{\mathrm{T}}, \Delta t, t) \cdot \rho_{\mathrm{SS},c,qq'}^{\mathrm{M_R}}(\delta_{\mathrm{R}}, \Delta t, t)$. In the limit as $M_c, N_c \to \infty$, the transmit-side and receive-side ST-CCF are

$$\rho_{\mathrm{SS},c,pp'}^{\mathrm{M_T}}(\delta_{\mathrm{T}}, \Delta t, t) = \int_{-\pi}^{\pi} \int_0^{\pi} e^{-jk_0 \Delta_{c,pp'}^{\mathrm{M_T}}(\delta_{\mathrm{T}} \Delta t, t)} f_c^{\mathrm{M_T}}(\theta_c^{\mathrm{M_T}}, \phi_c^{\mathrm{M_T}}) \, \mathrm{d}\theta_c^{\mathrm{M_T}} \, \mathrm{d}\phi_c^{\mathrm{M_T}} \tag{4.44}$$

$$\rho_{\mathrm{SS},c,qq'}^{\mathrm{M_R}}(\delta_{\mathrm{R}}, \Delta t, t) = \int_{-\pi}^{\pi} \int_0^{\pi} e^{-jk_0 \Delta_{c,qq'}^{\mathrm{M_R}}(\delta_{\mathrm{R}}, \Delta t, t)} f_c^{\mathrm{M_R}}(\theta_c^{\mathrm{M_R}}, \phi_c^{\mathrm{M_R}}) \, \mathrm{d}\theta_c^{\mathrm{M_R}} \, \mathrm{d}\phi_c^{\mathrm{M_R}} \tag{4.45}$$

where the discrete random variables $\phi_{c,m}^{\mathrm{M_T}}$, $\phi_{c,n}^{\mathrm{M_R}}$, $\theta_{c,m}^{\mathrm{M_T}}$, $\theta_{c,n}^{\mathrm{M_R}}$, $\psi_{1,c,m}^{\mathrm{M_T}}$, $\psi_{1,c,n}^{\mathrm{M_R}}$, $\psi_{2,c,m}^{\mathrm{M_T}}$, $\psi_{2,c,n}^{\mathrm{M_R}}$, and $\Delta_{c,mn,qp}^{\mathrm{MB}}(\delta_{\mathrm{T}}, \delta_{\mathrm{R}}, \Delta t, t)$ in (4.38) have been substituted by $\phi_c^{\mathrm{M_T}}$, $\phi_c^{\mathrm{M_R}}$, $\theta_c^{\mathrm{M_T}}$, $\theta_c^{\mathrm{M_R}}$, $\psi_{1,c}^{\mathrm{M_T}}$, $\psi_{1,c}^{\mathrm{M_R}}$, $\psi_{2,c}^{\mathrm{M_T}}$, $\psi_{2,c}^{\mathrm{M_R}}$, and $\Delta_{c,qp}^{\mathrm{MB}}(\delta_{\mathrm{T}}, \delta_{\mathrm{R}}, \Delta t, t)$, respectively. The function $f_c^{\mathrm{M_T}}(\theta_c^{\mathrm{M_T}}, \phi_c^{\mathrm{M_T}})$ denotes the joint-PDF of the EAoD and AAoD of $\mathrm{C}_c^{\mathrm{M_T}}$ and $f_c^{\mathrm{M_R}}(\theta_c^{\mathrm{M_R}}, \phi_c^{\mathrm{M_R}})$ the joint-PDF of the EAoA and AAoA of $\mathrm{C}_c^{\mathrm{M_R}}$.

Equations (4.36)–(4.45), specially (4.40), show that the ST-CCF does not only depend on relative time and antenna positions Δt and $\Delta_{pp'}$, but also on absolute time t and antenna position δ_p^{T}, demonstrating the non-stationary properties of the CIR in both temporal and spatial (over the array) domains, respectively. The terms dependent of the ratios $v_c^{\mathrm{S_T}}t/r_c^{\mathrm{S_T}}, \delta_p^{\mathrm{T}}/r_c^{\mathrm{S_T}}$ indicate that the closer the cluster is to the Tx, the more it contributes to the non-stationarity of the CIR. In addition, the cross-products, e.g., $v^{\mathrm{R}}t \cdot \delta_p^{\mathrm{T}}, v_c^{\mathrm{S_T}}t \cdot \delta_p^{\mathrm{T}}$, introduce cross-dependencies into the correlation functions with respect to the time and space, i.e., the temporal ACF and S-CCF depend on the position over the array and on absolute time, respectively. In Section 4.5, it will be shown that these terms are responsible for the Doppler spectrum drifts along both dimensions. Moreover, the terms that depend on the ratios $v_c^{\mathrm{S_T}}\Delta t/r_c^{\mathrm{S_T}}$ and $\Delta_{pp'}/r_c^{\mathrm{S_T}}$ improve the accuracy of the ST-CCF compared to the conventional stationary MIMO models. Finally, it is worth noting that as the temporal ACFs depend on the pair of antennas A_p^{T} and A_q^{R} considered, they cannot be obtained from the ST-CCFs by setting $\delta_{\mathrm{T}} = \delta_{\mathrm{R}} = 0$, but setting $p = p'$ and $q = q'$ in (4.36)–(4.45).

4.3.1.2 Large-scale ST-CCF

Because cluster (re)appearance and shadowing processes are assumed to be independent for simplicity, the large-scale ST-CCF can be separated as the product of the ST-CCF of the cluster (re)appearance processes and that of the shadowing processes as

$$\rho_{\mathrm{LS}}^{\mathrm{SB}}(\delta_{\mathrm{T}}, \delta_{\mathrm{R}}, \Delta t) = \rho_{\Pi_{c,qp}}^{\mathrm{SB}}(\delta_{\mathrm{T}}, \delta_{\mathrm{R}}, \Delta t) \cdot \rho_{\gamma_{c,qp}}^{\mathrm{SB}}(\delta_{\mathrm{T}}, \delta_{\mathrm{R}}, \Delta t). \tag{4.46}$$

Similarly, since the spatial-temporal cluster (re)appearance process in (4.31) is expressed as the product of three independent processes, hence the ST-CCF of $\Pi_{c,qp}^{\mathrm{SB}}(t)$

can be calculated as $\rho_{\Pi_c}^{\text{SB}}(\delta_{\text{T}}, \delta_{\text{R}}, \Delta t) = \rho_{\Pi_c}^{\text{S}_{\text{T}}}(\delta_{\text{T}}) \cdot \rho_{\Pi_c}^{\text{S}_{\text{R}}}(\delta_{\text{R}}) \cdot \rho_{\Pi_c}^{\text{SB}}(\Delta t)$, where

$$\rho_{\Pi_c}^{\text{S}_{\text{T}}}(\delta_{\text{T}}) = \mathbb{E}[\Pi_c^{\text{S}_{\text{T}}}(\delta_p^{\text{T}})\Pi_c^{\text{S}_{\text{T}}}(\delta_{p'})] = P_{V,c}^{\text{S}_{\text{T}}}\left(P_{V,c}^{\text{S}_{\text{T}}} + P_{I,c}^{\text{S}_{\text{T}}}e^{-\lambda_{T,c}^{\text{S}_{\text{T}}}\delta_{\text{T}}|p-p'|}\right) \tag{4.47}$$

$$\rho_{\Pi_c}^{\text{SB}}(\Delta t) = \mathbb{E}[\Pi_c^{\text{SB}}(t)\Pi_c^{\text{SB}}(t+\Delta t)] = P_{V,c}^{\text{SB}}\left(P_{V,c}^{\text{SB}} + P_{I,c}^{\text{SB}}e^{-\lambda_{T,c}^{\text{SB}}|q(\Delta t)|}\right) \tag{4.48}$$

where the receive-side $\rho_{\Pi_c}^{\text{S}_{\text{R}}}(\delta_{\text{R}})$ can be computed by substituting T by R and p by q in (4.47). Note that (4.47) corrects [115, eq. (17)]. Since the total ST-CCF only depends on relative time and antenna elements, the process $\Pi_{c,qp}^{\text{SB}}(\delta_{\text{T}}, \delta_{\text{R}}, t)$ is WSS in these domains. It is worth noting that, since clusters can reappear, the correlation of the (re)apperance processes does not completely vanish for long distances between antenna elements, i.e., the reappearance of clusters introduces additional large-scale correlation.

As the shadowing processes associated to the transmit- and receive-arrays are considered independent, the ST-CCF of $\gamma_{c,qp}^{\text{SB}}(t)$ can be calculated as [12], [119]

$$\begin{aligned}\rho_{\gamma_{c,qp}}^{\text{SB}}(\delta_{\text{T}}, \delta_{\text{R}}, \Delta t) = &\exp\left(m_{0,c}^{\text{SB}} + (\sigma_{0,c}^{\text{SB}})^2[1 + \rho_{\eta_c}^{\text{SB}}(\Delta t)]\right) \\ &\times \exp\left((\sigma_{0,c}^{\text{S}_{\text{T}}})^2[1 + \rho_{\eta_c}^{\text{S}_{\text{T}}}(\delta_{\text{T}})]\right) \\ &\times \exp\left((\sigma_{0,c}^{\text{S}_{\text{R}}})^2[1 + \rho_{\eta_c}^{\text{S}_{\text{R}}}(\delta_{\text{R}})]\right)\end{aligned} \tag{4.49}$$

where it has been defined $m_{0,c}^{\text{SB}} = m_c^{\text{SB}}\ln(10)/10$, $\sigma_{0,c}^{\text{S}_{\text{T}}} = \sigma_c^{\text{S}_{\text{T}}}\ln(10)/10$, and $\sigma_{0,c}^{\text{S}_{\text{R}}} = \sigma_c^{\text{S}_{\text{R}}}\ln(10)/10$. In addition, the terms $\rho_{\eta_c}^{\text{S}_{\text{T}}}(\delta_{\text{T}})$, $\rho_{\eta_c}^{\text{S}_{\text{R}}}(\delta_{\text{R}})$, and $\rho_{\eta_c}^{\text{SB}}(\Delta t)$ denote the ACFs of the processes $\eta_c^{\text{S}_{\text{T}}}(\delta_p^{\text{T}})$, $\eta_c^{\text{S}_{\text{T}}}(\delta_q^{\text{R}})$, and $\eta_c^{\text{SB}}(t)$ defined in (4.33) and (4.34), respectively. For the Gaussian correlation model, the ACFs in (4.49) are [12]

$$\rho_{\eta_c}^{\text{S}_{\text{T}}}(\delta_{\text{T}}) = e^{-\delta_{\text{T}}^2|p-p'|^2/(D_c^{\text{S}_{\text{T}}})^2} \tag{4.50}$$

$$\rho_{\eta_c}^{\text{SB}}(\Delta t) = e^{-[(v_c^{\text{T}})^2+(v_c^{\text{R}})^2]\Delta t^2/(D_c^{\text{SB}})^2}. \tag{4.51}$$

The parameters $D_c^{\text{S}_{\text{T}}}$ and D_c^{SB} are called the *decorrelation distance* and *decorrelation time* and they are defined as the relative distance and time where the correlations in (4.50) and (4.51) become e^{-1}. Since the ACFs in (4.49)–(4.51) only depend on relative time and distances, the cluster shadowing process $\gamma_{c,qp}^{\text{SB}}(t)$ is WSS. Finally, as

$\rho_{\mathrm{LS}}^{\mathrm{MB}}(\delta_{\mathrm{T}}, \delta_{\mathrm{R}}, \Delta t)$ and $\rho_{\mathrm{LS}}^{\mathrm{L}}(\delta_{\mathrm{T}}, \delta_{\mathrm{R}}, \Delta t)$ are computed analogously, they are omitted.

4.3.2 Spatial-temporal Doppler frequency drifts

The non-stationary properties of the channel model result in a spatial-temporal variant Doppler PSD. Since the analysis for both SBCs and MBCs is similar and closed-form solutions can only be obtained for MBCs, the MBC case will be presented here. The instantaneous Doppler shift experienced by a ray scattered by a MBC can be computed as the time derivative of the phase $\Delta\Phi_{c,mn,qp}^{\mathrm{MB}}(t) = k_0 D_{c,mn,qp}^{\mathrm{MB}}(t)$ in (4.9) as

$$\nu_{c,mn,qp}^{\mathrm{MB}}(t) = \frac{1}{2\pi} \cdot \frac{\mathrm{d}\Delta\Phi_{c,mn,qp}^{\mathrm{MB}}(t)}{\mathrm{d}t} = \nu_{c,m,p}^{\mathrm{M_T}}(t) + \nu_{c,n,q}^{\mathrm{M_R}}(t) \tag{4.52}$$

where

$$\frac{\nu_{c,m,p}^{\mathrm{M_T}}(t)}{\nu_{\max}^{\mathrm{M_T}}} = \overbrace{\cos\psi_{1,c,m}^{\mathrm{M_T}}}^{\substack{\text{Conventional Tx}\\\text{Doppler shift}}} + t \cdot \overbrace{\frac{v_c^{\mathrm{M_T}}}{r_c^{\mathrm{M_T}}}\sin^2\psi_{1,c,m}^{\mathrm{M_T}}}^{\text{Temporal drift at Tx}} + \delta_p^{\mathrm{T}} \cdot \overbrace{\frac{1}{r_c^{\mathrm{M_T}}}Q(\psi_{1,c,m}^{\mathrm{M_T}}, \psi_{2,c,m}^{\mathrm{M_T}}, \psi_{3,c}^{\mathrm{M_T}})}^{\text{Array drift at Tx}} \tag{4.53}$$

$$\frac{\nu_{c,n,q}^{\mathrm{M_R}}(t)}{\nu_{\max}^{\mathrm{M_R}}} = \overbrace{\cos\psi_{1,c,n}^{\mathrm{M_R}}}^{\substack{\text{Conventional Rx}\\\text{Doppler shift}}} + t \cdot \overbrace{\frac{v_c^{\mathrm{M_R}}}{r_c^{\mathrm{M_R}}}\sin^2\psi_{1,c,n}^{\mathrm{M_R}}}^{\text{Temporal drift at Rx}} + \delta_q^{\mathrm{R}} \cdot \overbrace{\frac{1}{r_c^{\mathrm{M_R}}}Q(\psi_{1,c,n}^{\mathrm{M_R}}, \psi_{2,c,n}^{\mathrm{M_R}}, \psi_{3,c}^{\mathrm{M_R}})}^{\text{Array drift at Rx}} \tag{4.54}$$

with $\nu_{\max}^{\mathrm{M_T}} = v_c^{\mathrm{M_T}}/\lambda$, $\nu_{\max}^{\mathrm{M_R}} = v_c^{\mathrm{M_R}}/\lambda$. The normalized Doppler shift of the LoS component is obtained as

$$\frac{\nu_{qp}^{\mathrm{L}}(t)}{\nu_{\max}^{\mathrm{L}}} = \overbrace{\cos\psi_1^{\mathrm{L}}}^{\substack{\text{Conventional}\\\text{Doppler shift}}} + t \cdot \overbrace{\frac{v^{\mathrm{R}}}{r_{\mathrm{L}}}\sin^2\psi_1^{\mathrm{L}}}^{\text{Temporal drift}} + \delta_p^{\mathrm{T}} \cdot \overbrace{\frac{1}{r_{\mathrm{L}}}Q(\psi_1^{\mathrm{L}}, \psi_3^{\mathrm{L}}, \psi_5^{\mathrm{L}})}^{\text{Array drift at Rx}} - \delta_q^{\mathrm{R}} \cdot \overbrace{\frac{1}{r_{\mathrm{L}}}Q(\psi_1^{\mathrm{L}}, \psi_2^{\mathrm{L}}, \psi_4^{\mathrm{L}})}^{\text{Array drift at Rx}} \tag{4.55}$$

with $\nu_{\max}^{\mathrm{L}} = v^{\mathrm{R}}/\lambda$. The first term in (4.53) denotes the conventional Doppler shift in stationary MIMO channels [12], [82], [83], [85], [86]. The second term results in a linear Doppler frequency drift over time whose normalized slope is proportional to $v_c^{\mathrm{M_T}}/r_c^{\mathrm{M_T}}\sin^2\psi_{1,c,m}^{\mathrm{M_T}}$. The third term in (4.53) represents the effect of the antenna position along the array on the Doppler shift. Similarly to the second term, the Doppler shift experiences a linear drift over the array with a normalized slope proportional to $\delta_{\mathrm{T}}/r_c^{\mathrm{M_T}}Q(\psi_{1,c,m}^{\mathrm{M_T}}, \psi_{2,c,m}^{\mathrm{M_T}}, \psi_{3,c}^{\mathrm{M_T}})$. Thus, we can conclude that it is the ratio of the array length (cluster displacement) to the distance between the array and the clusters what

determines the contribution of the cluster to the channel non-stationarity over the array (in time domain).

For a uniformly distributed scattering over the 3D sphere, i.e., when $f_c^\ell(\theta_c^\ell, \phi_c^\ell) = \sin(\theta_c^\ell)/4\pi$ with $\ell \in \{\mathrm{M_T, M_R}\}$, we can obtain an explicit solution for the expected value of the Doppler frequency shift as $B_{\mathrm{MB}}^{(1)} = \mathbb{E}[\nu_{c,m,p}^{\mathrm{M_T}}] + \mathbb{E}[\nu_{c,n,q}^{\mathrm{M_R}}]$, where the transmit- and receive-side frequency shifts are given by $\mathbb{E}[\nu_{c,m,p}^{\mathrm{M_T}}] = \frac{2}{3}\frac{\nu_{\max}^{\mathrm{M_T}}}{r_c^{\mathrm{M_T}}}(v_c^{\mathrm{M_T}}t - \delta_p^{\mathrm{T}}\cos\psi_{3,c}^{\mathrm{M_T}})$ and $\mathbb{E}[\nu_{c,n,q}^{\mathrm{M_R}}] = \frac{2}{3}\frac{\nu_{\max}^{\mathrm{M_R}}}{r_c^{\mathrm{M_R}}}(v_c^{\mathrm{M_R}}t - \delta_q^{\mathrm{R}}\cos\psi_{3,c}^{\mathrm{M_R}})$, respectively. The Doppler frequency spread corresponding to the MBC can be obtained as $B_{\mathrm{MB}}^{(2)} = (\mathbb{E}[(\nu_{c,mn,qp}^{\mathrm{MB}})^2] - \mathbb{E}[\nu_{c,mn,qp}^{\mathrm{MB}}]^2)^{1/2}$ or, equivalently, as $B_{\mathrm{MB}}^{(2)} = (\mathbb{E}[(\nu_{c,m,p}^{\mathrm{M_T}})^2] + \mathbb{E}[(\nu_{c,n,q}^{\mathrm{M_R}})^2] - \mathbb{E}[\nu_{c,m,p}^{\mathrm{M_T}}]^2 - \mathbb{E}[\nu_{c,n,q}^{\mathrm{M_R}}]^2)^{1/2}$ where it has been used the fact that the transmit- and receive-side Doppler frequencies shifts are independent. Finally, the term $\mathbb{E}[(\nu_{c,m,p}^{\mathrm{M_T}})^2]$ is given by

$$
\mathbb{E}[(\nu_{c,m,p}^{\mathrm{M_T}})^2] = \frac{(\nu_{\max}^{\mathrm{M_T}})^2}{15}\left[5 + 8\left(\frac{v_c^{\mathrm{M_T}}t}{r_c^{\mathrm{M_T}}}\right)^2 - 16\left(\frac{v_c^{\mathrm{M_T}}t\delta_p^{\mathrm{T}}}{r_c^{\mathrm{M_T}}}\right)^2\cos\psi_{3,c}^{\mathrm{M_T}} \right.
$$
$$
\left. + \left(\frac{\delta_p^{\mathrm{T}}}{r_c^{\mathrm{M_T}}}\right)^2\left(1 + 2\cos\psi_{3,c}^{\mathrm{M_T}} + 5\cos^2\psi_{3,c}^{\mathrm{M_T}}\right)\right]. \tag{4.56}
$$

The term $\mathbb{E}[(\nu_{c,n,q}^{\mathrm{M_R}})^2]$ can be computed analogously and it is omitted here for brevity. The average Doppler frequency shift drifts over the array and in time in a similar fashion to the individual rays in (4.53) and (4.54). Notice that the drift of the average Doppler shift and Doppler spread depends on the orientation of the array with respect to the direction of motion, i.e., the angle $\psi_{3,c}^{\mathrm{M_T}}$. Furthermore, considering short periods of time and small-arrays, i.e., $\{v_c^{\mathrm{M_T}}t, (N_{\mathrm{T}}-1)\delta_{\mathrm{T}}\} \ll r_c^{\mathrm{M_T}}$, both $B_{\mathrm{MB}}^{(1)}$ and $B_{\mathrm{MB}}^{(2)}$ become spatial-temporal invariant as in conventional non-massive MIMO models. Closed-form expressions cannot be obtained for the SBC Doppler drifts because the AoA and AoD are interdependent.

4.4 Simulation Model and Statistical Properties

The implementation of the theoretical model is not possible as it requires an infinite number of scatterers. However, it is well known that a finite number of rays can approximate the statistical properties of the theoretical model [12]. As the procedure is the same for SBCs and MBCs, only SBCs will be presented here. The SBC component of the CIR for the simulation model is

$$\hat{h}_{c,qp}^{\mathrm{SB}}(t) = \sqrt{\hat{P}_{c,qp}^{\mathrm{SB}}(t)} \sum_{i=1}^{I_c} \hat{a}_{c,i} e^{j\hat{\Theta}_{c,i}^{\mathrm{SB}}} e^{-jk_0 \hat{D}_{c,i,qp}^{\mathrm{SB}}(t)} \qquad (4.57)$$

where $\hat{a}_{c,i}, \hat{\Theta}_{c,i}^{\mathrm{SB}}, \hat{D}_{c,i,qp}^{\mathrm{SB}}(t)$, and I_c are the simulation model parameters of the small-scale fading process, and $\hat{P}_{c,qp}^{\mathrm{SB}}(t)$ is the cluster's average power of the simulation model. For $\hat{P}_{c,qp}^{\mathrm{SB}}(t)$, the Gaussian processes $\hat{\eta}_{p,c}^{\mathrm{S_T}}(\delta_p^{\mathrm{T}})$, $\hat{\eta}_{q,c}^{\mathrm{S_R}}(\delta_q^{\mathrm{R}})$, and $\hat{\eta}_c(t)$ contained within $\hat{\gamma}_{c,qp}^{\mathrm{SB}}(t)$ are approximated by a finite number of sinusoids. Due to the similarity of the procedure, only the transmit-side process is presented here. Thus, the process $\hat{\eta}_c^{\mathrm{S_T}}(\delta_p^{\mathrm{T}})$ is defined as

$$\hat{\eta}_c^{\mathrm{S_T}}(\delta_p^{\mathrm{T}}) = \sum_{k=1}^{K_c^{\mathrm{S_T}}} \hat{b}_{c,k}^{\mathrm{S_T}} \cos\left(2\pi \hat{s}_{c,k}^{\mathrm{S_T}} \delta_p^{\mathrm{T}} + \hat{\Theta}_{c,k}^{\mathrm{S_T}}\right). \qquad (4.58)$$

In the simulation model, it is required to find reasonable values of the parameters $\{\hat{a}_{c,i}, \hat{\theta}_{c,i}^{\mathrm{S_T}}, \hat{\phi}_{c,i}^{\mathrm{S_T}}\}$ in (4.57) and $\{\hat{b}_{c,k}, \hat{s}_{c,k}\}$ in (4.58) in order to have a good approximation to the statistical properties of the theoretical model. Aside from the values of $\hat{\Theta}_{c,i}^{\mathrm{SB}}$ and $\hat{\Theta}_{k_c}^{\mathrm{S_T}}$ that are drawn from i.i.d. random variables uniformly distributed over the interval $(0, 2\pi]$, the remaining parameters can be obtained using the corresponding equations of the theoretical model, e.g., $\hat{D}_{c,i,qp}^{\mathrm{SB}}(t)$ in (4.57) can be obtained using (4.26). In this chapter, a 3D extension of the RSM [117] is used to compute the parameters of the small-scale fading processes, and the method of equal areas (MEA) [12] is used to compute the parameters of the cluster shadowing processes.

The small-scale ST-CCF of the simulation model for SBCs can be expressed as

$$\hat{\rho}_{\mathrm{SS},c,qp}^{\mathrm{SB}}(\delta_{\mathrm{T}}, \delta_{\mathrm{R}}, \Delta t, t) = \sum_{i=1}^{I_{E,c}I_{A,c}} \hat{a}_{c,i}^2 e^{-jk_0\hat{\Delta}_{c,i,qp}^{\mathrm{SB}}(\delta_{\mathrm{T}},\delta_{\mathrm{R}},\Delta t,t)} \tag{4.59}$$

where $I_{E,c}$ and $I_{A,c}$ denote the number of rays used in the simulation model in the zenith and azimuth planes, respectively, so the total number of rays in (4.57) is $I_c = I_{E,c}I_{A,c}$. In the RSM, the theoretical correlation functions in (4.43) can be approximated as midpoints Riemann sums of finite number of terms [117]. The angular parameters of the simulation model are assumed equally spaced in both the zenith and azimuth planes as $\hat{\theta}_{c,i}^{\mathrm{S_T}} = \pi/I_{E,c}\left(\lceil i/I_{E,c}\rceil - 1/2\right)$ and $\hat{\phi}_{c,i}^{\mathrm{S_T}} = 2\pi/I_{A,c}\left[(i-1/2) \mod I_{A,c}\right]$, with $i = 1, 2, \ldots, I_{E,c}I_{A,c}$. Here, $\lceil x \rceil$ denotes the least integer greater than or equal to x and $A \mod B$ the remainder after division of A by B. In addition, the parameter $\hat{\Delta}_{c,i,qp}^{\mathrm{SB}}(\delta_{\mathrm{T}}, \delta_{\mathrm{R}}, \Delta t, t)$ in (4.59) can be obtained by plugging $\hat{\theta}_{c,i}^{\mathrm{S_T}}$ and $\hat{\phi}_{c,i}^{\mathrm{S_T}}$ into (4.11)–(4.13) and these into (4.40). The parameters $\hat{a}_{c,i}$ in (4.59) can be obtained as [117]

$$\hat{a}_{c,i} = \left[\frac{f_c^{\mathrm{S_T}}\left(\hat{\theta}_{c,i}^{\mathrm{S_T}}, \hat{\phi}_{c,i}^{\mathrm{S_T}}\right)}{\sum_{i=0}^{I_{E,c}I_{A,c}} f_c^{\mathrm{S_T}}\left(\hat{\theta}_{c,i}^{\mathrm{S_T}}, \hat{\phi}_{c,i}^{\mathrm{S_T}}\right)}\right]^{1/2}. \tag{4.60}$$

The introduction of a new dimension (the zenith angle) into the model increases its complexity compared to its 2D counterpart, as it requires additional terms in the sum of complex exponential functions to represent the zenith component of the rays.

Secondly, the ACF of the SoS process in (4.58) is given by

$$\hat{\rho}_{\eta_c}^{\mathrm{S_T}}(\delta_{\mathrm{T}}) = \sum_{k=1}^{K_c^{\mathrm{S_T}}} \frac{(\hat{b}_{c,k}^{\mathrm{S_T}})^2}{2} \cos(2\pi \hat{s}_{c,k}^{\mathrm{S_T}}(p - p')\delta_{\mathrm{T}}). \tag{4.61}$$

For the Gaussian correlation model, the MEA assumes the amplitude of all sinusoids to be $\hat{b}_{c,k}^{\mathrm{S_T}} = \sqrt{2/K_c^{\mathrm{SB}}}$. In addition, the spatial frequencies $\hat{s}_{c,k}^{\mathrm{S_T}}$ can be obtained as [12]

$$\hat{s}_{c,k}^{\mathrm{S_T}} = \frac{1}{\pi D_c^{\mathrm{S_T}}}\mathrm{erf}^{-1}\left(\frac{k - 1/2}{K_c^{\mathrm{S_T}}}\right) \tag{4.62}$$

where $k = 1, 2, \ldots, K_c^{\mathrm{SB}}$ and $\mathrm{erf}^{-1}(\cdot)$ denotes the inverse error function.

4.5   Results and Analysis

Henceforth, the scatterers distribution within a cluster is modeled by the VMF distribution, which is defined by the mean zenith angle θ_μ, the mean azimuth angle ϕ_μ, and its concentration parameter $\kappa \geq 0$. The PDF of a VMF random variable is defined in spherical coordinates as [111]

$$f(\theta, \phi) = \frac{\kappa \sin \theta}{4\pi \sinh(\kappa)} e^{\kappa \left(\sin \theta_\mu \sin \theta \, \sin(\phi_\mu - \phi) + \cos \theta_\mu \cos \theta \right)}. \tag{4.63}$$

The concentration parameter κ determines the angular spread in both azimuth and zenith angles. A high value of κ produces a highly concentrated distribution and $\kappa = 0$ results in a uniform distribution on the 3D sphere. In general, the azimuth and zenith angles of the VMF are correlated, with the exception of $\kappa = 0$ and $\theta_\mu = 0$.

4.5.1   Small-scale statistical properties of the model

In Figures 4.2 A) and B), a performance comparison of the plane, parabolic, and spherical wavefronts using the theoretical model is presented. In particular, the absolute values of the transmit-side cluster-level array-variant ACFs and time-variant S-CCFs for a MBC and different values of the VMF concentration parameter are shown. For a fair comparison of the three wavefronts, it has been set $t = 0$ s and $p = p' = N_{\mathrm{T}}/2$ in (4.40) to obtain Figures 4.2 A) and B), respectively. This enables us to eliminate the influence of absolute time and antenna position on the ACFs and S-CCFs, respectively. Note that as the plane wavefront with static channel parameters cannot capture non-stationary properties of the channel in the spatial or temporal domains, the corresponding results do not show any difference at different antenna elements or time instants. Thus, only the results obtained with the plane wavefront at antenna A_{50}^{T} in Figure 4.2 A) and time instant $t = 0$ in Figure 4.2 B) are presented. The temporal ACFs (Figure 4.2 A)) and S-CCFs (Figure 4.2 B)) at the centre of the transmit-array ($p = 50$) and time $t = 0$, respectively, show negligible differences for the three different wavefronts as expected. However, unlike the plane wavefront

FIGURE 4.2: Comparison of the cluster-level transmit-side A) array-variant ACF ($t = 0$) s and B) time-variant S-CCF ($p = 50$) of the theoretical model using plane, parabolic, and spherical wavefronts for different values of VMF κ-factor ($f = 2$ GHz, $N_T = 100$, $\delta_T = \lambda/2$, $\beta^T = \pi/2$, $\alpha^T = 0$, $\theta_\mu = 3\pi/4$, $\phi_\mu = \pi/3$, $\zeta_c^{M_T} = \pi/2$, $\xi_c^{M_T} = \pi/6$, $r_c^{M_T} = 30$ m, $v_c^{M_T} = 5$ m/s).

model, the results obtained with the parabolic wavefront demonstrate that it can model non-stationary channels and approximate the corresponding results obtained with the spherical wavefront very well. Also, notice that the array and temporal variations of the ACFs and S-CCFs, respectively, are the result of the cross-products in (4.40) described in Section 4.3. Finally, it can be observed that the ACF at A_{100}^T is higher than that at A_1^T. The reason is that, as A_1^T is closer to the cluster than A_{100}^T, the aparent angular spread at A_1^T is higher than that at A_{100}^T. Accordingly, as the coherence time, i.e., the region where the ACF is above certain level, is inversely proportional to the angular spread, hence the ACF widens from A_1^T to A_{100}^T.

In Figures 4.3 A) and B), a comparison of the theoretical model, simulation model, and simulation results is presented through the absolute values of the transmit-side cluster-level time-variant ACFs and array-variant S-CCFs, respectively, for a MBC and different values of the VMF concentration parameter. Note that as the CIR is non-stationary and hence non-ergodic, the simulation results have been obtained by averaging over 10^4 realizations of the correlation functions. Unlike Figures 4.2 A) and B), these results demonstrate temporal and spatial non-stationarity through the ACFs and S-CCFs, respectively. It is worth noting the very good agreement between
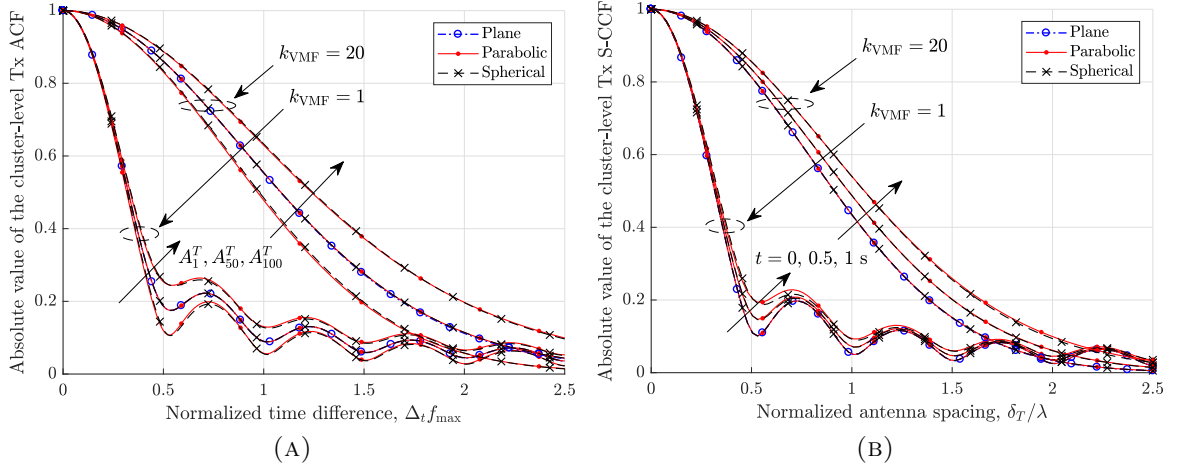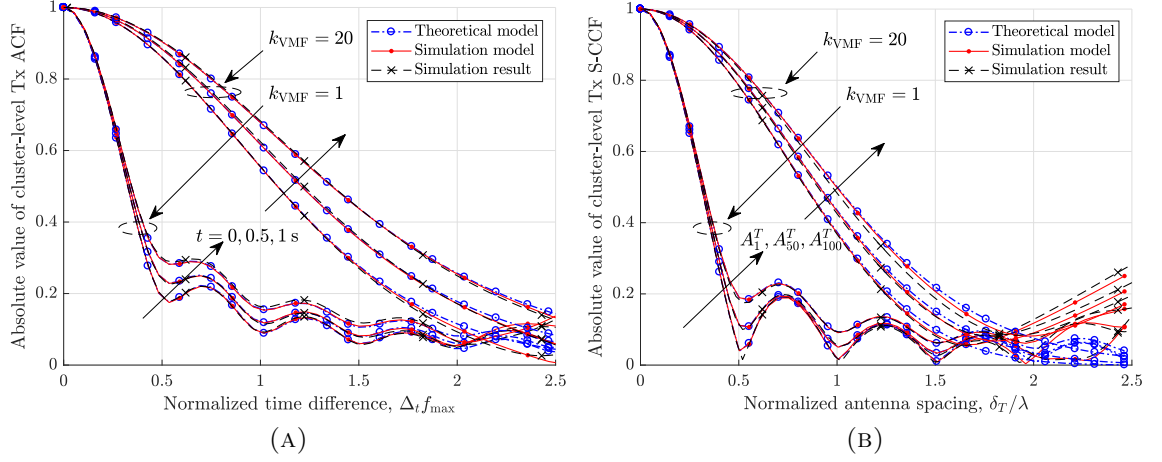
FIGURE 4.3: Comparison of the cluster-level transmit-side A) time-variant ACF ($p = 50$) and B) array-variant S-CCF ($t = 0$) of the theoretical model, simulation model, and simulation results for different values of VMF κ-factor ($f = 2$ GHz, $N_c^{\mathrm{M_T}} = M_c^{\mathrm{M_T}} = 15$, $N_{\mathrm{T}} = 100$, $\delta_{\mathrm{T}} = \lambda/2$, $\beta^{\mathrm{T}} = \pi/2$, $\alpha^{\mathrm{T}} = 0$, $\theta_\mu = 3\pi/4$, $\phi_\mu = \pi/3$, $\zeta_c^{\mathrm{M_T}} = \pi/2$, $\xi_c^{\mathrm{M_T}} = \pi/6$, $r_c^{\mathrm{M_T}} = 30$ m, $v_c^{\mathrm{M_T}} = 5$ m/s).

theoretical and simulation results obtained through the extended 3D RSM in non-stationary conditions. In this study, we verified that the 3D RSM outperforms the Monte Carlo method approximating the ACFs and S-CCFs in more than one order of magnitude using $N_c^{\mathrm{M_T}} = 8$ and $M_c^{\mathrm{M_T}} = 16$ in the EAoD and AAoD, respectively.

On the other hand, whereas the accuracy of the parabolic wavefront has already been assessed, the benefits in terms of computational complexity have not been shown yet. In order to provide an estimation of the computational gain, we used the ratio of the average simulation time of calculating plane, parabolic, and spherical wavefronts under the condition that all the rest parameters in the simulations were kept the same. To minimize the influence of the selected parameters on the results, random parameters in every simulation are drawn and later the average computation time over many realizations (10^4) is obtained. The ratios of the average computation time of computing plane, parabolic, and spherical wavefronts obtained are: $T_{\mathrm{plane}}/T_{\mathrm{spherical}} = 0.06$, $T_{\mathrm{plane}}/T_{\mathrm{parabolic}} = 0.35$, $T_{\mathrm{parabolic}}/T_{\mathrm{spherical}} = 0.17$. The plane wavefront is the most efficient but it cannot capture non-stationary properties of the channel. The average computation time of the parabolic wavefront is 17% of the average time required by the spherical wavefront, which demonstrates the efficiency of the proposed approach.

4.5.2 Large-scale statistical properties of the model

The large-scale characteristics of the proposed model were validated by employing the outdoor measurements reported in [16] and [5]. In [16], Gao *et al.* studied the distribution of the VRs length along the array by setting a 128-element virtual ULA spanning 7.5 m on the rooftop of a building in a semi-urban environment. In a similar setting [6] [5], Payami et al. studied the array-variant RMS DS by setting a virtual ULA composed by 128 omnidirectional antenna elements spaced half wavelength. In both cases, the measurements were performed in LoS and NLoS conditions at a central frequency of 2.6 GHz with a signal bandwidth of 50 MHz.

For the simulation results, if some channel parameters, e.g., carrier frequency, antenna separation, and number of antennas, were provided in the measurements (such as in [16] and [5]), they were directly employed in our simulations. The rest channel model parameters, e.g., $\lambda_{V,c}$, $\lambda_{I,c}$, σ_c, and D_c, were then estimated using an optimization algorithm in order to fit the statistical properties of the channel model to those of the measurement data. In the estimation process, random initial values of those parameters were first generated. Then, the average root mean square error of the simulation and measurement results was minimized by optimizing the values of those parameters in an iterative process. The following simulation results, e.g, CDFs, were obtained by using the Monte Carlo method, i.e., performing multiple simulation runs (10^4). A total number of 20 clusters per simulation run are employed with 25 sinusoids per cluster to generate the shadowing processes. Notice that $\lambda_{I,c}$ and $\lambda_{V,c}$, σ_c, and D_c are assumed to be equal for every cluster.

In Figure 4.4, the CDFs of the measured and simulated VRs' length over the array are presented for different values of the visibility rates. The VRs inside the array were selected for comparison as their information is complete and reliable [16]. Although the measurement and simulation curves for $\lambda_{I,c} = \lambda_{V,c} = 0.5$ m^{-1} are in good agreement for most of the range, there are discrepancies between these curves for low values of the VR's length, which can be explained due to the lack of reliable information for short VRs. Note that as the maximum length of a VR that can be measured over
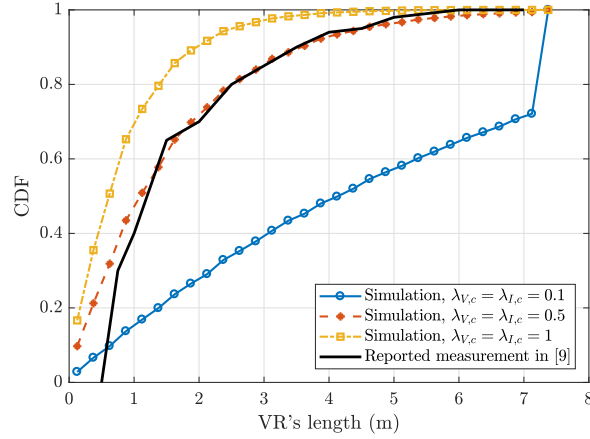
FIGURE 4.4: Measured [16] and simulated CDF of the clusters' VR lengths over the array ($f = 2.6$ GHz, $N_R = 128$, $\delta_R = \lambda/2$).

a ULA is equal to the length of the array (see [16, Figures 6 b-c]), we limited the maximum length of VRs to the ULA length. As a result, a discontinuity occurs in the CDF at a VR length of about 7.5 m for $\lambda_{I,c} = \lambda_{V,c} = 0.1$. In this case, whereas approximately 70% of VRs are strictly shorter than 7.5 m, 30% are longer than or equal to 7.5 m. Generally, it can be stated that the lower the cluster disappearance rate, the higher the percentage of clusters visible over the entire ULA and the larger the discontinuity.

In the VR approach for massive MIMO arrays developed in [16], the slopes of the clusters' average power variations along the array were employed to model cluster-level large-scale fading. These slopes were estimated in a least-squares sense in decibel domain. In Figure 4.5, the CDFs of the slopes simulated and estimated from measurements are presented for comparison purposes. Note that to estimate the values of the slopes by simulations, the values of the visibility rates $\lambda_{I,c} = \lambda_{V,c} = 0.5$ m^{-1} previously obtained (see Figure 4.4) are kept constant. It is worth noting that larger standard deviations of the clusters power σ_c tend to increase the spread of the slopes, whereas larger decorrelation distances produce the opposite effect. Moreover, it should be remarked that the area mean has little or no impact on the CDFs of the slopes.

Caused by the (re)appearance of clusters and smooth evolution of the clusters' average power along the array, variations of the RMS DS as reported in [5] need to be captured by massive MIMO channel models. For that purpose, in Figure 4.6 a comparison
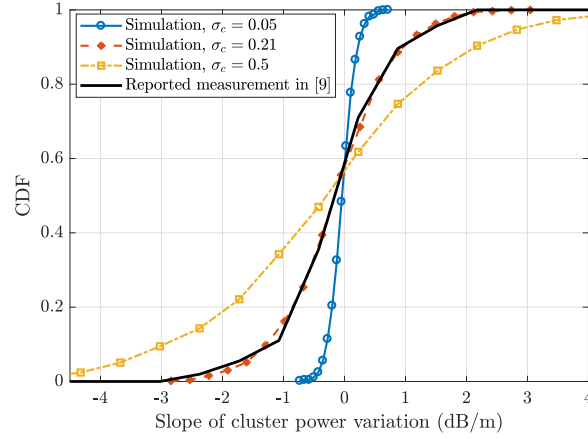
FIGURE 4.5: Measured and simulated CDF of slopes of the cluster's power variations along the array for different values of the standard deviation of the clusters' average power ($f = 2.6$ GHz, $\lambda_{I,c} = \lambda_{V,c} = 0.5$ m^{-1}, $D_c = 1.23$ m, $N_R = 128$, $\delta_R = \lambda/2$).
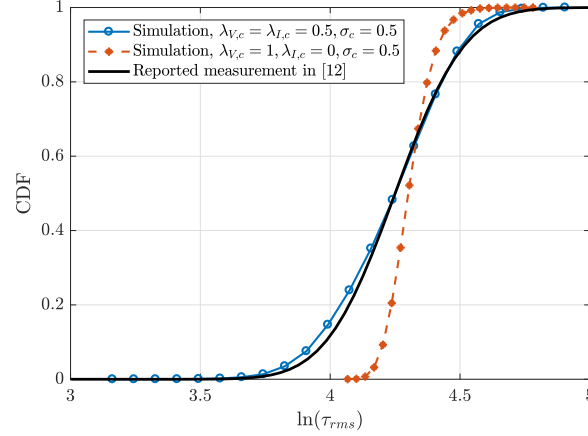
FIGURE 4.6: Comparison of the simulated and estimated [5] CDF of the array-variant RMS DS for different values of the (re)appearance rates and standard deviation of the clusters' average power ($f = 2.6$ GHz, $N_R = 128$, $\delta_R = \lambda/2$, $D_c = 1.23$ m).

of the simulated and measured CDFs of the RMS DS over the array is presented. The simulation results correspond to different values of the appearance rates and clusters' average power standard deviations. Whereas shadowing of clusters results in variations of the DS, adding both cluster (re)appearance and shadowing enables us to model such variations of the DS more accurately.

4.6   Summary

In this chapter, a novel 3D non-stationary wideband theoretical channel model and a corresponding simulation channel model for massive MIMO communication systems have been presented. First, a new efficient and accurate way of capturing spatial-temporal non-stationary properties of the channel through parabolic wavefronts has been proposed. It has been shown that the parabolic wavefront is sufficiently flexible and accurate to model the statistical properties of the channel with reduced computational complexity. Moreover, the relationship between non-stationary properties of the channel, e.g., time- and array-variant ST-CCFs and Doppler frequency drifts, and the distance between the arrays and clusters has been demonstrated. Second, non-stationary properties of the channel have also been modeled through cluster-level evolution processes in space and time domains. A comparison of simulation results and measurements has validated the spatial-temporal cluster (re)appearance and Log-normal shadowing processes in order to approximate key statistical properties of the channel such as the length of the clusters' VRs, the array-variant cluster power and array-variant DS. Finally, a 3D extension of the RSM for parameters computation has been proposed and validated through simulations.

Chapter 5

A Novel 3D Non-Stationary Massive MIMO Channel Model based on Ray-Level Evolution

5.1 Introduction

As introduced in Chapter 2, near-field effects take place when the distance between the array and the scatterers is shorter than the Rayleigh distance, which is $2D_A^2/\lambda$ with D_A denoting the largest dimension of the array and λ the carrier wavelength. It is important to note that the Rayleigh distance was originally derived assuming free-space LoS propagation and does not consider other phenomena related to multipath propagation [121], [122]. In agreement with this definition of Rayleigh distance, the largest dimension of the array is commonly used to determine which wavefront is the most adequate for each MPC or ray. This assumes that MPCs are received by all antennas of the array regardless of its size, i.e., it does not consider clusters' lifespans over the array. Clearly, this is in contradiction with the phenomenon of cluster (dis)appearance over the array. This widespread criterion is employed in previous works, e.g., [9], [13], [88]–[92], [95], including the model presented in Chapter 4. In addition, it is assumed that rays' lifespans over the array were equal to that of clusters.

This leads to the wrong conclusion that high-order wavefronts are required for most clusters and rays. This problem is accentuated when one considers B5G antenna array geometries such as ELAAs in which the co-located assumption and sub-wavelength separation between antenna arrays is challenged [7]. Due to their large aperture, the conventional Rayleigh distance criterion applied to an ELAA implies that virtually every scatterer lies within the near-field region of the array and every scattered MPC is subject to spherical wave propagation. As discussed in Chapter 4, high-order wavefronts are computational more complex than the plane wavefront as they require to calculate the exact or high-order approximations to the distances between every antenna element of the array and the surrounding scatterers. Thus, an accurate method to determine the most appropriate wavefront for each MPC would help reduce the complexity of existing massive MIMO channel models.

Most massive MIMO channel models [9], [13], [88], [89], [91]–[94] consider large-scale fading over the array by focusing on the array-varying number of clusters either employing Markov BD processes [13], [88], [89], [91], [92], [94], [115], [116] or VRs [90]. Aside from cluster (dis)appearance, very few works modeled cluster-level large-scale fading over the array. In [89], the authors included cluster-level path loss, but neglected shadow fading. In [90] and [91], only the slope of the cluster-level large-scale fading was considered. However, cluster-level large scale fading will be particularly important for the B5G channel models required by ELAAs as they will suffer from strong shadowing effects due to the extreme size of the array [7]. In addition, recent works [58] and [62] have shown the impact of an accurate modelling of large-scale fading over the array on the achievable SE. In particular, the authors proved that *unlimited* capacity can be achieved in multi-user massive MIMO systems employing M-MMSE precoding/combining envisioned for B5G communication systems.

In addition, existing models predict that the random number of clusters at any location of the array is Poisson distributed. However, measurements in [16] reported that a negative Binomial distribution is more accurate. How to resolve this apparent contradiction is still an open question.

It was discussed in Chapter 3 that the variations of the delay over the array become more significant for large arrays, e.g., ELAAs, and nearby scatterers. However, very few massive MIMO channel models [9], [91] have incorporated and studied the impact of the delay drift on the statistical properties of the channel. In Chapter 3, the array-varying PDF of the delay was studied, but its effect on the FCF was presented in isolation without considering the visibility of scatterers across the array.

Recent measurements that employed advanced clustering and sub-cluster tracking algorithms demonstrated the existence of massive MIMO effects such as near-field effects and (dis)appearance of both clusters and individual MPCs or rays as well [4]. These findings indicate that a more efficient use of wavefronts and a more accurate modelling of sub-cluster (dis)appearance can be achieved. Models including these phenomena and comprehensive studies of its impact on the their statistical properties are still missing. Although the model proposed in Chapter 4 captured the large-scale fading through (re)appearance and shadowing of clusters, it did not considered MPC (dis)appearance and smooth transitions between VRs.

To fill this gap, this chapter proposes a 3D non-stationary massive MIMO channel model that includes ray-level evolution and studies its effects into the small- and large-scale channel statistical properties. The main contributions and novelties of this chapter are the following:

1. A novel 3D non-stationary wideband massive MIMO channel model that is able to capture space-time ray-level evolution is proposed. The evolution process can flexibly control rays' lifespans and smoothness of (dis)appearance in both space and time domains. Cluster-level large-scale fading is automatically embedded in the model as a consequence of the ray-level process and smooth cluster-level (dis)appearance is guaranteed. The proposed channel model is suitable for 3D antenna-array layouts of arbitrary shape.

2. A novel method to accurately determine the most adequate wavefront for each cluster and ray is presented. For that purpose, the concept of effective Rayleigh distance, which accounts for the limited rays' lifespan over large-scale antenna

arrays, is proposed. In addition, it is proved that the use of the proposed method can significantly reduce the number of rays requiring spherical wavefronts.

3. Closed-form expressions of key statistical properties of the ray-level evolution process are derived and the impact of its parameters on the statistical properties of the proposed channel model is studied. The correctness of the derivations in this chapter are validated through simulations.

4. A Gamma-Poisson mixture is proposed to model the number of clusters when multiple locations of the mobile station are considered. This model resolves the apparent contradiction between previous channel measurements and models in order to fit the distribution of the random number of clusters appropriately.

The rest of this chapter is organized as follows. Section 5.2 introduces the proposed 3D massive MIMO channel model including the ray-level evolution process and the improved Rayleigh criterion for ray-level wavefront selection. The derivations of the channel model statistical properties, study of the impact of the ray evolution process and the Gamma-Poisson mixture distribution to model the number of clusters are included in Section 5.3. Section 5.4 studies the statistical properties of the channel model through numerical and simulation results and verifies the correctness of the derivations. Finally, conclusions are drawn in Section 5.5.

5.2   A Wideband Massive MIMO Channel model

Let us consider a generic 3D wireless channel in which the Tx and Rx can be equipped with arbitrary-shaped 3D antenna arrays. For simplicity, we assume that only the Rx is equipped with a large number of antennas. The p-th ($p = 1, 2, ..., N_T$) transmitting and q-th ($q = 1, 2, ..., N_R$) receiving omnidirectional antenna elements are denoted as A_p^T and A_q^R, respectively. The position vector and distance of the antenna A_p^T (A_q^R) measured from the centre of the transmitting (receiving) array are denoted as $\boldsymbol{a}_p^T$ ($\boldsymbol{a}_q^R$) and $\delta_p^T = ||\boldsymbol{a}_p^T||$ ($\delta_q^R = ||\boldsymbol{a}_q^R||$), respectively, with $|| \cdot ||$ denoting the Euclidian norm. Let us assume that the Tx (Rx) moves with a velocity $\boldsymbol{v}^T$ ($\boldsymbol{v}^R$) of constant magnitude
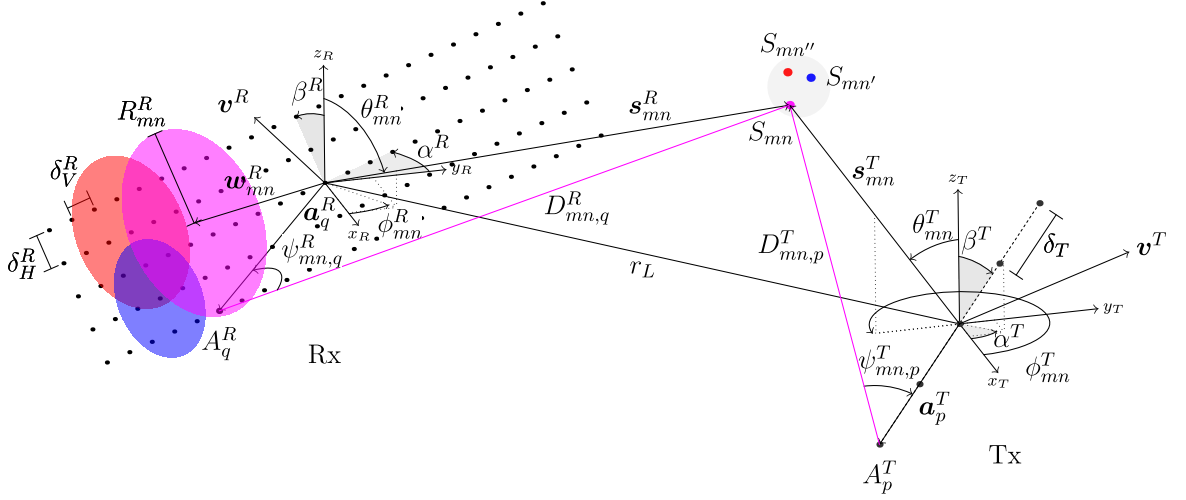
FIGURE 5.1: A 3D massive MIMO channel model including the visibility regions of individual scatterers across the large array.

v^T (v^R). Scattered rays with similar parameters, e.g., AoAs, AoDs, and delays, are grouped into C clusters of N_m, $m = 1 \dots C$, rays each. In the following, the n-th scatterer of the m-th cluster is denoted as S_{mn} and its position vector measured from the centre of the transmitting (receiving) array is denoted as $\boldsymbol{s}_{mn}^T$ ($\boldsymbol{s}_{mn}^R$). The azimuth and zenith AoDs (AoAs) of the scattered rays are denoted as ϕ_{mn}^T (ϕ_{mn}^R) and θ_{mn}^T (θ_{mn}^R), respectively. The most important elements of the channel model are depicted in Figure 5.1. For illustration purposes, we have employed a UPA at the receive side and a conventional ULA at the transmit side. For the UPA, the horizontal (vertical) inter-element spacing is denoted as δ_H^R (δ_V^R) and its orientation is modeled by the zenith and azimuth angles denoted as β^R and α^R, respectively. For the ULA, the inter-element spacing is denoted as δ_T and its orientation zenith and azimuth angles are denoted as β^T and α^T, respectively. Note that the regions of the UPA where individual scatterers are visible are depicted in color.

The massive MIMO channel is modeled by the matrix $\boldsymbol{H}(t, \tau) = [h_{qp}(t, \tau)]_{N_R \times N_T}$ with $p = 1, \dots, N_T$ and $q = 1, \dots, N_R$. The CIR $h_{qp}(t, \tau)$ can be calculated as

$$h_{qp}(t, \tau) = \sum_{m=1}^{C} a_m h_{m,qp}(t) \qquad (5.1)$$

with a_m denoting the m-th cluster's amplitude. The cluster-level CIR is defined as

$$h_{m,qp}(t) = \sum_{n=1}^{N_m} g_{mn,qp}(t) e^{j(k_0 D_{mn,qp}(t) + \theta_{mn})} \delta(\tau - \tau_{mn,qp}(t)) \qquad (5.2)$$

where $j = \sqrt{-1}$ and $k_0 = 2\pi/\lambda$. The term $g_{mn,qp}(t)$ accounts for the gain or amplitude of a ray that has travelled a distance $D_{mn,qp}(t)$ from A_q^T to A_q^R via S_{mn} at time instant t. The corresponding propagation delay is obtained as $\tau_{mn,qp}(t) = D_{mn,qp}(t)/c_0$, with c_0 denoting the speed of light. As signals from and to sufficiently separated antenna elements of the array experience different delays, note that $\tau_{mn,qp}(t)$ in (5.2) depends on the antenna indices p and q. In addition, scatterers introduce phase shifts θ_{mn}, which are usually modeled as i.i.d. random variables uniformly distributed over the interval $[0, 2\pi)$. The CTF of this model, defined as the Fourier transform of the CIR with respect to τ, is given by

$$H_{qp}(t, f) = \sum_{m=1}^{C} a_m \sum_{n=1}^{N_m} g_{mn,qp}(t) e^{j(k_0 D_{mn,qp}(t) + \theta_{mn})} e^{-j2\pi f \tau_{mn,qp}(t)}. \qquad (5.3)$$

5.2.1 Ray-level evolution process

In order to model the spatial-temporal ray-level evolution as it has been recently measured [4], we have selected a tapered cosine profile due to its flexibility and mathematical simplicity. The temporal definition of this function is as

$$g_{mn}(t) = \begin{cases} c_{mn} & 0 \le |t| < t'_{mn} \\ \frac{c_{mn}}{2} \left\{ 1 + \cos\left(\frac{2\pi}{r T_{mn}^R} \left[|t| - t'_{mn} \right] \right) \right\} & t'_{mn} \le |t| < \frac{T_{mn}^R}{2} \end{cases} \qquad (5.4)$$

and zero otherwise. The parameter c_{mn} denotes the maximum amplitude of the n-th ray in the m-th cluster, T_{mn}^R the period of time when the corresponding scatterer is visible (ray's lifetime), and the normalized *transition* or taper parameter $r \in (0, 1]$ denotes the ratio of the duration of the tapered region to the ray's lifetime. Small values of r model rapid transitions between zero and the maximum gain of the ray, i.e., rapid (dis)appearance, and vice versa. The term $t'_{mn} = (1 - r)T_{mn}^R/2$ denotes the time

separating the tapered from the constant-gain region. Note that the ray's lifetime T_{mn}^R is independent of the transition parameter r, i.e., the period of (dis)appearance is included in the ray's lifetime.

For an arbitrary-shaped 3D array at the receiving side, the gain in the spatial domain $g_{mn,qp}(\boldsymbol{a}_q^R)$ can be analogously defined by using the change of variables $t = ||\boldsymbol{a}_q^R - \boldsymbol{w}_{mn}^R||$ in (5.4), where $T_{mn}^R = 2R_{mn}^R$. In this case, the parameter R_{mn}^R denotes the radius of the ray's VR (see Figure 5.1). Note that this definition assumes spherical symmetry of the ray's gain for simplicity.

5.2.2 Spherical wavefront vs. plane wavefront

The total length of the path from A_p^T to A_q^R via S_{mn} used in (5.2) and (5.3) can be calculated as $D_{mn,qp}(t) = D_{mn,p}^T(t) + D_{mn,q}^R(t) + D_{mn,s}$, i.e.,

$$D_{mn,qp}(t) = \left\|\boldsymbol{s}_{mn}^T - \boldsymbol{a}_p^T - \boldsymbol{v}^T \cdot t\right\| + \left\|\boldsymbol{s}_{mn}^R - \boldsymbol{a}_q^R - \boldsymbol{v}^R \cdot t\right\| + D_{mn,s} \qquad (5.5)$$

where the term $D_{mn,s}$ denotes the propagation distance between the first and last scatterers. Clearly, for single-bounced signals $D_{mn,s} = 0$. However, due to the lack of information, multi-bounce scattering is usually abstracted as virtual link between the first and last bounces. The conventional approximation for short periods of time and small arrays, i.e., the first-order or plane-wavefront approximation, reduces the distance in (5.5) to [116]

$$D_{mn,qp}(t) \approx D_{mn} - \delta_p^T \cos \psi_{mn}^T - \delta_q^R \cos \psi_{mn}^R - v^T t \cos \xi_{mn}^T - v^R t \cos \xi_{mn}^R \qquad (5.6)$$

where D_{mn} is propagation distance from the centre of the transmitting array to the centre of the receiving array via S_{mn}. The angles ψ_{mn}^T, and ξ_{mn}^T can be obtained as

$$\cos \psi_{mn,p}^T = \frac{\boldsymbol{a}_p^T \cdot \boldsymbol{s}_{mn}^T}{||\boldsymbol{a}_p^T|| \cdot ||\boldsymbol{s}_{mn}^T||} \qquad (5.7)$$

$$\cos \xi_{mn}^T = \frac{\boldsymbol{v}^T \cdot \boldsymbol{s}_{mn}^T}{||\boldsymbol{v}^T|| \cdot ||\boldsymbol{s}_{mn}^T||}. \qquad (5.8)$$

The explicit dependency of the angles $\psi_{mn,p}^T$ and ξ_{mn}^T with respect to the azimuth and elevation AoDs can be seen in spherical coordinates as

$$\cos \psi_{mn,p}^T = \sin \theta_{mn}^T \sin \beta_p^T \cos(\phi_{mn}^T - \alpha_p^T) + \cos \theta_{mn}^T \cos \beta_p^T \qquad (5.9)$$

$$\cos \xi_{mn}^T = \sin \theta_{mn}^T \sin \beta_v^T \cos(\phi_{mn}^T - \alpha_v^T) + \cos \theta_{mn}^T \cos \beta_v^T \qquad (5.10)$$

where the terms α_p^T and β_p^T denote the azimuth and elevation components of A_p^T with respect to the centre of the transmitting array. Similarly, the terms α_v^T and β_v^T denote the azimuth and elevation components of the velocity vector $\boldsymbol{v}^T$, respectively. The angles $\psi_{mn,q}^R$ and ξ_{mn}^R are analogously obtained and are omitted here. In conventional WSS models [12], the plane-wavefront approximation in (5.6) is used to calculate the phase of the signal in (5.2) and (5.3). However, this first-order polynomial in δ_p^T, δ_q^R, and t results in linear spatial-temporal variations of the phase that do not capture the non-stationary properties of massive MIMO channels. In such case, the AoDs and AoAs are implicitly assumed to be constant over the array and time. Moreover, the delay $\tau_{mn,qp}(t)$ in (5.2) is usually approximated as a constant value for every path, i.e., $\tau_{mn,qp}(t) = \tau_{mn}$. However, this may be incorrect for large arrays and long periods of time as it has been recently shown in [123].

5.2.3   Wavefront selection: Effective Rayleigh distance

One of the advantages of the proposed ray-level process is the possibility of selecting the appropriate wavefront for each ray. The parameter commonly used to determine which wavefront is required is the Rayleigh distance, which is $D_R = 2D_A^2/\lambda$ with D_A denoting the largest dimension of the array and λ the carrier wavelength. However, as most clusters and rays only exist over very small regions of the array [4], [46], their effective Rayleigh distance is smaller than D_A. We define the effective Rayleigh distance of a ray as $D_{E,n} = 2\,(2R_n^R)^2/\lambda$ with R_n^R the radius of the ray's VR, i.e., with $2R_n^R$ being the ray's lifespan over the array. Thus, when a scatterer is located at a distance $r_n > D_{E,n}$ measured from the centre of the ray's VR, plane wavefronts can
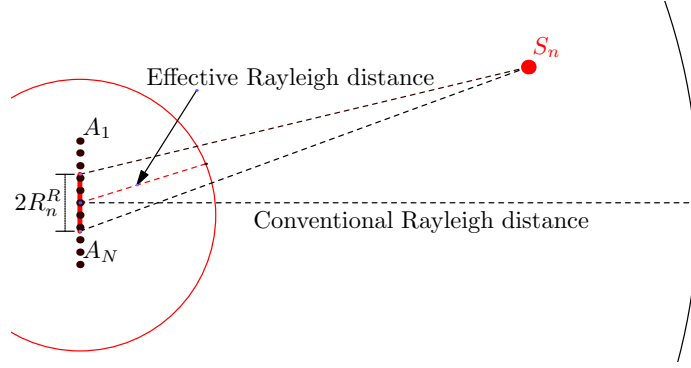
FIGURE 5.2: Comparison of the conventional Rayleigh distance calculated using the largest dimension of the array (black) and the proposed effective Rayleigh distance considering the ray's VR (red). The ray's lifespan is depicted as a red segment over the array.

be appropriately used. Figure 5.2 illustrates the concept of effective Rayleigh distance using a ULA.

Note that halving the radius of the ray's VR makes the effective Rayleigh distance four times shorter. The same concept can be applied to the time domain for which the effective Rayleigh distance is $2(v^R \cdot T_n^R)^2/\lambda$ with $T_n^R = 2R_n^R/v^R$, where it is assumed that the Rx moves at a constant speed v^R across the ray's VR.

Measurements in [4] have shown that R_n^R can accurately be approximated using i.i.d. exponentially distributed random variables of equal rate λ^R. Thus, for a particular cluster of scatterers located at distance r_0, it can be easily seen that the average fraction of scatterers that require spherical wavefronts is $N_R^{\mathrm{SW}}/N_R = \exp(-\sqrt{r_0/\bar{r}_R})$. The parameter $\bar{r}_R$ denotes the effective Rayleigh distance of an average-size ray's VR, which is given by $\bar{r}_R = 16(\bar{R}^R)^2/\lambda$ with $\bar{R}^R = 1/\lambda^R$ denoting the average radius of the rays' VRs. Note that for an average ray's lifespan 4 times shorter than the largest dimension of the array, i.e., $D_A/\bar{R}^R = 8$, less than 3% of the rays would require spherical wavefronts to be employed. Analogous conclusions apply to the clusters since the radius of the clusters' VR are exponentially distributed as well [4]. However, as clusters' lifepans are larger in average than rays', the fraction of clusters that require spherical wavefronts may be larger.

In order to reduce the computational complexity, the following procedure is used with those scatterers located beyond their effective Rayleigh distance. First, use (5.5),

i.e., the spherical wavefront approach, to calculate the exact distance travelled by the scattered ray only at the centre of the ray's VR. Second, use (5.6), i.e., the plane wavefront approach, to obtain the approximate distance travelled by rays received within the VR. This is in contrast with previous approaches, in which the exact distance in (5.5) was used for all rays, antenna elements and time instants. This method enables to reduce the computational burden of the wavefront computation process by the ratio of the complexity of computing the spherical wavefront to that of the plane one.

5.3   Statistical Properties of the Channel Model

This section studies key statistical properties of the proposed massive MIMO channel model. Although the section focuses on the small-scale properties, some relevant statistical properties of the large-scale fading will be studied as well. As only the cluster-level statistical properties of the channel are studied, it is possible to drop the cluster index m in the following sections when it is not essential for the sake of notation simplicity and readability.

5.3.1   Small-scale fading

5.3.1.1   Distribution of the amplitude of rays

Measurements in [4] indicate that the time of arrival t_n, with $n = 1, 2, ..., N$, of rays within a cluster can be modeled as i.i.d. random variables uniformly distributed over the interval $(0, T_C]$. The cluster and rays within it remain visible over periods of time denoted as T_C and T_n^R, respectively. The rays' lifetimes T_n^R can be modeled as i.i.d. exponential random variables of equal rate $\lambda^R = \lambda_n^R$ as indicated in [4]. Thus, the PDF of the amplitude of the rays can be obtained using the theory of transformation

of random variables as

$$p_{g_n(t)}(x) = (1 - p_v)\,\delta(x) + p_v\left(\frac{r}{\pi\sqrt{c_n x - x^2}} + (1-r)\delta(x - c_n)\right) \tag{5.11}$$

for $0 \le x \le c_n$ and zero otherwise. The term $p_v = (\lambda^R T_C)^{-1}$ denotes the probability of a ray being visible at any time t of the cluster's lifetime. Hence, the first term $(1 - p_v)$ in (5.11) denotes the probability of the amplitude of the ray being zero, i.e., scatterer not visible. The second term corresponds to the transition period of (dis)appearance and the third to the period of maximum amplitude c_n. Note that (5.11) is approximately time invariant in $(\lambda^R)^{-1} < t \le T_C - (\lambda^R)^{-1}$ and is time dependent outside this interval. As the average ray's lifetime of a ray is much smaller than that of a cluster [4], i.e., $T_C \lambda^R \gg 1$, the distribution can be approximated by (5.11) and $g_n(t)$ can be considered as a first-order stationary process.

The PDF of the amplitude of the rays in the spatial domain is given by

$$p_{g_n(\boldsymbol{r}^R)}(x) = \;\; (1 - p_v)\,\delta(x) + p_v\frac{\left(2\pi r_0 + r\arccos(1 - 2x)\right)^2}{2\pi^2\sqrt{c_n x - x^2}} + p_v(1 - r)\delta(x - c_n)$$
$$\tag{5.12}$$

where the probability of a ray being visible at any location is $p_v = 4\pi(\bar{R}^R)^3/(L'_x L'_y L'_z)$. The parameters L'_x, L'_y, and L'_z denote the x, y, and z dimensions, respectively, of a region containing the large array where the rays' VRs are randomly generated according to a uniform distribution.

5.3.1.2   Distribution of the envelope

Next, we will study the effects of the ray-level gain on the distribution of the cluster-level envelope process $\Xi = |h_{m,qp}(t)|$ in (5.2) only in the temporal domain as closed-form expressions can be derived. The analysis in the spatial domain leads to closed-form expressions only in the case of ULAs, but it is more complex for 3D antenna arrays of arbitrary shape. The distribution of Ξ for a fixed time instant t is given by

(see Appendix C)

$$p_\Xi(z) = (2\pi)^2 z \int_0^\infty \exp\left\{ r N_a \, {}_2F_3\left(\frac{1}{4}, \frac{3}{4}; \frac{1}{2}, 1, 1; -(c\pi x)^2\right) \right\}$$

$$\times \exp\left\{ N_a \left[J_0(2\pi c x)(1 - r) - 1 \right] \right\} J_0(2\pi z x) x \, \mathrm{d}x \qquad (5.13)$$

for $z > 0$, with ${}_2F_3(\cdot; \cdot; \cdot)$ denoting the generalized hypergeometric series of order 2, 3 [124] and N_a the average number of active rays within the cluster at any time instant. Note that all the rays are assumed to have the same maximum amplitude $c = c_n$ in (5.13). For large values of N_a, the integrand of the previous expression decreases very rapidly. Thus, approximating the exponent by a third-order Taylor polynomial at $x = 0$, $p_\Xi(z)$ is approximately

$$p_\Xi(z) \approx (2\pi)^2 z \int_0^\infty \exp\left[-N_a (c\pi x)^2 \left(1 - \frac{5}{8}r\right) \right] J_0(2\pi z x) x \, \mathrm{d}x. \qquad (5.14)$$

Let σ be the total received power and the maximum amplitude of all rays is $c = \sigma \left[\frac{N_a}{2}(1 - \frac{5}{8}r) \right]^{-\frac{1}{2}}$. Finally, the previous integral can be solved using [124, Equation (6.631.4)] as

$$p_\Xi(z) \approx \frac{z}{\sigma^2} \exp\left(-\frac{z^2}{2\sigma}\right) \qquad (5.15)$$

for $z > 0$ and zero otherwise. That is, the envelope is approximately Rayleigh distributed. Note that the maximum amplitude of the rays $c = \sigma \left[\frac{N_a}{2}(1 - \frac{5}{8}r) \right]^{-\frac{1}{2}}$ depends on the average number of rays and the transition parameter r. The dependence on r compensates the effective reduction of amplitude caused by the taper. Also, note that the rays' lifetimes have no effect on the distribution of the envelope as long as the average number of rays N_a remains constant over the cluster's lifetime. In the spatial domain, the analysis is analogous by plugging (5.12) instead of (5.11) into (C.1). Unlike in the temporal analysis, no closed-form solution has been found to such distribution for the 3D spatial ray gain.

5.3.1.3   Temporal autocorrelation function (ACF)

The normalized temporal ACF of the channel impulse response can be defined as $\rho_{qp}(t_1, t_2) = \mathbb{E}[H_{qp}(t_1, f)H_{qp}^*(t_2, f)]/\mathbb{E}[|H_{qp}(t, f)|^2]$, where

$$
\begin{aligned}
\mathbb{E}[H_{qp}(t_1, f)H_{qp}^*(t_2, f)] = \sum_{m=1}^{C} \sum_{m'=1}^{C} \sum_{n=1}^{N} \sum_{n'=1}^{N} & a_m a_{m'}^* \\
& \times \mathbb{E}[g_{mn,qp}(t_1 - t_{mn})g_{m'n',qp}(t_2 - t_{m'n'})] \\
& \times \mathbb{E}[e^{jk_0[D_{mn,qp}(t_1) - D_{m'n',qp}(t_2)]}]\mathbb{E}[e^{j(\theta_{mn} - \theta_{m'n'})}]. \quad (5.16)
\end{aligned}
$$

Since $\mathbb{E}[e^{j(\theta_{mn} - \theta_{m'n'})}] = 1$ for $m = m'$ and $n = n'$ and is zero otherwise, then

$$
\mathbb{E}[H_{qp}(t_1, f)H_{qp}^*(t_2, f)] = \sum_{m=1}^{C} |a_m|^2 \rho_{m,qp}(t_1, t_2) \quad (5.17)
$$

with

$$
\rho_{m,qp}(t_1, t_2) = \sum_{n=1}^{N} \mathbb{E}[g_{mn,qp}(t_1 - t_{mn})g_{mn,qp}(t_2 - t_{mn}))]\mathbb{E}[e^{jk_0[D_{mn,qp}(t_1) - D_{mn,qp}(t_2)]}]. \quad (5.18)
$$

That is, the total ACF is a weighed sum of the cluster-level ACFs. The total received power can be obtained as $\mathbb{E}[|H_{qp}(t, f)|^2] = \sum_{m=1}^{C} |a_m|^2 \sum_{n=1}^{N} \mathbb{E}[|g_{mn,qp}(t - t_{mn})|^2]]$, where the received power corresponding to a single ray is given by $P_R = \mathbb{E}[|g_{mn,qp}(t - t_{mn})|^2]] = c^2 \left(1 - \frac{5r}{8}\right) T^R / T_C$ for rays of constant lifetime $T_n^R = T^R$ and $P_R = c^2(1 - \frac{3}{4}r)/(T_C \lambda^R)$ when T_n^R are modeled as exponential random variables of rate λ^R. In the calculation of P_R, the boundary effects caused at the extremes of the cluster's lifetime have been neglected.

Due to the complexity and lack of closed-form expressions of the ray-level gain ACF when T_n^R are random variables, we will derive the ACF for a constant lifetime and study its impact on the ACF of the channel. The ACF considering i.i.d. exponentially distributed rays' lifetimes will be studied numerically in Section 5.4. For constant T^R, the ACF of the ray gain can be obtained as $\rho_{g_n g_n}(t_1, t_2) = \mathbb{E}[g_{n,qp}(t_1 - t_n)g_{n,qp}(t_2 - t_n)]/\mathbb{E}[|g_{n,qp}(t - t_n)|^2]]$, where we have dropped the cluster index m for clarity. Thus,

$$\rho_{g_n g_n}(\tau') =$$

$$
\begin{cases}
\frac{1}{8-5r}\left[8-6r-4\tau'+(r-2\tau')\cos\left(\frac{2\pi}{r}\tau'\right)+\frac{3r}{\pi}\sin\left(\frac{2\pi}{r}\tau'\right)\right] & 0 < \tau' \leq r/2 \\[2mm]
\frac{1}{1-\frac{5}{8}r}\left[1-\frac{1}{2}r-\tau'\right] & r/2 \leq \tau' \leq \bar{r} \\[2mm]
\frac{1}{8-5r}\left[6\tau''+2r+[\tau''+r]\cos\left(\frac{2\pi}{r}\tau''\right)-\frac{3r}{2\pi}\sin\left(\frac{2\pi}{r}\tau''\right)\right] & \bar{r} \leq \tau' \leq (1-\frac{r}{2}) \\[2mm]
\frac{1}{8-5r}\left[-\tau''\left[2+\cos\left(\frac{2\pi}{r}\tau''\right)\right]+\frac{3r}{2\pi}\sin\left(\frac{2\pi}{r}\tau''\right)\right] & (1-r/2) \leq \tau' \leq 1
\end{cases}
\tag{5.19}
$$

and zero otherwise. To simplify notation, we have used $\tau' = |t_2-t_1|(T^R)^{-1}$, $\tau'' = \tau'-1$, and $\bar{r} = 1-r$. Equation (5.19) is valid only for $0 \leq r \leq 2/3$. For $2/3 < r \leq 1$ the ACF is obtained as $\rho_{g_n g_n}(\tau) =$

$$
\begin{cases}
\frac{1}{8-5r}\left[8-6r-4\tau'+(r-2\tau')\cos\left(\frac{2\pi}{r}\tau'\right)+\frac{3r}{\pi}\sin\left(\frac{2\pi}{r}\tau'\right]\right] & 0 < \tau' \leq \bar{r} \\[2mm]
\frac{1}{8-5r}\left[4\bar{r}-2\tau''+(\tau''+r)\cos\left(\frac{2\pi}{r}\tau''\right)\right. & \\
\left.\quad -\frac{3}{2\pi}r\sin\left(\frac{2\pi\tau''}{r}\right)+(r-2\tau')\cos\left(\frac{2\pi\tau'}{r}\right)+\frac{3r}{\pi}\sin\left(\frac{2\pi\tau'}{r}\right)\right] & \bar{r} \leq \tau' \leq \frac{r}{2} \\[2mm]
\frac{1}{8-5r}\left[-6\tau''+2r+(\tau''+r)\cos\left(\frac{2\pi}{r}\tau''\right)-\frac{3}{2\pi}r\sin\left(\frac{2\pi}{r}\tau''\right)\right] & \frac{r}{2} \leq \tau' \leq 1-\frac{r}{2} \\[2mm]
\frac{1}{8-5r}\left[-\tau''(\cos\left(\frac{2\pi}{r}\tau''\right)+2)+\frac{3r}{2\pi}\sin\left(\frac{2\pi}{r}\tau''\right)\right] & (1-\frac{r}{2}) \leq \tau' \leq 1.
\end{cases}
\tag{5.20}
$$

As we have shown in (5.11), the ray gain is a first-order stationary process in the interval $T^R/2 < t < T_C - T^R/2$. As the ACFs in (5.19) and (5.20) depend only on the time difference $|t_2-t_1|$ for $T^R/2 < t_i < T_s - T^R/2$ with $i = 1,2$, the process is also second-order stationary and hence WSS for the majority of the cluster's lifetime. Assuming that the amplitudes of the rays are constant $c_n = \sigma[\frac{N_a}{2}(1-\frac{5}{8}r)]^{-1/2}$, the cluster-level temporal ACF is given by

$$\rho_{qp}(t_1,t_2) = \frac{1}{N}\sum_{n=1}^{N}\rho_{g_n g_n}(t_1,t_2)\mathbb{E}[e^{jk_0[D_{n,qp}(t_1)-D_{n,qp}(t_2)]}]. \tag{5.21}$$

When all the rays' lifetimes are equal or they are equally i.i.d. random variables, this ACF can be separated as $\rho_{qp}(t_1, t_2) = \rho_{g_n g_n}(t_1, t_2) \cdot \rho_{S,qp}(t_1, t_2)$, where

$$\rho_{S,qp}(t_1, t_2) = \frac{1}{N} \sum_{n=1}^{N} \mathbb{E}[e^{jk_0[D_{n,qp}(t_1) - D_{n,qp}(t_2)]}] \tag{5.22}$$

is defined as the ACF of the cluster without ray-level evolution process. The rays' gains introduce several effects in the total ACF that are worth studying. First, as the ACF of $g_n(t)$ is a decreasing function of the time difference, the total ACF is tapered off. This effect is more important when the rays' lifetimes are of the same order of magnitude as the coherence time of the cluster, defined as $\min_{|t_2 - t_1|} [\rho_{qp}(t_1, t_2) < \rho_C]$, with $|\rho_C| \leq 1$. An estimate of the rays' lifetimes guaranteeing that the reduction of the absolute value of the ACF is at most $1/\rho_0$ with $0 < \rho_0 \leq 1$ for a time difference $|t_2 - t_1|$ can be calculated as

$$T^R = \frac{1 - \left(\frac{1}{2}r + \rho_0 \left(1 + \frac{5}{8}r\right)\right)}{T_C}. \tag{5.23}$$

This expression is valid for $r < 2/3$ and $rT^R/2 < T_C$, which are reasonable conditions as rays' lifetimes are shorter than clusters' and we assume a short (dis)appearance times.

The ACF derived above considered a constant ray's lifetime T^R for all rays. However, when T_n^R are i.i.d. random variables, the law of total probabilities can be used as

$$\rho_{g_n g_n}(\tau)(x) = \int_0^{\infty} \rho_{g_n g_n}(\tau)(x \mid T^R = y) p_{T^R}(y) \, \mathrm{d}y \tag{5.24}$$

where $\rho_{g_n g_n}(\tau)(x \mid T^R = y)$ denotes the ACF of the n-th ray's gain when its lifetime is a constant value $T^R = y$ as given by (5.19) and (5.20). For exponentially distributed i.i.d. random rays' lifetimes [4], the closed-form solution to (5.24) is $\rho_{g_n g_n}(\tau) = \exp\left(-\tau/\lambda^R\right)$, which is valid only for $r = 0$. Although we have not found a general closed-form solution to the integral above valid for any value of r, the following approximation

$$\hat{\rho}_{g_n g_n}(\tau) = e^{-\lambda^R (1 + 3r/8) \tau} \tag{5.25}$$

has been found to fit very well the results obtained using (5.24) for $0 < r < 1$. Thus, it can be seen that the exponentially distributed i.i.d. rays' lifetimes transform a linear decay into an exponential one. In addition, whereas the average ray's lifetime has a large effect on the total ACF, taper parameter has a relatively small impact on it.

5.3.1.4 Doppler power spectral density (PSD)

The Doppler spectrum of the channel can be obtained as the Fourier transformation of the ACF of the CIR with respect to the time difference. As we have shown in (5.22), the cluster-level ACF is separable as a product of two different ACFs. By the convolution property of the Fourier transform, the cluster-level Doppler PSD can be obtained as

$$S_{qp}(\nu) = S_{g_n}(\nu) \otimes S_{S,qp}(\nu) \tag{5.26}$$

where ν denotes the Doppler frequency, $\otimes$ the convolution operation, $S_{g_n}(\nu)$ the Doppler PSD of the n-th ray's gain and $S_{S,qp}(\nu)$ that of a cluster without ray-level evolution process. Due to the convolution, the cluster-level Doppler PSD is spread. For a constant value of T^R, the Doppler PSD $S_{g_n}(\nu)$ is given by the Fourier transform of the ACF in (5.19) with respect to τ as

$$\begin{aligned} S_{g_n}(\nu') = \frac{(T^R)^2}{8\pi^2 \nu'^2 (\nu'^2 r^2 - 1)(\nu'^2 r^2 + 1)} &\Big[2 \left(1 + \cos \left(r\pi\nu' \right) \right) \\ &- \cos \left(2\pi\nu' \right) - \cos \left(2\pi\nu'(r-1) \right) - 2\cos \left(r\pi\nu'(r-2) \right) \Big] \end{aligned} \tag{5.27}$$

where $\nu' = \nu T^R$. Clearly, the rays' lifetimes and taper parameter determine the spectral characteristics of the ray-level evolution process. Whereas T^R is a scale parameter that controls the spread of the Doppler spectrum, r determines both the spread and level of spectral leakage. The average Doppler shift and spread can be calculated using the first and second derivative of the ACF with respect to the time difference $\dot{\rho}(0)$ and $\ddot{\rho}(0)$, respectively, as [12]

$$B_{qp}^{(1)}(t) = \frac{1}{2\pi j} \cdot \frac{\dot{\rho}_{qp}(t,t)}{\rho_{qp}(t,t)} = \frac{1}{2\pi j} \frac{\dot{\rho}_{S,qp}(t,t)}{\rho_{S,qp}(t,t)} \tag{5.28}$$

$$B_{qp}^{(2)}(t) = \frac{1}{2\pi}\sqrt{\left(\frac{\dot{\rho}_{qp}(t,t)}{\rho_{qp}(t,t)}\right)^2 - \frac{\ddot{\rho}_{qp}(t,t)}{\rho_{qp}(t,t)}}$$

$$= \frac{1}{2\pi}\sqrt{\left(\frac{\dot{\rho}_{S,qp}(t,t)}{\rho_{S,qp}(t,t)}\right)^2 - \left(\frac{\ddot{\rho}_{S,qp}(t,t)}{\rho_{S,qp}(t,t)} - \frac{4\pi^2}{r(T^R)^2}\right)} \tag{5.29}$$

where we have used the relationships $\dot{\rho}_{g_n}(t,t) = 0$ and $\ddot{\rho}_{g_n}(t,t) = \frac{4\pi^2}{r(T^R)^2}$. Equation (5.29) is not defined for $r = 0$ as the derivative of the ACF in (5.19) does not exist at $\tau = 0$. The average Doppler shift is not affected by the rays' gains, but the Doppler spread always increases. In particular, when rays' lifetimes are similar or greater than the reciprocal of the maximum Doppler frequency, the impact on the Doppler spread of the channel will be higher.

5.3.1.5 Spatial cross-correlation function (S-CCF)

The S-CCF of the channel can be defined as the correlation between a signal transmitted from the antenna element A_p^T and received by A_q^R and that transmitted from $A_{p'}^T$ and received by $A_{q'}^R$ at time t and carrier frequency f. Thus, it can expressed as $\rho_{qp,q'p'} = \mathbb{E}[H_{qp}(t,f)H_{q'p'}^*(t,f)]/\mathbb{E}[|H_{qp}(t,f)|^2]$. Similar to the derivation of the ACF, as $\mathbb{E}[e^{j(\theta_{mn} - \theta_{m'n'})}] = 1$ for $m = m'$ and $n = n'$ and is zero otherwise, then

$$\mathbb{E}[H_{qp}(t,f)H_{q'p'}^*(t,f)] = \sum_{m=1}^{C}|a_m|^2\sum_{n=1}^{N_m}\mathbb{E}[g_{mn,qp}(t - t_{gn})g_{mn,q'p'}(t - t_{mn})]$$
$$\times \mathbb{E}[e^{jk_0[D_{mn,qp}(t) - D_{mn,q'p'}(t)]}]. \tag{5.30}$$

The S-CCF of the ray-level evolution process can analogously be defined $\rho_{S,qp} = \mathbb{E}[g_{mn,qp}(t - t_{mn})g_{mn,q'p'}(t - t_{mn})]/\mathbb{E}[|g_{mn,qp}(t - t_{mn})|^2]]$. One important difference in the derivation of the ACF and S-CCF lies on the number of dimensions involved. Whereas the ACF is limited to a single dimension, i.e., time, a larger number of dimensions is required for antenna arrays at both sides of the communication link. Single or multiple-dimensional antenna arrangements usually lead to complex expressions of the S-CCF and closed-form expressions are usually not achievable. In the case of ULAs with antenna spacing at the transmit- and receive-sides δ_T and δ_R, respectively,

and multi-bounce propagation (where independence between the transmit-side and receive-side is usually assumed), the S-CCF of the ray-level process can be expressed the product of the transmit-side and receive-side S-CCFs. In these conditions, the S-CCFs of the ray-level evolution process can be easily obtained by using (5.19) and replacing $|t_2 - t_1|$ by $|\delta_R(q - q')|$. Due to the limitations described above, we will numerically study the S-CCF in Section 5.4.

5.3.1.6   Frequency correlation function (FCF)

The normalized FCF is $\rho_{qp}(f_1, f_2) = \mathbb{E}[H_{qp}(t, f_1)H_{qp}^*(t, f_2)]/\mathbb{E}[|H_{qp}(t, f)|^2]$, where

$$\mathbb{E}[H_{qp}(t, f_1)H_{qp}^*(t, f_2)]] = P_R \sum_{m=1}^{C} |a_m|^2 \sum_{n=1}^{N} e^{-j2\pi(f_1 - f_2)\tau_{mn,qp}(t)}. \qquad (5.31)$$

As delays corresponding to individual rays depend on the antenna elements of the large array and time instant considered, the FCF is STV. As indicated by [123], the relatively small variation of the delays over the array enables to use a linear approximation of $\tau_{mn,qp}(t)$ as

$$\tau_{mn,qp}(t) \approx \tau_{0,mn} - \tau_q \cos\psi_{mn}^R - \tau_v^T(t)\cos\xi_{mn}^T - \tau_v^R(t)\cos\xi_{mn}^R \qquad (5.32)$$

where $\tau_{0,mn}$ is the reference delay of the n-th ray in the mth cluster from the transmitting to the receiving arrays centres, $\tau_v^T(t) = v^T t/c_0$ and $\tau_v^R(t) = v^R t/c_0$ denote the extra propagation delay induced by the motion of the Tx and Rx, respectively, and $\tau_q = \delta_q/c_0$ denotes the propagation delay from the centre of the receiving large array to the q-th antenna element. Therefore, the terms $\tau_q \cos\psi_n^R$, $\tau_v^T(t)\cos\xi_n^T$, and $\tau_v^R(t)\cos\xi_n^R$ in (5.32) model the relative delay experienced by the signal radiated from A_p^T and received by A_q^R at time instant t with respect to $\tau_{0,mn}$. Note that previous models assumed a constant delay that is independent of the time instant and antenna element as $\tau_{qp,mn}(t) = \tau_{0,mn}$, since δ_p/c_0, δ_q/c_0, $v^T t/c_0$, and $v^R t/c_0$ are small in conventional WSS MIMO systems.

5.3.2 Large-scale fading

The ray-level evolution process may be physically interpreted as shadowing of individual rays produced by objects in the environment. Thus, the cluster-level large-scale fading is implicitly captured in this model due to the ray-level evolution process.

5.3.2.1 Distribution of the local-average received power

Even though the cluster-level average received power is a constant value $P_C = Nc^2(1-5/8r)T^R$, the cluster-level local-average received power is an STV random process describing the cluster-level shadow fading [125]. A sample function of the average received power can be obtained through the expectation of the instantaneous received power conditioned to a set of fixed parameters of the ray-level evolution process, i.e., conditioned to a fixed large-scale environment, as

$$\mathbb{E}\left[H_{qp}(t,f)H_{qp}(t,f)^* \mid g_{mn,qp}(t-t_{mn})\right] = \sum_{m=1}^{C}|a_m|^2\sum_{n=1}^{N_m}g_{mn,qp}^2(t-t_{mn}). \quad (5.33)$$

Thus, we can model the cluster-level large-scale fading by extending the formulation of the average received power proposed in [126] and defining the process $\gamma_{m,qp}(t)$ as [125]

$$\gamma_{m,qp}(t) = \sum_{n=1}^{N_m}g_{mn,qp}^2(t-t_{mn}). \quad (5.34)$$

Although large-scale fading is usually modeled employing a Lognormal distribution [12], the sum of Lognormal random variables is not Lognormal distributed [127], [128], which hinders the modelling of the total large-scale fading. Thus, Gamma distributions have been proposed as a convenient alternative to the Lognormal distribution for this purpose [129]. Let $c_{mn}^2 \sim \Gamma(k_{mn}, \theta)$, with $m = 1 \ldots C$ and $n = 1 \ldots N_m$, be a collection of i.i.d. Gamma-distributed random variables denoting the maximum squared amplitude of N_m rays in C clusters. Note that the collection shares the same scale

parameter θ, hence we can use the summation property of i.i.d. Gamma random variables, i.e., $\sum_{n=1}^{N} c_{mn}^2 \sim \Gamma(\sum_{n=1}^{N} k_{mn}, \theta)$. For a sufficiently large average number of visible rays within a cluster, the resulting process modelling the cluster-level local-average received power is approximately Gamma-distributed as $\gamma_{m,qp}(t) \sim \Gamma(\sum_{n=1}^{N} k_{mn}, \theta)$.

5.3.2.2   ACF of cluster-level large-scale fading

The ACF of the process $\gamma_{m,qp}(t)$ is obtained as

$$\rho_{\gamma_m \gamma_m}(t_1, t_2) = \sum_{n=1}^{N_m} \sum_{n'=1}^{N_m} \mathbb{E}\left[g_{mn,qp}^2(t_1 - t_{mn}) g_{mn',qp}^2(t_2 - t_{mn'})\right] \qquad (5.35)$$

which can be analogously computed to the ACF of the ray gain in (5.19) and it is omitted here for brevity. As an example, closed-form expressions of this ACF can be found for rapid (dis)appearance of rays ($r = 0$) as $\lambda^R \exp\left(-\tau/\lambda^R\right)$ with $\tau = |t_2 - t_1|$. This ACF depends only on time difference $|t_2 - t_1|$ and has a form similar to that in (5.19) and (5.20), being a smoothly decreasing function of the time difference. Traditionally, the exponential profile has been widely used to fit measurement results of the ACF of the large-scale fading [12].

5.3.3   Distribution of the number of rays and clusters

As in previous sections, let us assume that the appearance times of N rays within a cluster are modeled as i.i.d. random variables uniformly distributed over the cluster's lifetime as $t_n \sim \mathcal{U}(0, T_C)$, with $n = 1 \ldots N$. In addition, rays' lifetimes T_n^R are modeled as i.i.d. exponentially distributed random variables with rate λ^R. The total number of visible rays in the cluster at time t is a random variable which can be expressed as

$$n_R(t) = \sum_{n=1}^{N} \mathbb{1}_{t_n < t < t_n + T_n^R}. \qquad (5.36)$$

The term $\mathbb{1}_{t_n < t < t_n + T_n^R}$ above denotes the indicator function, i.e., it is unity when $t_n < t < t_n + T_n^R$ and zero otherwise. For a given time instant t and a constant

$T^R = T_n^R$, the event $t_n < t < t_n + T^R$ is a Bernoulli trial with probability of success given by

$$p(t) = \begin{cases} \frac{1}{T_C} \cdot \left(t + \frac{1}{2}T^R\right) & -\frac{T^R}{2} < t \le \frac{T^R}{2} \\ \frac{T^R}{T_C} & \frac{T^R}{2} < t \le T_C - \frac{T^R}{2} \\ \frac{1}{T_C}\left(T_C - t + \frac{1}{2}T^R\right) & T_C - \frac{T^R}{2} < t < T_C + \frac{T^R}{2} \end{cases} \tag{5.37}$$

where $T^R < T_C$ was assumed. Thus, the probability of a ray being visible is approximately a constant $p \approx T^R/T_C$ over the majority of the cluster's lifetime as long as $T^R \ll T_C$. However, as T_n^R are i.i.d. exponentially distributed random variables with rate λ^R, $p(t)$ can be computed using the law of total probabilities and is given by

$$p(t) = \begin{cases} \frac{1}{2}\frac{1}{\lambda^R T_C} \cdot e^{2\lambda^R t}\left(1 - e^{-2\lambda^R T_C}\right) & t \le 0 \\ \frac{1}{\lambda^R T_C} \cdot \left(1 - \frac{1}{2}\left[e^{-2\lambda^R t} + e^{-2\lambda^R(T_C - t)}\right]\right) & 0 < t \le T_C \\ \frac{1}{2}\frac{1}{\lambda^R T_C} \cdot \left(e^{-2\lambda^R(T_C - t)} - e^{-2\lambda^R t}\right) & T_C \le t. \end{cases} \tag{5.38}$$

The number of visible rays at any time instant $n_R(t)$ is the sum of N Bernoulli trials, so it is Binomial distributed with parameters N and time-varying probability $p(t)$ as given by (5.38). However, as recent measurements [4] showed that rays' lifetimes are usually much shorter than clusters', e.g., $\lambda^R T_C \approx 10$, from (5.38) the probability $p(t)$ can be approximated as $p = (\lambda^R T_C)^{-1}$. Then, the number of visible rays is Binomial distributed as $n_R(t) \sim \mathcal{B}\left(N, (\lambda^R T_C)^{-1}\right)$ approximately in the interval $0 < t < T_C$. Thus, the average number of visible rays in a cluster is approximately a constant value $N_R(t) = \mathbb{E}[n_R(t)] = Np(t) \approx N(\lambda^R T_C)^{-1}$.

When the cluster (dis)appears, the number of rays increases (decreases) exponentially and the raising (decay) time from (to) the $L\%$ to (from) the $(1 - L)\%$ of the total number of rays is

$$\Delta t_{L\%} = -\frac{1}{\lambda^R} \cdot \log\left(\frac{1}{100} \cdot \frac{2L}{1 - e^{-2\lambda^R T_C}}\right) \tag{5.39}$$

for $0 < L < 50\%$. Examples of transition periods are $\Delta t_{10\%} \approx 1.6(\lambda^R)^{-1}$ $\Delta t_{1\%} \approx$

$3.9(\lambda^R)^{-1}$, where we have assumed $\lambda^R T_C \gg 1$. The raising (decay) time $\Delta t_{L\%}$ guarantees a smooth transition of the cluster's power when it (dis)appears without adding additional elements to the model. In addition, as $\lambda^R T_C \gg 1$ [4], the law of rare events allows us to approximate $n_R(t)$ as a Poisson random variable with rate parameter $N(\lambda^R T_C)^{-1}$, as proposed by previous non-stationary massive MIMO channel models [13], [88], [89].

Using an analogous argument, the number of visible clusters at any time instant $n_C(t)$ is Poisson distributed with rate parameter λ^C. However, measurements [16] reported that the number of clusters at different locations of the array can be accurately modeled by a negative binomial random variable when multiple locations of the MS are considered. This apparent contradiction is solved by noting that a negative binomial distribution can be obtained as a continuous mixture of Poisson and Gamma distributions. Thus, a negative binomial random variable denoted as $x \sim \mathcal{NB}(r, p)$ can be expressed as $x \sim \text{Poisson}(\lambda)$ where the rate parameter λ is also a Gamma-distributed random variable $\lambda \sim \Gamma(k, \theta)$, with $k = r$ and $\theta = \frac{p}{1-p}$.

Thus, let λ_l^C, $l = 1, 2, ..., L$, be i.i.d. Gamma-distributed random rates corresponding to the Poisson-distributed number of visible clusters at any time instant for L different locations of the MS. Using the scaling property of the Gamma distribution and assuming that the L random rates are i.i.d. as $\lambda_l^C \sim \Gamma(k, \theta T_S / C)$ with C the total number of clusters, the aggregated number of visible clusters follows a negative binomial distribution, i.e., $n_C(t) \sim \text{NB}(r, p)$ with parameters $r = k$ and $p = \theta / (\theta + 1)$. The average of the aggregated number of visible clusters is given by $N_C = \mathbb{E}[n_C(t)] = \mathbb{E}[\lambda_l^C C / T_S] = k\theta$. Finally, using measured parameters p and r of the negative binomial distribution as given in [16], the random (dis)appearance rates can be modeled as i.i.d. random variables distributed as $\lambda_l^C \sim \Gamma(r, \frac{p}{1-p} \frac{T_S}{C})$. From the physical point of view, it is reasonable to expect different average numbers of visible clusters at different locations of the MS. This assumption is less restrictive than the opposite, i.e., that of spatially-invariant average number of visible clusters. The previous results focused on the temporal characteristics of the number of visible

rays/clusters can be analogously extended to the spatial (array) domain and they are ommited here for brevity.

5.4   Results and Analysis

As the main contribution of this work is the ray-level spatial-temporal evolution process, in this section we we will numerically study the effects produced by the ray-level gain on the statistical properties of the channel model. The following theoretical results were obtained by numerical evaluation of the expressions derived in section 5.3. For the simulations, we used the recent massive MIMO channel measurements reported in [4] to generate the channel parameters, e.g., ray-level visibility characteristics, angles, and delays, and computed 10^3 realizations of the CTF in (5.3). The measurements [4] were conducted in a subway station, employing a virtual 256-element rectangular antenna array at the transmitting side and a single antenna element at the receiving side. The sounding signal was centred at 6 GHz and spanned 100 MHz. Advanced clustering and tracking algorithms enabled the authors to obtain both cluster- and ray-level parameters and their evolution over the array, e.g., ray (dis)appearance rates. Although both Tx and Rx remained static due to the limitations of the virtual array technique, we will assume the Tx moves at a constant speed in order to study the ACF and Doppler spectrum predicted by the channel model.

5.4.1   Envelope distribution

First, we will study the effect of the ray-level gain and its parameters on the distribution of the envelope as defined in Section 5.3.1.2. In Figure 5.3, the distribution $p_\Xi(z)$ is depicted for short and long (dis)appearance times, i.e., for values of the taper parameter $r = 0$ and $r = 1$, respectively. For reference, the Rayleigh distribution of unit variance is also shown. Both theoretical and simulated distributions resemble a Rayleigh distribution almost independently of r. However, note that the maximum
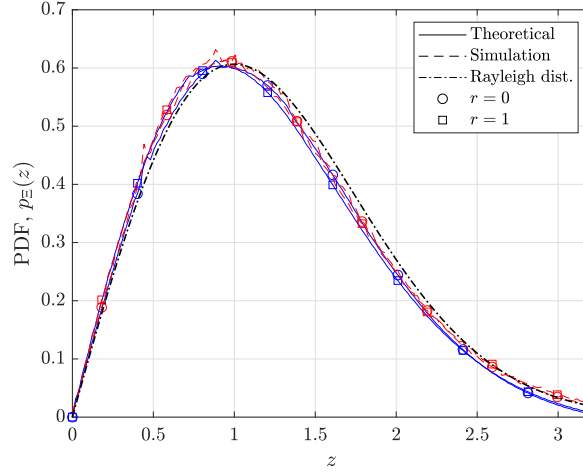
FIGURE 5.3: Comparison of the theoretical and simulated distribution of the envelope for rapid and slow (dis) appearance times, i.e., $r = 0$ and $r = 1$, respectively. The Rayleigh distribution of unit variance is also shown for comparison ($\sigma = 1$, $N_a = 10$).

amplitude of the rays is scaled by r as $c = \sigma \left[\frac{N_a}{2} (1 - \frac{5}{8}r) \right]^{-\frac{1}{2}}$ to compensate the reduction of amplitude caused by the taper. This is, the contribution of every ray to the overall received signal is uneven as the amplitude of every ray is weighted by the ray gain. In addition, it can be seen that the average number of visible rays required to achieve a given level of accuracy approximating a Rayleigh distribution is larger than that of existing models due to the random nature of the number of rays.

5.4.2 Temporal autocorrelation function (ACF)

In Figure 5.4, we present a comparison of the theoretical and simulated absolute values of the array-variant cluster-level ACFs with and without ray-level evolution for a maximum Doppler frequency of $\nu_{\max}^T = 24$ Hz. These results show that the ray-level evolution process can have a strong impact on the temporal correlation and hence the coherence time. As the average lifetime of rays is shorter than the cluster's coherence time, the ray-level evolution process significantly reduces the total cluster-level ACF. For instance, for a correlation level of 0.5, the coherence time becomes $1/\nu_{\max}^T$ seconds shorter in Figure 5.4, which represents a reduction of the 66 % of the coherence time of the cluster without considering ray-level evolution.
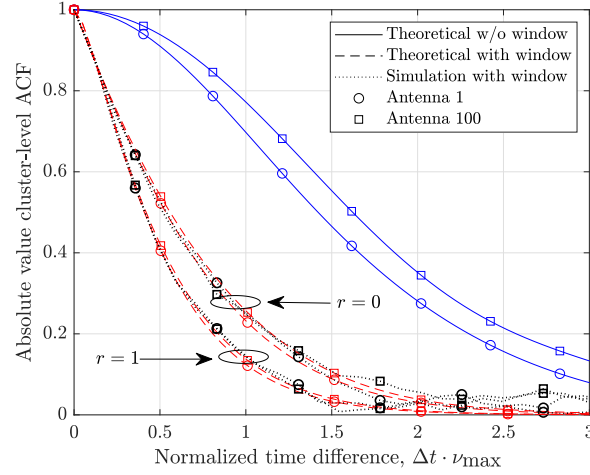
FIGURE 5.4: Comparison of the absolute values of the theoretical and simulated ACF with and without ray-level evolution for different values of the temporal taper parameter r ($N_a = 10$, $N_T = 256$, $N_R = 1$, $\alpha^T = 45°$, $\beta^T = 0°$, $\boldsymbol{s}_c^T = (4, 4, 0)$ m, $\phi_\mu^T = 45°$, $\phi_\sigma^T = 4°$, $\theta_\mu^T = 0°$, $\theta_\sigma^T = 0.5°$, $\alpha_v^T = 135°$, $\beta_v^T = 90°$, $\nu_{\max} = 24$ Hz, $\nu_{\max}^T \cdot T^R = 0.7$).

The impact of the (dis)appearance times on the ACF is less significant than that of the rays' lifetimes, but its effects are not negligible. Long (dis)appearance times ($r \approx 1$) reduce the temporal ACF more than short ones ($r \approx 0$) because rays' lifetimes are independent of their duration, i.e., T_n^R does not increase with r. If the total lifetime of the ray depended on r, the effect would be the opposite. Note that we have used the spatial rays' lifespans D^R provided in [4] in order to calculate the temporal lifespan as $T^R = D^R/v^T$. In addition, note that the ray-level evolution reduces the differences among ACFs at different locations of the array produced by near-field effects.

5.4.3 Doppler power spectal density (PSD)

In Figure 5.5, a comparison of the theoretical and simulated cluster-level Doppler PSDs is presented. Since the simulted Doppler PSD has been obtained through the Fourier transformation of the corresponding ACF, the effects of the ray-level evolution can be deduced by duality. Thus, a short average lifetime of rays leads to large cluster-level Doppler spreads. In particular, we observe in Figure 5.5 that the cluster-level Doppler spread increases from 75 to 86 Hz on average, which represents a 15% approximately. In addition, shorter (dis)appearance times ($r \approx 0$) spread the Doppler PSD
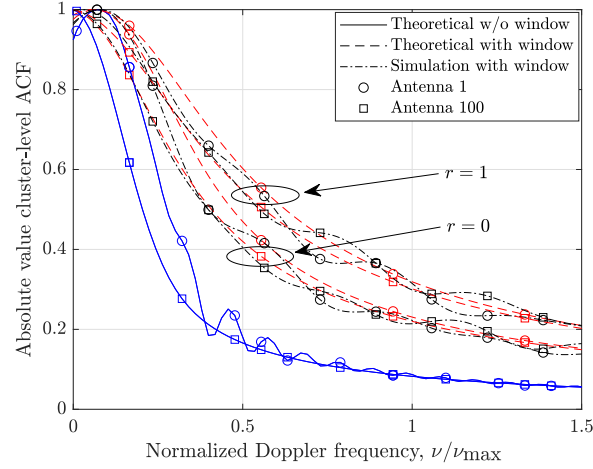
FIGURE 5.5: Comparison of the absolute values of the theoretical and simulated cluster-level Doppler PSD with and without ray-level evolution for different values of the temporal taper parameter r ($N_a = 10$, $N_T = 256$, $N_R = 1$, $\alpha^T = 45°$, $\beta^T = 0°$, $\boldsymbol{s}_c^T = (4, 4, 0)$ m, $\phi_\mu^T = 45°$, $\phi_\sigma^T = 4°$, $\theta_\mu^T = 0°$, $\theta_\sigma^T = 0.5°$, $\alpha_v^T = 135°$, $\beta_v^T = 90°$, $\nu_{\max} = 24$ Hz, $\nu_{\max}^T \cdot T^R = 0.7$).

less than longer ones ($r \approx 1$). As explained above, this effect is due to the independence of the rays' lifetimes on r. Finally, note the differences in the Doppler spectra at different locations of the array that demonstrate the non-stationary properties of the channel in the spatial domain.

5.4.4 Spatial cross correlation function (S-CCF)

In Figure 5.6, the theoretical and simulated absolute values of the cluster-level S-CCFs are compared. The effects of the ray-level gain are similar to those observed above for the ACF. Thus, the small sizes of the rays' VRs tend to reduce the cluster-level antenna correlation. As presented in [4], the average lifespan of rays is one order of magnitude shorter that cluster's. This is specially important for clusters highly concentrated in the angular domain, since they present longer coherence regions. For widespread clusters in the angular domain, the effect of the ray-level evolution process is lower as the S-CCF decays faster. Note also that the effect of the parameter r on the S-CCF is smaller than that observed in the ACF above due to the 2D circular shape of the ray-level spatial VRs.
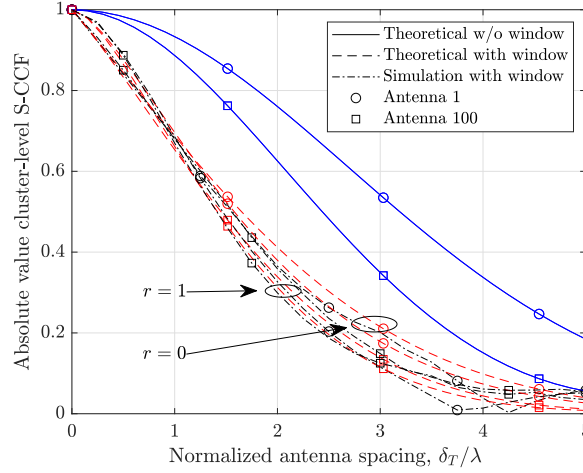
FIGURE 5.6: Comparison of the absolute values of the theoretical and simulated cluster-level S-CCF with and without window ($N_a = 10$, $N_T = 256$, $N_R = 1$, $\alpha^T = 0°$, $\beta^T = 0°$, $\boldsymbol{s}_c^T = (5, 5, 0)$ m, $\phi_\mu^T = 45°$, $\phi_\sigma^T = 4°$, $\theta_\mu^T = 0°$, $\theta_\sigma^T = 6°$, $R^R = 0.15 \, (1.2\lambda)$ m).

5.4.5 Frequency correlation function (FCF)

In Figure 5.7 we present a comparison of the theoretical and simulated absolute values of the cluster-level FCFs. The FCF is unaltered by the ray-level gain as this is independent of the delay domain. However, note that the FCF depends on the antenna element considered as a consequence of the delay drifts and spread, as described in [116]. These effects are more noticeable for values of the delay spread similar to the time it takes a ray to travel across the array, i.e., when $\tau_{\mathrm{rms}} \approx c_0^{-1} \cdot D_A$, with D_A the largest dimension of the array.

5.5 Summary

This chapter presented a novel space-time non-stationary 3D wideband massive MIMO channel model that is able to capture ray-level near-field effects and smooth (dis)appearance recently reported in massive MIMO measurements. Moreover, the impact of the ray-level evolution process on the most important statistical properties of the channel model has been studied and it can be concluded that the cluster-level ACF, Doppler PSD, and S-CCF can be largely affected by the ray's lifespan and smoothness of
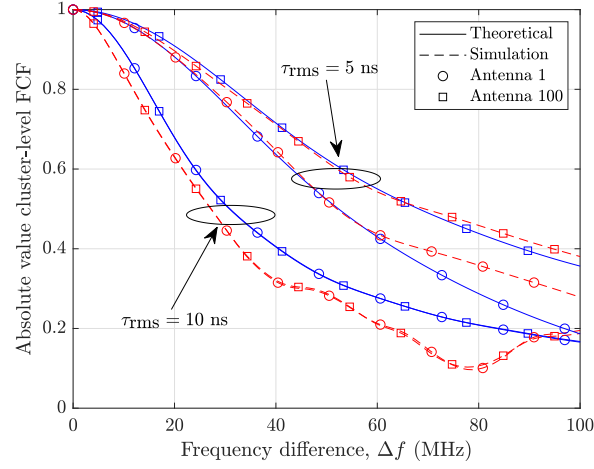
FIGURE 5.7: Comparison of the absolute values of the theoretical and simulated cluster-level FCF for different values of intra-cluster delay spread ($N_a = 10$, $N_T = 256$, $N_R = 1$, $\alpha^T = 45°$, $\beta^T = 0°$, $\boldsymbol{s}_c^T = (4, 4, 0)$ m, $\phi_\mu^T = 45°$, $\phi_\sigma^T = [6\ 50]°$, $\theta_\mu^T = 0°$, $\theta_\sigma^T = [4\ 30]°$).

(dis)appearance. A novel method has been proposed to determine the most adequate wavefront for each cluster and ray. A large percentage of clusters and rays of limited lifespan can still use plane wavefronts and significantly reduce the computational complexity of the channel model.

Chapter 6

Conclusions and Future Work

This dissertation dealt with the modelling of wideband massive MIMO wireless channels under spatial and temporal non-stationary conditions. The comprehensive literature review on both channel measurements and models presented in Chapter 2 has permitted to identify the limitations and major areas of improvement of existing channel models. The study of fundamental aspects of massive MIMO channels in Chapter 3 has been leveraged to propose accurate and efficient channel models for B5G communication systems in Chapters 4 and 5. This concluding chapter summarizes the key findings of this work and provides an outlook on future research directions.

6.1 Summary of Results

In Chapter 3, a transformation method to model STV 2D non-stationary wideband massive MIMO channels has been proposed. This method can be used to obtain the STV joint PDF of the ToA and AoA at any time instant and antenna element of the array from a predefined configuration of the scatterers. In addition, the chapter introduced a simplified channel modelling approach based on STV parameters of the AoA distribution and demonstrated that key statistical properties of massive MIMO channels, such as the STV temporal ACF and Doppler PSD, can be derived in closed

form. As examples of application, multiple array-variant properties of three widely-used GBSMs: the Unified Disk, Ellipse, and Gaussian scattering models, have been studied. Numerical results and simulations of the statistical properties of the three GBSMs have demonstrated a good agreement between the proposed techniques and the spherical wavefront approach. It has been shown that both the means and spreads of the AoA and ToA vary over the array and that the array-varying properties of the FCF of these three GBSMs are caused not only by the disappearance of MPCs, but also by the drift and spread of the ToA over the array.

In Chapter 4, a novel 3D non-stationary wideband geometry-based stochastic theoretical channel model for 5G massive MIMO communication systems has been introduced. The proposed model includes a second-order approximation to the spherical wavefront in space and time domains, i.e., *parabolic wavefront*, that captures near-field effects more efficiently than spherical wavefronts with a negligible reduction in accuracy. In addition, space-time large-scale fading has been modeled by spatial-temporal cluster (re)appearance and shadowing processes. A novel (re)appearance process to model the visibility of clusters with enhanced spatial-temporal consistency have been proposed. Shadowing processes have been used to capture smooth spatial-temporal variations of the clusters' average power. Additionally, a corresponding simulation model has been derived along with a 3D extension of the RSM for parameters computation. Key statistical properties of the proposed model, e.g., the spatial-temporal cross-correlation function, have been derived and analysed. This chapter included numerical and simulation results showing an excellent agreement between the theoretical and simulation models and a validation of the proposed parameter computation method. The accuracy and flexibility of the proposed simulation model have been demonstrated by comparing simulation results and measurements of the RMS DS, slope of cluster power variations, and VRs' size. The relationship between non-stationary properties of the channel, e.g., time- and array-variant ST-CCFs and Doppler frequency drifts, and the distance between the arrays and clusters has been demonstrated.

In Chapter 5, a novel space-time non-stationary 3D wideband massive MIMO channel model has been proposed. The sub-cluster ray-level evolution process introduced can

model the spatial-temporal evolution of individual MPCs or rays, including near-field effects and (dis)appearance, and cluster-level large-scale fading. The evolution process can flexibly control rays' lifespans and smoothness of (dis)appearance in both space and time domains. Key statistical properties of the channel, including the ACF, Doppler PSD, S-CCF, and FCF, have been derived and the impact of the ray-level evolution process on them analysed. The chapter demonstrates the correctness of the derived statistical properties through numerical and simulation results. In addition, it introduces an improved criterion based on the effective Rayleigh distance to determine the most adequate wavefront for each cluster and ray, significantly reducing the need for spherical wavefronts. Existing models can easily use the proposed criterion and make a more efficient use of computation resources. Moreover, a Gamma-Poisson mixture distribution has shown a good accuracy modelling the number of clusters when multiple locations of the MS are considered.

6.2 Future Research Directions

Massive MIMO channel modelling is a vast area of research that is still maturing. Important aspects of this field are under investigation and need significant effort to be considered as solved. The following list includes potential research directions identified by the author:

- The theoretical analysis of massive MIMO channel characteristics presented in Chapter 3 has only considered single-bounce propagation. However, multi-bounce propagation could represent a relevant fraction of the received power in some cases. As the AoD, AoA, and delay cannot uniquely identify a multi-bounce path, additional propagation information is required to overcome this challenge. In addition, an extension of the method that considers the elevation characteristics of the channel may lead to new conclusions about the non-stationary properties of massive MIMO channels.

- The characteristics of VRs such as their 3D shape need further investigation through both measurements and models. As these measurements will require

high spatial sampling rates over long distances, the development of parallel MIMO channel sounders could help accomplish this task in an affordable time. Stochastic geometric shapes may be worth investigating to overcome the over-simple and common circular or spherical shape of VRs. Additionally, it is important to understand the impact of cluster (re)appearance on the performance and accuracy of massive MIMO channel models, particularly at mmWave frequencies where blockage effects are more pronounced.

- The statistical properties of cluster-level large scale fading processes and their relative importance compared to the (dis)appearance of clusters would also be valuable. New channel parameter estimation techniques capable of measuring individual mutipath components and sub-clustering effects are needed. This will allow to study the relationship between the clusters' and rays' lifespans more accurately. The amount of power conveyed by different rays in a cluster will help determine the impact of non-stationary characteristics of the channel on key performance metrics of wireless communication systems.

- Different methodologies to determine the most appropriate wavefront for each ray need to be empirically supported. For that purpose, measurements that capture the proportion of plane and high-order wavefronts in real environments would be required. Moreover, further investigation on the definition of the stationary region of the channel based on the STV PDF of the ToA and AoA would complement existing methods.

- Additional channel measurements and models for mmWave and THz communications using (ultra) massive MIMO are essential. The use of extremely high carrier frequencies, bandwidths and number of antennas will require a deep understanding of the propagation characteristics of quasi optical communications. Although LoS conditions are usually required at these frequencies, it is worth investigating how a large number of highly packed transmitters and receivers could compensate for the high scattering loses in NLoS conditions without accentuating potentially extreme Doppler spreads.

Appendix A

Derivation of the transformed PDF of the ToA and AoA

For single-bounced rays, the ToA-AoA parameters of the rays (τ, ϕ^R) are related to their Cartesian coordinates in (X, Y) through the following non-linear transformation equations [108]

$$X = \frac{1}{2} \frac{(c_0 \tau)^2 - d^2}{c_0 \tau + d \cos \phi^R} \cos \phi^R \tag{A.1}$$

$$Y = \frac{1}{2} \frac{(c_0 \tau)^2 - d^2}{c_0 \tau + d \cos \phi^R} \sin \phi^R. \tag{A.2}$$

The PDF in Cartesian coordinates $f_{XY}(x, y)$ can be calculated by applying the theory of transformation of random variables as [108]

$$f_{X,Y}(x, y) = |J_1(x, y)|^{-1} f_{\tau, \phi^R} \left(c_0^{-1} (\sqrt{x^2 + y^2} + \sqrt{(x + d)^2 + y^2}), \arctan(y/x) \right) \tag{A.3}$$

where $J_1(x, y)$ is the Jacobian of the transformation, i.e.,

$$|J_1(x, y)|^{-1} = c_0^{-1} \left| \frac{1}{\sqrt{x^2 + y^2}} + \frac{1 + \frac{dx}{x^2 + y^2}}{\sqrt{(x + d)^2 + y^2}} \right|. \tag{A.4}$$

Using $f_{X,Y}(x, y)$, we can obtain a second distribution for the antennas A_p^T and A_q^R and time instant t by performing shift and rotation operations on the random variables

127

(X, Y) as defined by the following transformation equations

$$\begin{bmatrix} X_1 \\ Y_1 \end{bmatrix} = \begin{bmatrix} X - x_q^R - v_x^R t \\ Y - y_q^R - v_y^R t \end{bmatrix} \begin{bmatrix} \cos \alpha_{qp}(t) & \sin \alpha_{qp}(t) \\ -\sin \alpha_{qp}(t) & \cos \alpha_{qp}(t) \end{bmatrix} \tag{A.5}$$

where $\alpha_{qp}(t)$ denotes the angle between the segment joining A_p^T and A_q^R at time instant t and the x-axis, which can be calculated as

$$\alpha_{qp}(t) = \arctan \left(\frac{y_q^R + v_y^R t - y_p^T}{x_q^R + v_x^R t - x_q^T + d} \right). \tag{A.6}$$

Obviously, at the center of both arrays and $t = 0$, the transformation defined by (A.5) becomes the identity, i.e., $X_1 = X$ and $Y_1 = Y$, and $\alpha_{qp}(t)$ reduces to zero. As this transformation corresponds to a shift and rotation of the coordinate system, hence $|J_2(x_1, y_1)|^{-1} = 1$. The distribution in Cartesian coordinates is now $f_{X_1 Y_1}(x_1, y_1) = f_{XY}(x(x_1, y_1), y(x_1, y_1))$, with

$$\begin{bmatrix} x \\ y \end{bmatrix} = \begin{bmatrix} \cos \alpha_{qp}(t) & -\sin \alpha_{qp}(t) \\ \sin \alpha_{qp}(t) & \cos \alpha_{qp}(t) \end{bmatrix} \begin{bmatrix} x_1 \\ y_1 \end{bmatrix} + \begin{bmatrix} x_q^R + v_x^R t \\ y_q^R + v_y^R t \end{bmatrix}. \tag{A.7}$$

In the third step, the random variables (X_1, Y_1) are transformed back into the ToA-AoA domain (τ_1, ϕ_1^R) by using the inverse transformation equations of (A.1) and (A.2) used in the first step, i.e.,

$$\tau_1 = c_0^{-1} \left(\sqrt{X_1^2 + Y_1^2} + \sqrt{[X_1 + d_{qp}(t)]^2 + Y_1^2} \right) \tag{A.8}$$

$$\phi_1^R = \arctan \left(Y_1 / X_1 \right) \tag{A.9}$$

where the separation $d_{qp}(t)$ between A_p^T and A_q^R depends on the antennas locations at any time as

$$d_{qp}(t) = \sqrt{\left(x_q^R + v_x^R t - d - x_q^T \right)^2 + \left(y_q^R + v_y^R t - y_p^T \right)^2}. \tag{A.10}$$

Appendix A. *Derivation of the transformed PDF of the ToA and AoA*

Thus, the joint-PDF of the random variables (τ_1, ϕ_1^R) can be computed as

$$f_{\tau_1, \phi_1^R}(\tau_1, \phi_1^R; \delta_q^R, \delta_p^T, t) = |J_3(\tau_1, \phi_1^R)|^{-1} f_{X_1 Y_1}(x_1(\tau_1, \phi_1), y_1(\tau_1, \phi_1)) \qquad \text{(A.11)}$$

where

$$x_1(\tau_1, \phi_1) = \frac{1}{2} \frac{(c_0 \tau_1)^2 - d_{qp}^2(t)}{c_0 \tau_1 + d_{qp}(t) \cos \phi_1^R} \cos \phi_1^R \qquad \text{(A.12)}$$

$$y_1(\tau_1, \phi_1) = \frac{1}{2} \frac{(c_0 \tau_1)^2 - d_{qp}^2(t)}{c_0 \tau_1 + d_{qp}(t) \cos \phi_1^R} \sin \phi_1^R \qquad \text{(A.13)}$$

and $J_3(\tau_1, \phi_1^R)$ is the Jacobian of the transformation, i.e.,

$$|J_3(\tau_1, \phi_1^R)|^{-1} = \frac{c_0}{4} \left| \frac{\left[(c_0 \tau_1)^2 - d_{qp}^2(t)\right] \left[(c_0 \tau_1)^2 + d_{qp}^2(t) + 2 d_{qp}(t) c_0 \tau_1 \cos \phi_1^R\right]}{\left[d_{qp}(t) \cos \phi_1^R + c_0 \tau_1\right]^3} \right|.$$

$$\text{(A.14)}$$

The resulting joint-PDF $f_{\tau_1, \phi_1^R}(\tau_1, \phi_1^R; \delta_q^R, \delta_p^T, t)$ in (3.5) is obtained using (A.3)–(A.14).

Appendix B

Derivation of the STV prameters of the von Mises Distribution

The simplest approach to obtain $\mu_{qp}^{\phi}(t)$ and $\kappa_{qp}(t)$ relies on the geometrical description of the channel. To find a reasonable solution, we use the Gaussian cluster model defined in (3.16) whose marginal distribution of the AoA approximates very well a von Mises distribution as it will be shown. The distribution of the position of the scatterers in the Gaussian cluster model expressed in polar coordinates (R, ϕ^R) can be obtained by applying the transformation defined by the equations $X = R \cos \phi^R$ and $Y = R \sin \phi^R$ as

$$f_{R,\phi^R}(r, \phi^R) = \frac{r}{2\pi\sigma_{xy}^2} e^{-\frac{1}{2\sigma_{xy}^2}\left(r^2 + r_c^2 - 2rr_c \cos(\phi^R - \mu_c^{\phi})\right)} \tag{B.1}$$

where the relationships $r_c^2 = x_0^2 + y_0^2$ and $\mu_c^{\phi} = \arctan(y_0/x_0)$ have been used. Clearly, the conditional distribution $f_{r,\phi^R}(\phi^R | r = r_c)$ follows a von Mises distribution with mean angle μ_c^{ϕ} and concentration parameter $\kappa_c = r_c^2/\sigma_c^2$. Integrating (B.1) w.r.t. r, the marginal distribution of the AoA is given by

$$f_{\phi^R}(\phi^R) = \frac{e^{-(r_c/\sqrt{2}\sigma_{xy})^2}}{2\pi} + \frac{1}{2\sqrt{2\pi}} \frac{r_c}{\sigma_{xy}} \left(1 + \mathrm{erf}\left(\frac{r_c}{\sqrt{2}\sigma_{xy}} \cos(\phi^R - \mu_c^{\phi})\right)\right)$$
$$\times \cos(\phi^R - \mu_c^{\phi}) e^{-(r_c/\sqrt{2}\sigma_{xy})^2 \sin^2(\phi^R - \mu_c^{\phi})}. \tag{B.2}$$

It can be seen that (B.2) is a very good approximation of the von Mises distribution with mean angle μ_c^ϕ and concentration parameter $\kappa_c = (r_c/\sigma_{xy})^2$ for $\kappa \gg 1$. In practice, a root mean square error below 1% is obtained for any value of κ_c. Using the previous observation, the STV concentration parameter can be calculated as $\kappa_q^2(t) = (r_{c,q}(t)/\sigma_{xy})^2$, where $r_{c,q}(t)$ can be obtained by applying the law of cosines as

$$
\begin{aligned}
r_{c,q}^2(t) =& r_c^2 + (\delta_q^R)^2 + (v^R t)^2 - 2r_c\delta_q^R \cos(\mu_c^\phi - \alpha^R) \\
& - 2r_c v^R t \cos(\mu_c^\phi - \xi^R) + 2\delta_q^R v^R t \cos(\alpha^R - \xi^R).
\end{aligned}
\tag{B.3}
$$

Next, the distance r_c and the parameters of the von Mises distribution imposed at the center of the receiving array μ_c^ϕ and κ_c can be used to obtain the standard deviation of the Gaussian cluster model as $\sigma_{xy} = r_c/\sqrt{\kappa_c}$. The STV concentration parameter $\kappa_{qp}(t)$ in (3.25) can be computed substituting (B.3) in $\frac{r_{c,q}^2(t)}{r_c^2}\kappa$. Finally, by geometrical considerations, the STV mean AoA $\mu_{qp}^\phi(t)$ can be obtained as indicated in (3.26).

Appendix C

Distribution of the Envelope Ξ

The distribution of Ξ can be calculated as [130]

$$p_\Xi(z) = (2\pi)^2 z \int_0^\infty \left[\prod_{n=1}^N \int_0^\infty p_{g_n}(y_n) J_0(2\pi y_n x) \, \mathrm{d}y_n \right] J_0(2\pi z x) x \, \mathrm{d}x. \tag{C.1}$$

Thus, plugging (5.11) into (C.1), we obtain

$$p_\Xi(z) = (2\pi)^2 z \int_0^\infty \left(\prod_{n=1}^N \int_0^{c_n} \left[(1-p_v)\, \delta(y_n) + \frac{p_v r}{\pi \sqrt{c_n y_n - y_n^2}} \right. \right.$$
$$\left. \left. + p_v(1-r)\delta(y_n - c_n) \right] J_0(2\pi y_n x) \, \mathrm{d}y_n \right) J_0(2\pi z x) x \, \mathrm{d}x \tag{C.2}$$

$$= (2\pi)^2 z \int_0^\infty \prod_{n=1}^N \left[(1-p_v) + p_v(1-r)J_0(2\pi c_n x) \right.$$
$$\left. + \frac{p_v r}{\pi} \int_0^{c_n} \frac{J_0(2\pi y_n x)}{\sqrt{c_n y_n - y_n^2}} \, \mathrm{d}y_n \right] J_0(2\pi z x) x \, \mathrm{d}x \tag{C.3}$$

$$= (2\pi)^2 z \int_0^\infty \prod_{n=1}^N \left[(1-p_v) + p_v(1-r)J_0(2\pi c_n x) \right.$$
$$\left. + p_v r\, {}_2F_3\left(\frac{1}{4}, \frac{3}{4}; \frac{1}{2}, 1, 1; -(c_n \pi x)^2 \right) \right] J_0(2\pi z x) x \, \mathrm{d}x \tag{C.4}$$

for $z > 0$ and with ${}_2F_3(\cdot; \cdot; \cdot)$ denoting the generalized hypergeometric series of order 2, 3 [124]. For the special case where all the windows have the same maximum amplitude

132

$c = c_n$, then

$$p_\Xi(z) = (2\pi)^2 z \int_0^\infty \left\{ 1 + p_v \left[{}_2F_3 \left(1/4, 3/4; 1/2, 1, 1; -(c\pi x)^2 \right) r \right. \right.$$
$$\left. \left. + J_0(2\pi cx)(1-r) - 1 \right]^N J_0(2\pi zx)x \, \mathrm{d}x. \right. \tag{C.5}$$

As the number of active rays at time instant t is a Binomial-distributed random variable with N trials and probability of success $p_v = (\lambda^R T_C)^{-1}$, the average number of visible rays at any time instant is $N_a = N(\lambda^R T_C)^{-1}$. Thus, substituting $p_v = \frac{N_a}{N}$ into (C.5)

$$p_\Xi(z) = (2\pi)^2 z \int_0^\infty \left\{ 1 + \frac{N_a}{N} \left[{}_2F_3 \left(1/4, 3/4; 1/2, 1, 1; -(c\pi x)^2 \right) r \right. \right.$$
$$\left. \left. + J_0(2\pi cx)(1-r) - 1 \right]^N J_0(2\pi zx)x \, \mathrm{d}x. \right. \tag{C.6}$$

Let us assume that $T_S \to \infty$, the average number of rays N_a is constant over the simulation time, and the total number of rays $N \to \infty$. Under these conditions, we can use the well-known identity $e^x = \lim_{n\to\infty}(1 + x/n)^n$ in the integrand of (C.6) as

$$p_\Xi(z) = (2\pi)^2 z \int_0^\infty \exp \left\{ N_a \left[{}_2F_3 \left(\frac{1}{4}, \frac{3}{4}; \frac{1}{2}, 1, 1; -(c\pi x)^2 \right) r \right. \right.$$
$$\left. \left. + J_0(2\pi cx)(1-r) - 1 \right] \right\} J_0(2\pi zx)x \, \mathrm{d}x. \tag{C.7}$$

References

[1] "Cisco visual networking index VNI: Global mobile data traffic forecast." `www.cisco.com/c/en/us/solutions/collateral/service-provider/visual-networking-index-vni/white-paper-c11-738429.html`. Accessed: 2019-02-18.

[2] M. P. Mills, "An overview of the electricity used by the global digital ecosystem." `https://www.tech-pundit.com/wp-content/uploads/2013/07/Cloud_Begins_With_Coal.pdf?c761ac&c761ac`, 2013. Accessed: 2019-07-01.

[3] X. Gao, F. Tufvesson, O. Edfors, and F. Rusek, "Measured propagation characteristics for very-large MIMO at 2.6 GHz," in *Proc. IEEE ASILOMAR'12*, (Pacific Grove, USA), pp. 295–299, Nov. 2012.

[4] J. Li *et al.*, "Cluster-based 3-D channel modeling for massive MIMO in subway station environment," *IEEE Access*, vol. 6, pp. 6257–6272, Dec. 2017.

[5] S. Payami and F. Tufvesson, "Delay spread properties in a measured massive MIMO system at 2.6 GHz," in *Proc. IEEE PIMRC'13*, (London, United Kingdom), pp. 53–57, Sept. 2013.

[6] S. Payami and F. Tufvesson, "Channel measurements and analysis for very large array systems at 2.6 GHz," in *Proc. IEEE EUCAP'12*, (Prague, Czech Republic), pp. 433–437, Mar. 2012.

[7] E. Björnson, L. Sanguinetti, H. Wymeersch, J. Hoydis, and T. L. Marzetta, "Massive MIMO is a reality - What is next? Five promising research directions for antenna arrays," *arXiv e-prints*, p. arXiv:1902.07678, Feb 2019.

[8] J. Hoydis, C. Hoek, T. Wild, and S. ten Brink, "Channel measurements for large antenna arrays," in *Proc. ISWCS'12*, (Paris, France), pp. 811–815, Aug. 2012.

[9] "METIS channel models," Tech. Rep. D1.4 v3, ICT-317669 METIS Project, June 2015.

[10] G. Gougeon, M. Brau, Y. Corre, T. Tenoux, and Y. Lostanlen, "3D ray-based propagation channel modeling for multi-layer wireless network performance simulation: Focus on the MIMO channel rank," in *Proc. IEEE EuCAP'14*, (The Hague, Netherlands), Apr. 2014.

[11] A. M. Sayeed, "Deconstructing multiantenna fading channels," *IEEE Trans. Signal Process.*, vol. 50, no. 10, pp. 2563–2579, 2002.

[12] M. Pätzold, *Mobile radio channels.* West Sussex: John Wiley & Sons, 2 ed., 2012.

[13] S. Wu *et al.*, "A non-stationary wideband channel model for massive MIMO communication systems," *IEEE Trans. Wireless Commun.*, vol. 14, pp. 1434–1446, Mar. 2015.

[14] H. Wu, S. Jin, and X. Gao, "Non-stationary multi-ring channel model for massive mimo systems," in *Proc. Conf. Wireless Commun. Signal Processing, WCSP'15*, (Nanjing, China), pp. 1–6, Oct 2015.

[15] P. Almers *et al.*, "Survey of channel and radio propagation models for wireless MIMO systems," *Eurasip J. Wireless Commun. and Networking*, vol. 2007, no. Section 3, 2007.

[16] X. Gao, F. Tufvesson, and O. Edfors, "Massive MIMO channels - measurements and models," in *Proc. IEEE ASILOMAR'13*, (Pacific Grove, USA), pp. 280–284, Nov. 2013.

[17] "5GPPP vision and mission." `https://5g-ppp.eu/`. Accessed: 2019-03-01.

[18] ITU-R, *IMT Vision – Framework and Overall Objectives of the Future Development of IMT for 2020 and Beyond*, 2015.

[19] W. Webb, *Wireless Communications: The Future.* John Wiley & Sons, 1 ed., 2007.

[20] H. Claussen, D. Lopez-Perez, L. Ho, R. Razavi, and S. Kucera, *Small Cell Networks: Deployment, Management, and Optimization.* Wiley/IEEE Press, 1 ed., 2017.

[21] A. Goldsmith, S. A. Jafar, I. Maric, and S. Srinivasa, "Breaking spectrum gridlock with cognitive radios: An information theoretic perspective," *Proc. IEEE*, vol. 97, pp. 894–914, May 2009.

[22] T. S. Rappaport *et al.*, "Millimeter wave mobile communications for 5G cellular: It will work!," *IEEE Access*, vol. 1, pp. 335–349, 2013.

[23] S. Kutty and D. Sen, "Beamforming for millimeter wave communications: An inclusive survey," *IEEE Commun. Surveys Tuts*, vol. 18, pp. 949–973, Second quarter 2016.

[24] E. G. Larsson and P. Stoica, *Space-Time Block Coding for Wireless Communications.* Cambridge university press, 1 ed., 2003.

[25] 3GPP, "3rd generation partnership project; technical specification group radio access network; evolved universal terrestrial radio access (E-UTRA); user equipment radio transmission and reception (release 10)," Tech. Rep. 36.101, 2011.

[26] D. Lopez-Perez, A. Garcia-Rodriguez, L. Galati-Giordano, M. Kasslin, and K. Doppler, "IEEE 802.11be − extremely high throughput: The next generation of Wi-Fi technology beyond 802.11ax," 2019. preprint, `https://arxiv.org/pdf/1902.04320`.

[27] E. Dahlman, S. Parkvall, and J. Skold, *5G NR: The Next Generation Wireless Access Technology.* London, UK: Academic Press, 2018.

[28] 3GPP, "3rd generation partnership project; technical specification group services and system aspects; release 15 description; summary of rel-15 work items (release 15)," Tech. Rep. 21.915, 2019.

[29] 3GPP, "Enhancements on mimo for nr," Tech. Rep. 800085, 2019.

[30] D. Persson, B. K. Lau, and E. G. Larsson, "Scaling up MIMO: Opportunities and challenges with very large arrays," *IEEE Signal Process. Mag.*, vol. 30, pp. 40–60, Jan. 2013.

[31] E. G. Larsson, O. Edfors, F. Tufvesson, and T. L. Marzetta, "Massive MIMO for next generation wireless systems," *IEEE Commun. Mag.*, vol. 52, pp. 186–195, Feb. 2013.

[32] H. Q. Ngo, E. G. Larsson, and T. L. Marzetta, "Energy and spectral efficiency of very large multiuser MIMO systems," *IEEE Trans. Commun.*, vol. 61, pp. 1436–1449, April 2013.

[33] E. Björnson, E. G. Larsson, and T. L. Marzetta, "Massive MIMO: ten myths and one critical question," *IEEE Commun. Mag.*, vol. 54, pp. 114–123, Feb. 2016.

[34] D. Tse and P. Viswanath, *Fundamentals of wireless communication.* Cambridge: University Press, 1 ed., 2005.

[35] C. Y. Chiu, J. B. Yan, and R. D. Murch, "24-port and 36-port antenna cubes suitable for mimo wireless communications," *IEEE J. Trans. Antennas Propag.*, vol. 56, pp. 1170–1176, Apr. 2008.

[36] C. Shepard *et al.*, "Argos: practical many-antenna base stations," in *Proc. ACM MOBICOM'12*, (Istanbul, Turkey), pp. 53–64, 2012.

[37] J. Li and Y. Zhao, "Channel characterization and modeling for large-scale antenna systems," in *Proc. IEEE ISCIT'14*, no. 1, (Incheon, South Korea), pp. 559–563, Sept. 2014.

[38] T. Jämsä, P. Kyösti, and K. Kusume, "Deliverable D1.2 - Initial channel models based on measurements," tech. rep., ICT-317669 METIS Project, 2014.

[39] J. Vieira *et al.*, "A flexible 100-antenna testbed for Massive MIMO," in *Proc. IEEE GLOBECOM'14*, (Austin, USA), pp. 287–293, Dec. 2014.

[40] X. Gao, O. Edfors, F. Rusek, and F. Tufvesson, "Linear pre-coding performance in measured very-large MIMO channels," in *Proc. IEEE VTC Fall'11*, (San Francisco, CA, USA), pp. 1–5, Sept. 2011.

[41] A. O. Martínez, E. D. Carvalho, and J. O. Nielsen, "Towards very large aperture massive MIMO: A measurement based study," in *Proc. IEEE Globecom Workshops*, (Austin, TX), Dec. 2014.

[42] X. Gao, O. Edfors, F. Rusek, and F. Tufvesson, "Massive MIMO performance evaluation based on measured propagation data," *IEEE Trans. Wireless Commun.*, vol. 14, pp. 3899–3911, July 2015.

[43] X. Gao, O. Edfors, F. Tufvesson, and E. G. Larsson, "Massive MIMO in real propagation environments: do all antennas contribute equally?," *IEEE Trans. Commun.*, vol. 63, pp. 3917–3928, Nov. 2015.

[44] W. Li *et al.*, "Channel measurements and angle estimation for massive MIMO systems in a stadium," in *Proc. IEEE ICACT'15*, (Seoul, South Korea), pp. 105–108, July 2015.

[45] J. Huang *et al.*, "Multi-frequency mmWave massive MIMO channel measurements and characterization for 5G wireless communication systems," *IEEE J. Sel. Areas Commun.*, vol. 35, pp. 1591–1605, July 2017.

[46] J. Chen, X. Yin, X. Cai, and S. Wang, "Measurement-based massive MIMO channel modeling for outdoor LoS and NLoS environments," *IEEE Access*, vol. 5, pp. 2126–2140, 2017.

[47] M. Gudmundson, "Correlation model for shadow fading in mobile radio systems," *Electronics Letters*, vol. 27, pp. 2145–2146, Nov 1991.

[48] D. Fei *et al.*, "Massive MIMO channel measurements and analysis at 3.33 GHz," in *Proc. ChinaCom'15*, pp. 194–198, Aug 2015.

[49] J. Chen, X. Yin, and S. Wang, "Measurement-based massive MIMO channel modeling in 13–17 GHz for indoor hall scenarios," in *Proc. IEEE ICC'16*, pp. 1–5, May 2016.

[50] J. Li *et al.*, "Measurement-based characterizations of indoor massive MIMO channels at 2 GHz, 4 GHz, and 6 GHz frequency bands," in *Proc. IEEE VTC'16 Spring*, pp. 1–5, May 2016.

[51] Q. Wang *et al.*, "Parameter estimation using SAGE algorithm based on massive MIMO channel measurements," in *Proc. IEEE APS/URSI'16*, pp. 1457–1458, June 2016.

[52] J.-Z. Li *et al.*, "Indoor massive multiple-input multiple-output channel characterization and performance evaluation," *Frontiers of Information Technology & Electronic Engineering*, vol. 18, pp. 773–787, Jun 2017.

[53] B. Ai *et al.*, "On indoor millimeter wave massive MIMO channels: Measurement and simulation," *IEEE J. Sel. Areas Commun.*, vol. 35, pp. 1678–1690, July 2017.

[54] C. Wang, J. Zhang, L. Tian, M. Liu, and Y. Wu, "The variation of clusters with increasing number of antennas by virtual measurement," in *Proc. IEEE EUCAP'17*, pp. 648–652, Mar. 2017.

[55] J. Li, Y. Zhao, and Z. Tan, "Indoor channel measurements and analysis of a large-scale antenna system at 5.6 GHz," in *Proc. IEEE ICCC'14*, (Shanghai, China), pp. 281–285, Oct 2014.

[56] H. Q. Ngo, A. Ashikhmin, H. Yang, E. G. Larsson, and T. L. Marzetta, "Cell-free massive MIMO versus small cells," *IEEE Trans. Wireless Commun.*, vol. 16, pp. 1834–1850, March 2017.

[57] A. Amiri, M. Angjelichinoski, E. de Carvalho, and R. W. Heath, "Extremely large aperture massive MIMO: Low complexity receiver architectures," in *Proc. IEEE Globecom Workshops'18*, pp. 1–6, Dec 2018.

[58] E. Björnson, J. Hoydis, and L. Sanguinetti, "Massive MIMO networks: Spectral, energy, and hardware efficiency," *Foundations and Trends® in Signal Processing*, vol. 11, no. 3-4, pp. 154–655, 2017.

[59] Q. Wang *et al.*, "Measurements and performance of large MIMO systems at 2.4 GHz for indoor WLAN," in *Proc. IEEE SCVT'14*, (Delft, Netherlands), pp. 35–40, Nov 2014.

[60] A. Bernland, M. Gustafsson, C. Gustafson, F. Tufvesson, and S. Member, "Estimation of Spherical Wave Coefficients From 3-D Positioner Channel Measurements," *IEEE Antennas Wireless Propag. Lett.*, vol. 11, pp. 608–611, 2012.

[61] F. Rusek, O. Edfors, and F. Tufvesson, "Indoor multi-user MIMO: measured user orthogonality and its impact on the choice of coding," in *Proc. IEEE EUCAP'12*, (Prague, Czech Republic), pp. 2289–2293, Mar. 2012.

[62] E. Bjornson, J. Hoydis, and L. Sanguinetti, "Massive MIMO has unlimited capacity," *IEEE Trans. Wireless Commun.*, vol. 17, pp. 574–590, Jan 2018.

[63] A. Chockalingam and B. Sundar Rajan, *Large MIMO Systems.* Cambridge University Press, 1 ed., 2014.

[64] L. Liu *et al.*, "Channel capacity investigation of a linear massive MIMO system using spherical wave model in LOS scenarios," *Sci. China Inf. Sci.*, vol. 59, pp. 1–15, 2016.

[65] J. Weng, X. Tu, Z. Lai, S. Salous, and J. Zhang, "Indoor massive mimo channel modelling using ray-launching simulation," *Int. J. Antennas Propag.*, vol. 2014, 2014.

[66] C.-X. Wang *et al.*, "Recent advances and future challenges for massive MIMO channel measurements and models," *Sci. China Inf. Sci.*, vol. 59, no. 2, pp. 1–16, Feb. 2016.

[67] D.-S. Shiu, G. J. Foschini, M. J. Gans, and J. M. Kahn, "Fading correlation and its effect on the capacity of multielement antenna systems," *IEEE J. Trans. Commun.*, vol. 48, pp. 502–513, Mar 2000.

[68] J. P. Kermoal, L. Schumacher, K. I. Pedersen, P. E. Mogensen, and F. Frederiksen, "A stochastic mimo radio channel model with experimental validation," *IEEE J. Select. Areas Commun.*, vol. 20, pp. 1211–1226, Aug 2002.

[69] W. Weichselberger, M. Herdin, H. Ozcelik, and E. Bonek, "A stochastic MIMO channel model with joint correlation of both links," *IEEE Trans. Wireless Commun.*, vol. 5, no. 1, pp. 90–100, 2006.

[70] C. Oestges, "Validity of the Kronecker model for MIMO correlated channels," in *Proc. IEEE VTC'06*, vol. 6, (Melbourne, Vic), pp. 2818–2822, May 2006.

[71] S.-B. Wu, C.-X. Wang, E.-H. Aggoune, M. Alwakeel, and Y. Yang, "A novel Kronecker-based stochastic model for massive MIMO channels," in *Proc. IEEE ICCC'15*, pp. 53–57, Nov. 2015.

[72] V. Erceg, "IEEE 802.11 document 03/940r4," tech. rep., 2004.

[73] H. Ozcelik, N. Czink, and E. Bonek, "What makes a good mimo channel model?," in *Proc. IEEE VTC'05*, vol. 1, pp. 156–160, May 2005.

[74] C.-X. Wang, X. Hong, H. Wu, and W. Xu, "Spatial-temporal correlation properties of the 3GPP spatial channel model and the Kronecker MIMO channel model," *EURASIP J. Wireless Commun. and Networking*, vol. 2007, no. 1, pp. 1–10, 2007.

[75] J. Liberti and T. Rappaport, "A geometrically based model for line-of-sight multipath radio channels," in *Proc. IEEE VTC'96*, vol. 2, (Atlanta, GA, USA.), pp. 844–848, May 1996.

[76] A. Ghazal, C.-X. Wang, B. Ai, D. Yuan, and H. Haas, "A Nonstationary Wideband MIMO Channel Model for High-Mobility Intelligent Transportation Systems," *IEEE J. Trans. Intell. Transp. Syst.*, vol. 16, no. 2, pp. 1–13, 2014.

[77] Y. Xie, B. Li, X. Zuo, M. Yang, and Z. Yan, "A 3D geometry-based stochastic model for 5G massive MIMO channels," in *Proc. QSHINE'15*, pp. 216–222, Aug 2015.

[78] L. Bai, C. Wang, S. Wu, J. Sun, and W. Zhang, "A 3-D wideband multi-confocal ellipsoid model for wireless massive MIMO communication channels with uniform planar antenna array," in *Proc. IEEE VTC'17 Spring*, pp. 1–6, June 2017.

[79] A. F. Molisch, "A generic model for mimo wireless propagation channels in macro- and microcells," *IEEE J. Trans. Signal Process.*, vol. 52, pp. 61–71, Jan 2004.

[80] H. Hofstetter, A. F. Molisch, and N. Czink, "A twin-cluster mimo channel model," in *Proc. IEEE EuCAP'06*, pp. 1–8, Nov 2006.

[81] L. Correia, *Mobile Broadband Multimedia Networks*. Academic Press, 1 ed., 2006.

[82] R. Verdone and A. Zannella, *Pervasive mobile and ambient wireless communications – the COST action 2100*. Springer, 1 ed., 2011.

[83] "Spatial channel model for multiple-input multiple-output (MIMO) simulations," Tech. Rep. v11.0.0, 3GPP T.S. 25.996, 2012.

[84] K. Kyosti *et al.*, "WINNER II Channel Models: Part I channel models," Tech. Rep. D1.1.2 V1.2, IST-4-027756 WINNER II, 2007.

[85] J. Meinilä *et al.*, "WINNER+ Final Channel Models," Tech. Rep. D5.3 V1.0, June 2010.

[86] "Guidelines for evaluation of radio interface technologies for IMT-Advanced," tech. rep., ITU-R M.2135, Switzerland, 2008.

[87] "Study on 3D channel model for LTE," Tech. Rep. TR 36.873, V12.4.0, 3rd Generation Partnership Project (3GPP), 2017.

[88] S. Wu, C. X. Wang, E. H. M. Aggoune, M. M. Alwakeel, and Y. He, "A non-stationary 3-D wideband twin-cluster model for 5G massive MIMO channels," *IEEE J. Sel. Areas Commun.*, vol. 32, pp. 1207–1218, June 2014.

[89] S. Wu, C. X. Wang, E. H. M. Aggoune, M. M. Alwakeel, and X. H. You, "A general 3D non-stationary 5G wireless channel model," *IEEE Trans. Commun.*, vol. 66, pp. 3065–3078, July 2018.

[90] X. Gao, J. Flordelis, G. Dahman, F. Tufvesson, and O. Edfors, "Massive MIMO channel modeling - extension of the COST 2100 model," in *Proc. JNCW Workshop*, (Barcelona, Spain), Oct. 2015.

[91] S. Jaeckel, L. Raschkowski, K. Börner, and L. Thiele, "QuaDRiGa: A 3-D multi-cell channel model with time evolution for enabling virtual field trials," *IEEE Trans. Antennas Propag.*, vol. 62, pp. 3242–3256, June 2014.

[92] M. Peter *et al.*, "Measurement Campaigns and Initial Channel Models for Preferred Suitable Frequency Ranges," Tech. Rep. D2.1 V1.0, mmMagic Project, 2016.

[93] G. T. 38.901, "Study on channel model for frequencies from 0.5 to 100 GHz," Tech. Rep. V14.3.0, 3GPP, 2017.

[94] ITU-R, "Preliminary draft new report ITU-R M.[IMT-2020.EVAL], test environments and channel models," Tech. Rep. TR 38.901 , V14.3.0, ITU, June 2017.

[95] "Channel modeling and characterization," Tech. Rep. D5.1 V1.0, ICT FP7 MiWEBA project, June 2014.

[96] A. F. Molisch, H. Asplund, R. Heddergott, M. Steinbauer, and T. Zwick, "The COST 259 directional channel model-part I: Overview and methodology," *IEEE Trans. Wireless Commun.*, vol. 5, pp. 3421–3433, Dec. 2006.

[97] J. Medbo *et al.*, "Channel modelling for the fifth generation mobile commun.," in *Proc. IEEE EuCAP'14*, (The Hague, Netherlands), pp. 219–223, Apr. 2014.

[98] G. Matz, "On non-WSSUS wireless fading channels," *IEEE Trans. Wireless Commun.*, vol. 4, pp. 2465–2478, Sept 2005.

[99] A. Gehring, M. Steinbauer, I. Gaspard, and M. Grigat, "Empirical channel stationarity in urban environments," in *Proc. EPMCC'01*, (Vienna, Austria), Feb. 2001.

[100] C. X. Wang, A. Ghazal, B. Ai, Y. Liu, and P. Fan, "Channel measurements and models for high-speed train communication systems: A survey," *IEEE Commun. Surveys Tuts.*, vol. 18, pp. 974–987, 2nd Quart. 2016.

[101] T. Zwick, C. Fischer, D. Didascalou, and W. Wiesbeck, "A stochastic spatial channel model based on wave-propagation modeling," *IEEE J. Sel. Areas Commun.*, vol. 18, pp. 6–15, Jan. 2000.

[102] C.-C. Chong, D. I. Laurenson, and S. McLaughlin, "The implementation and evaluation of a novel wideband dynamic directional indoor channel model based on a Markov process," in *Proc. IEEE PIMRC'03*, (Beijing, China), Sept. 2003.

[103] Y. Yuan, C. X. Wang, Y. He, M. M. Alwakeel, and E. H. M. Aggoune, "3D wideband non-stationary geometry-based stochastic models for non-isotropic MIMO vehicle-to-vehicle channels," *IEEE Trans. Wireless Commun.*, vol. 14, pp. 6883–6895, Dec. 2015.

[104] A. Ghazal, C. X. Wang, B. Ai, D. Yuan, and H. Haas, "A nonstationary wideband MIMO channel model for high-mobility intelligent transportation systems," *IEEE Trans. Intell. Transp. Syst.*, vol. 16, pp. 885–897, Apr. 2015.

[105] Y. Liu, C.-X. Wang, C.-F. Lopez, and X. Ge, "3D non-stationary wideband circular tunnel channel models for high-speed train wireless communication systems," *Sci. China Inf. Sci.*, vol. 60, Aug. 2017.

[106] A. Ghazal *et al.*, "A non-stationary IMT-Advanced MIMO channel model for high-mobility wireless communication systems," *IEEE Trans. Wireless Commun.*, vol. 16, pp. 2057–2068, Apr. 2017.

144

[107] J. Bian *et al.*, "A WINNER+ based 3-D non-stationary wideband MIMO channel model," *IEEE Trans. Wireless Commun.*, vol. 17, pp. 1755–1767, Mar. 2018.

[108] A. Borhani and M. Pätzold, "On the spatial configuration of scatterers for given delay-angle distributions," *IAENG Engineering Letters*, vol. 22, pp. 34–38, Feb. 2014.

[109] R. B. Ertel and J. H. Reed, "Angle and time of arrival statistics for circular and elliptical scattering models," *IEEE J. Sel. Areas Commun.*, vol. 17, pp. 1829–1840, Nov 1999.

[110] S. H. Kong, "TOA and AOD statistics for down link Gaussian scatterer distribution model," *IEEE Trans. Wireless Commun.*, vol. 8, pp. 2609–2617, May 2009.

[111] K. Mardia and P. E. Jupp, *Directional Statistics.* John Wiley & Sons, 2000.

[112] A. Y. Olenko, K. T. Wong, and E. H.-O. Ng, "Analytically derived TOA-DOA statistics of uplink/downlink wireless multipaths arisen from scatterers on a hollow-disc around the mobile," *IEEE Antennas Wireless Propag. Lett.*, vol. 2, no. 1, pp. 345–348, 2003.

[113] A. Borhani and M. Pätzold, "A unified disk scattering model and its angle-of-departure and time-of-arrival statistics," *IEEE Trans. Veh. Technol.*, vol. 62, pp. 473–485, Feb. 2013.

[114] L. Devroye, *Non-uniform Random Variate Generation.* New York: Springer-Verlag New York Inc, 1 ed., 1986.

[115] C. F. López, C.-X. Wang, and R. Feng, "A novel 2D non-stationary wideband massive MIMO channel model," in *Proc. IEEE CAMAD'16*, (Toronto, Canada), pp. 207–212, Oct. 2016.

[116] C. F. López and C.-X. Wang, "Novel 3D non-stationary wideband models for massive MIMO channels," *IEEE Trans. Wireless Commun.*, vol. 17, pp. 2893–2905, May 2018.

[117] C. A. Gutiérrez and M. Pätzold, "The Riemann sum method for the design of sum-of-cisoids simulators for Rayleigh fading channels in non-isotropic scattering environments," in *Proc. IEEE ICUMT'09*, (St. Petersburg, Russia), pp. 1–5, Oct. 2009.

[118] A. Papoulis, *Probability, random variables and stochastic processes.* USA: McGraw-Hill, 4 ed., 2002.

[119] M. Pätzold and V. D. Nguyen, "A spatial simulation model for shadow fading processes in mobile radio channels," in *Proc. IEEE PIMRC'04*, (Barcelona, Spain), pp. 1832–1838, Sept 2004.

[120] X. Cai and G. B. Giannakis, "A two-dimensional channel simulation model for shadowing processes," *IEEE Trans. Veh. Technol.*, vol. 52, pp. 1558–1567, Nov. 2003.

[121] C. A. Balanis, *Antenna Theory: Analysis and Design.* New York, NY, USA: Wiley-Interscience, 2005.

[122] S. Gregson, J. McCormick, and C. Parini, *Principles of planar near-field antenna measurements.* London, UK: The Institution of Engineering and Technology, 1 ed., 2007.

[123] C.-F. Lopez and C.-X. Wang, "A study of delay drifts on massive MIMO wideband channel models," in *Proc. IEEE WSA'18*, (Bochum, Germany), Mar. 2018.

[124] I. S. Gradshteyn and I. M. Ryzhik, *Table of Integrals, Series, and Products.* London, UK: Academic Press, 8 ed., 2014.

[125] A. Borhani, G. L. Stüber, and M. Pätzold, "A random trajectory approach for the development of nonstationary channel models capturing different scales of fading," *IEEE Trans. Veh. Technol.*, vol. 66, pp. 2–14, Jan. 2017.

[126] G. D. Durgin, *Space-Time Wireless Channels.* Upper Saddle River, NJ, USA: Prentice-Hall, 2002.

[127] C.-L. J. Lam and T. Le-Ngoc, "Estimation of typical sum of lognormal random variables using log shifted gamma approximation," *IEEE Commun. Lett.*, vol. 10, pp. 234–235, Apr. 2006.

[128] N. B. Mehta, J. Wu, A. F. Molisch, and J. Zhang, "Approximating a sum of random variables with a lognormal," *IEEE Trans. Wireless Commun.*, vol. 6, pp. 2690–2699, July 2007.

[129] A. Abdi and M. Kaveh, "On the utility of gamma PDF in modeling shadow fading (slow fading)," in *Proc. IEEE VTC'99*, May 1999.

[130] M. Pätzold and G. Rafiq, "Sparse multipath channels: Modelling, analysis, and simulation," in *Proc. IEEE PIMRC'13*, Sept. 2013.